Modelling Wire Problems using the Unstructured Transmission Line Modelling Method

Zhewen Zhang, BEng (Hons.)

Thesis submitted to The University of Nottingham

for the degree of Doctor of Philosophy, August 2018

Abstract

In this thesis, the Unstructured Transmission Line Modelling (UTLM) method is used to study wire problems with various configurations and structures. The analysis of multi-wire systems based upon local field solutions for wave equations is presented for the understanding of propagation mode within a wire bundle. The derivation of TLM scheme based upon unstructured triangular and tetrahedral meshes is presented, along with applications to the study of electromagnetic coupling and field transmission of canonical single-wire models and junction structures. The impact of wire configurations and positioning of wires within a bundle on the electromagnetic coupling into wires is investigated. Moreover, the radiation patterns of a Log-periodic dipole array (LPDA) antenna in different frequency bands is investigated. The accuracy of results presented in this work is validated by self-convergence with respect to sufficient simulation parameters and the efficiency of this method is evaluated based upon computational expenses.

Acknowledgements

I would like to express my deepest gratitude to my supervisors, Prof. Phillip Sewell, Dr. Ana Vukovic and Prof. Trevor Bension, for their meticulous guidance, insightful comments and constructive criticisms. I would also like to thank Dr. Vicky Meng, who has been a special guider during my first two years of PhD. I will not have finished my PhD without their immeasurable support.

A very special thanks is given to Prof. Dave Thomas, Dr. Steve Greedy and the rest of the academics at the George Green Institute for Electromagnetics Research group for their valued support throughout the years.

The work presented here was carried out as part of ICE-NITE, a collaborative research project supported by Innovate UK under contract reference 101665. The project consortium includes BAE SYSTEMS Limited (coordinator), Bombardier, Horiba MIRA Limited, ITI Limited, The University of Liverpool, and The University of Nottingham.

I must also thank my collegues during my PhD, Dr. Vicky Meng, Dr. Sendy Phang, Dr. Ahmed Elkalsh, Dr. Dan Simons, Dr. Soumitro Kumar (Congrats to the viva!), Dr Hayan Nasser, Dr. Afonso Bernardino, Latifah Abdul Aziz (Good luck with your thesis as well) Nasri, Najla, Joju and Andrew. I am so lucky to meet you all and I will never forget our happy dinner nights, movie times and board games.

Finally, I would like to thank my family, who has been so patient and so supportive in the past 27 years. I would like to say sorry to my maternal grandparents as I missed the funeral in my first and second year of PhD. I miss you.

Contents

List of Symbols

This list registers symbols that are consistently used throughout in the thesis. Local symbols which are used in a specific section are not listed here to avoid ambiguity.

Symbol	Description
$\boldsymbol{E}$	Electric field intensity
$\boldsymbol{D}$	Electric flux density
$\boldsymbol{H}$	Magnetic field intensity
$\boldsymbol{B}$	Magnetic flux density
$\boldsymbol{J}$	Electric current density
ε	Electric permittivity
ε_0	Free-space permittivity
ε_r	Relative permittivity
σ	Electrical conductivity
ρ	Electric charge density
μ	Magnetic permeability
μ_0	Free-space permeability
$\boldsymbol{P}$	Poynting vector
ω	Angular frequency
j	Imaginary number $\sqrt{-1}$
γ	Complex propagation constant
α	Attenuation (+) or amplification (−)
β	Real part of propagation constant
$\mathbf{S}$	Scattering matrix

λ	wavelength
τ	scaling factor
Δ_t	TLM time step
V	Voltage
I	Current
G	Conductivity
C	Capacitance
L	Inductance
Z	Impedance
J_m	Bessel function of the 1^{st} kind order m
Y_m	Bessel function of the 2^{nd} kind order m
$H_m^{(1)}$	Hankel function of the 1^{st} kind order m
$H_m^{(2)}$	Hankel function of the 2^{nd} kind order m
Q	Quality factor
Φ	Field components

List of Abbreviation

EMC	Electromagnetic Compatibility
EMI	Electromagnetic Interference
CEM	Computational Electromagnetics
HIRF	High Intensity Radio Frequency
TLM	Transmission Line Modelling
UTLM	Unstructured Transmission Line Modelling
T-matrix	Transfer matrix
S-matrix	Scattering matrix
FDTD	Finite-Difference Time-Domain
MOM	Method of Moment
Q-factor	Quality factor
TEM	Transverse Electromagnetic
TE	Transverse Electric
TM	Transverse Magnetic
MTL	Multiconductor Transmission Line
p.u.l	per-unit-length
PEC	perfect electric conductor

1

Introduction

This chapter presents a brief introduction of the background of this thesis and a short history of wire coupling and electromagnetic compatibility (EMC) study. Different numerical modelling methods for modern Computational Electromagnetics (CEM) are introduced and compared.

***

1.1 Background

Wire coupling study has been seen increasing interest in recent years for following reasons. Wires are fundamental components in electromagnetic compatibility (EMC) problems as they provide both signal and power transfer in electrical and electronic systems. Although they are geometrically small features in an integrated system such as aircraft or vehicles, their effect on electromagnetic responses to external sources such as external High Intensity Radio Frequency (HIRF) environment and as a result the system performance is significant. Moreover, wires are usually tied together as bundles to provide space flexibility in a system. Coupling in wires due to close spacing between each other is non-negligible. Modern EMC studies demand the investigation of such complex systems in the design stage and elimination of unwanted electromagnetic interference (EMI) that fails demonstrating EMC compliance.

The history of wire coupling study dates back to the 1830s when Faraday firstly demonstrated the electromagnetic induction between two iron rings due to transient current change in one coil [1.1]. In the 1860s Maxwell mathematically formulated the time-evolving structure of electromagnetic fields based four important laws. With dramatic increasing of the use of electrical appliances from communication to transportation and living, EMI has been a common phenomena in people's daily life, unexpected noises from the earphone when you listening to music and a call comes and lightning destroyed home electrical appliances. Recent researches show increasing interest in wire coupling problems within integrated electrical platforms such as aircraft to comply with the requirement for EMC of electrical and electronic systems due to external HIRF environment [1.2–1.6].

1.2 Modelling methods

This section introduces and analyses methods that can be used for the modelling of wire coupling and EMC problems.

1.2.1 Transmission line methods

There are a number of analytical and numerical methods developed to model wire coupling and electromagnetic compatibility. Among them the multi-conductor transmission line (MTL) method is one of the most popular and widely used methods. Transmission line (TL) Equations are derived based on the transverse electromagnetic (TEM) propagation mode of waves [1.7–1.11]. The per-unit-length (p.u.l) parameters including inductance, capacitance, resistance and conductance for the TL equation are introduced to govern the propagation of voltage and currents [1.12]. The method has been extensively developed for various applications including homogeneous and inhomogeneous medium [1.13], lossy conductors [1.14], shielded wires [1.15], twisted-wire pairs, field-to-wire coupling and crosstalk prediction [1.16–1.18]. Moreover, the incorporation of the Green's function allows time-domain analysis of MTLs [1.19]

Although the simplicity and computational efficiency of the MTL method are appreciated, there are few disadvantages of this method. Firstly, the method analyses thin wires implicitly and ignores re-radiation from wires . Moreover, this method sees difficulty in modedllling complex integrated systems [1.20].

1.2.2 Method of moments (MOM)

The method of moments (MOM) is an important numerical method for modelling currents in thin wires. It is firstly developed by Harrington [1.21,1.22] as a special form of Finite Element Method (FEM).

The fundamental rule of this method is to find solutions for a partial differential equation [1.23]

$$\mathcal{L}\{f\} = g \tag{1.1}$$

where $\mathcal{L}$ is a linear operator, f is the unknown current function and g is the testing function. Hallen's integral equation and Pocklington's integral equations for electric fields are two popular sets of equations to describe the field operation. The unknowns can be expanded into a set of basis functions such as pulse functions. The testing function is in the same form of the basis function with specific weight to enforce the boundary conditions. The continuous differential equation 1.1 can then be simplified to a set of matrix equations of finite size and the unknown currents along a thin wire is easily solved.

The advantage of the MOM is shown in its easy implementation in computers and highly accurate results. However there are also some limitations. The MOM is widely used for solving integral equations in frequency domain. This would be computationally expensive when the frequency response over a wide range is desired. The choice of basis functions also has significant effect on the accuracy and convergence of the method. Moreover, it is not very effective when applied to inhomogeneous environment and interior of conductive enclosures.

1.2.3 Finite Difference Time Domain (FDTD) method

The Finite Difference Time Domain (FDTD) method is a powerful time domain numerical modelling method that differences Maxwell's equations in both space and time domain [1.24,1.25]. It is able to model full wave electromagnetic phenomenon such as coupling, radiation and ground bounce in time domain and easily transfer to frequency response via Fourier transform [1.26] Moreover, the method shows its capability of modelling a variety of environment such non-linear material properties and complex multi-scale structures naturally. Recent researches develop thin wire formulations to incorporate analysis of thin wire features in FDTD cells [1.27–1.32]

In FDTD method, electric and magnetic field points are sampled in two interleaved grids, with a half space-step and a half time-step separation respectively. This would be potential issue when modelling the propagation of fields in anisotropic materials and describing the magneto-electric coupling as they need simultaneous field processing [1.33] Besides, electric and magnetic fields are distributed throughout the cells instead of localised at one point. This might cause potential ambiguities in locating boundary and excitations.

1.2.4 Transmission Line Modelling (TLM) method

The Transmission Line Modelling (TLM) method is another widely used numerical modelling method that solves Maxwell's differential equations in the time domain.

The method is at first developed and introduced by Kron [1.34] based on the analogy between electrical circuits and Maxwell's equations for electric and magnetic fields. The method however had not been further developed until the 1970s when a two-dimensional scattering problem was solved using the TLM method based upon Huygen's theory of wave propagation [1.35,1.36]. The development of modern computational tools enables fast development of the TLM method in three dimensions and various features. The symmetrical condensed node was introduced in the 1980s for stable and accurate modelling in three-dimensional spaces. [1.37,1.38].

Due to its time domain operation, the TLM is able to model a large variety of problems, including multi-scale structures and non-linear problems over a wide band of frequency range. Different from the FDTD method, electric and magnetic fields in TLM are defined at the same space and time step, which makes it easier when modelling problems with complex materials [1.33]. Although sampling for TLM models normally requires full-volume discretisation in the space, which might requires substantial computational resources, it is able to model more complex structures and inhomogeneous materials, which is crucial in today's EMC investigation [1.39].

The MTL method has been studied to be embedded in coarse TLM schemes to study wire coupling problems without truncation of mesh size [1.40–1.43]. An alternative thin wire model based upon local field solutions has been developed for TLM simulations [1.44–1.47]. The advantage of this method is that it requires no empirical factors and allows arbitrary placed thin wires in the mesh cell.

In recent years the Unstructured Transmission Line Modelling (UTLM) method is introduced based upon unstructured triangular and tetrahedral meshes [1.48,1.49] Although the conventional structured mesh based TLM has shown its versatility and stability in modelling a diversity of problems, there is limitations existed in describing curved boundaries such as aircraft and circular cross-sectioned wires. Stair-casing error might be non-negligible if the the conducting boundary differs from the Cartesian coordinate axes [1.50].

A two-dimensional triangular or three-dimensional tetrahedral mesh easily resolves such stair-casing problems. However it needs to be noticed that the shape and size of each single mesh might differ to fit the geometry. This arises the computational cost of simulation as information of each single node needs to be stored and more attention needs to be taken to control the synchronism of time-stepping across the mesh [1.39].

This is particularly true for modelling wiring problems due to their thin structures and long lengths and that is why various thin-wire approximation methods described above were developed instead of pursuing explicit meshing for precise wire description [1.28] However, with increasing computational power in recent years and improved algorithm of UTLM, it is now possible to model thin wires and wire bundles by direct and explicit meshing of wire structures [1.51–1.53] It is the success of UTLM in modelling generally arbitrarily shaped structures and the use of UTLM in today EMC simulations of large and complicated systems has led to the work of this thesis.

1.3 Thesis Outline

The outline of the thesis is provided as follows. **Chapter 2** reviews fundamental electromagnetic theories including Maxwell's equations and wave equations. **Chapter 3** presents the study of propagation modes in multi-conductor wire systems using local field solutions of wave equations and boundary conditions. The effects of spatial relationship and dielectric coating are explored. **Chapter 4** describes basic theory of the Transmission Line Modelling (TLM) method and extended to 2-D Unstructured TLM (UTLM) based upon triangular meshes and 3-D UTLM based upon tetrahedral meshes. **Chapter 5** presents the simulation of several canonical wiring models using UTLM method with direct modelling. Two different excitation methods, the plane wave excitation from external and the modal excitation by direct injection to the wire , are explored and junction structures are modelled. **Chapter 6** presents the study of wire bundle coupling due to external plane wave excitations using UTLM method by direct modelling. Various wire bundle configurations are explored and the current induced in wires are observed and analysed for benchmarking. **Chapter 7** presents the study of an Log periodic dipole array (LPDA) antenna in order to evaluate the capability of UTLM to model broadband wiring structure antennas. The radiation pattern of the antenna for different frequency bands are investigated.

References

[1.1] F. T. Ulaby, *Fundamentals of Applied Electromagnetics* (Prentice Hall, 1999).

[1.2] G. A. Rasek, E. Pascual-Gil, A. Schröder, I. Junqua, R. Guidi, C. A. Kreller, H. Brüns, and S. E. Loos, "HIRF Transfer Functions of a Fuselage Model: Measurements and Simulations," IEEE Transactions on Electromagnetic Compatibility **56**, 311–319 (2014).

[1.3] Z. Řeznicek, P. Tobola, G. A. Rasek, and S. E. Loos, "TD and FD simulations of internal EM environment in small aircraft and experimental test comparison," in "2012 6th European Conference on Antennas and Propagation (EUCAP)," (2012), pp. 2261–2265.

[1.4] L. Paletta, J. P. Parmantier, F. Issac, P. Dumas, and J. C. Alliot, "Susceptibility analysis of wiring in a complex system combining a 3-D solver and a transmission-line network simulation," IEEE Transactions on Electromagnetic Compatibility **44**, 309–317 (2002).

[1.5] M. Bandinelli, A. Mori, G. Galgani, D. Romano, G. Antonini, A. G. Dieudonné, and M. Dunand, "A Surface PEEC Formulation for High-Fidelity Analysis of the Current Return Networks in Composite Aircrafts," IEEE Transactions on Electromagnetic Compatibility **57**, 1027–1036 (2015).

[1.6] J. Dai, F. Dai, and X. Zhao, "Output prediction about crosstalk coupling of representative multi-cable bundle on aircraft platform based on neural network," in "2009 3rd IEEE International Symposium on Microwave, Antenna, Propagation and EMC Technologies for Wireless Communications," (2009), pp. 381–384.

[1.7] C. R. Paul, *Analysis of multiconductor transmission lines* (John Wiley & Sons, 2008).

[1.8] C. R. Paul, "Solution of the transmission-line equations under the weak-coupling assumption," (2002).

[1.9] G. Antonini, A. Orlandi, and S. a. Pignari, "Review of Clayton R. Paul Studies on Multiconductor Transmission Lines," IEEE Transactions on Electromagnetic Compatibility **55**, 639–647 (2013).

[1.10] C. R. Paul, K. W. Whites, and S. A. Nasar, *Introduction to Electromagnetic Fields*, McGraw-Hill International Editions (WCB/McGraw-Hill, 1998).

[1.11] C. R. Paul, *Introduction to Electromagnetic Compatibility*, Wiley Series in Microwave and Optical Engineering (Wiley, 2006).

[1.12] C. R. Paul, "Decoupling the multiconductor transmission line equations," (1996).

[1.13] C. R. Paul, “Solution of the Transmission-Line Equations for Three- Conductor Lines in Homogeneous Media,” Ieee Transactions on Electromagnetic Compatibility pp. 216–222 (1978).

[1.14] C. R. Paul, “Solution of the transmission-line equations for lossy conductors and imperfect earth,” (1975).

[1.15] C. R. Paul and B. A. Bowles, “Symbolic Solution of the Multiconductor Transmission-Line Equations for Lines Containing Shielded Wires,” **33**, 149–162 (1991).

[1.16] C. R. Paul and J. W. McKnight, “Prediction of Crosstalk Involving Twisted Pairs of Wires-Part I: A Transmission-Line Model for Twisted-Wire Pairs,” IEEE Transactions on Electromagnetic Compatibility **EMC-21**, 92–105 (1979).

[1.17] C. R. Paul and J. W. Mcknight, “Prediction of Crosstalk Involving Twisted Pairs of Wires-Part II: A Simplified Low-Frequency Prediction Model,” Electromagnetic Compatibility, IEEE Transactions on **EMC-21**, 105–114 (1979).

[1.18] C. R. Paul, “A SPICE model for multiconductor transmission lines excited by an incident electromagnetic field,” (1994).

[1.19] G. Antonini, “A Spectral Formulation for the Transient Analysis of Plane-Wave Coupling to Multiconductor Transmission Lines,” IEEE Transactions on Electromagnetic Compatibility **51**, 792–804 (2009).

[1.20] P. Naylor, “Coupling Between Electromagnetic Waves and Wires Using Transmission-Line Modelling,” Ph.D. thesis, University of Nottingham (1986).

[1.21] R. F. Harrington and S. U. E. E. Dept, *Matrix Methods for Solving Field Problems: Final Report* (Rome Air Development Center, Griffins Air Force Base, 1966).

[1.22] R. F. Harrington, I. Antennas, and P. Society, *Field Computation by Moment Methods*, An IEEE / OUP classic reissue (Wiley, 1993).

[1.23] G. J. Burke, A. J. Poggio, J. C. Logan, and J. W. Rockway, “Numerical Electromagnetic Code (NEC),” in “1979 IEEE International Symposium on Electromagnetic Compatibility,” (1979), pp. 1–3.

[1.24] K. S. Yee, *Numerical Solution of Initial Boundary Value Problem Involving Maxwell's Equations in Isotropic Media*, vol. AP-14 (1966).

[1.25] A. Taflove, *Computation Electrodynamics—The Finite-Difference Time-Domain Method* (1995).

[1.26] S. Harmon, S. W. Staker, M. Piket-May, and C. Christopoulos, “Comparison of numerical modeling methods FDTD and TLM,” in “2001 IEEE EMC International

Symposium. Symposium Record. International Symposium on Electromagnetic Compatibility (Cat. No.01CH37161)," , vol. 2 (2001), vol. 2, pp. 1316–1321 vol.2.

[1.27] M. Douglas, M. Okoniewski, and M. A. Stuchly, "Accurate modeling of thin wires in the FDTD method," in "IEEE Antennas and Propagation Society International Symposium. 1998 Digest. Antennas: Gateways to the Global Network. Held in conjunction with: USNC/URSI National Radio Science Meeting (Cat. No.98CH36," , vol. 2 (1998), vol. 2, pp. 1246—-1249 vol.2.

[1.28] L. G., "A stable subcell model for arbitrarily oriented thin wires for the FDTD method," International Journal of Numerical Modelling: Electronic Networks, Devices and Fields **15**, 503–515 (2002).

[1.29] R. M. Makinen, J. S. Juntunen, and M. A. Kivikoski, "An improved thin-wire model for FDTD," IEEE Transactions on Microwave Theory and Techniques **50**, 1245–1255 (2002).

[1.30] F. Edelvik, "A new technique for accurate and stable modeling of arbitrarily oriented thin wires in the FDTD method," IEEE Transactions on Electromagnetic Compatibility **45**, 416–423 (2003).

[1.31] C. Guiffaut, A. Reineix, and B. Pecqueux, "New Oblique Thin Wire Formalism in the FDTD Method With Multiwire Junctions," IEEE Transactions on Antennas and Propagation **60**, 1458–1466 (2012).

[1.32] N. V. Kantartzis, "Enhanced Thin-Wire Representation Models in a High-Order FDTD/TLM Method for Electrically Large Microwave Applications," (2013).

[1.33] J. Paul, *Modelling of General Electromagnetic Material Properties in TLM*, October (1998).

[1.34] G. Kron, "Equivalent Circuit of the Field Equations of Maxwell-I," Proceedings of the IRE **32**, 289–299 (1944).

[1.35] P. B. Johns and R. L. Beurle, "Numerical solution of 2-dimensional scattering problems using a transmission-line matrix," Electrical Engineers, Proceedings of the Institution of **118**, 1203–1208 (1971).

[1.36] C. Christopoulos, *The Transmission-Line Modelling method:TLM* (Wiley-IEEE Press, 1995).

[1.37] P. B. Johns, "New symmetrical condensed node for three-dimensional solution of electromagnetic-wave problems by TLM," Electronics Letters **22**, 162–164 (1986).

[1.38] P. B. Johns, "A Symmetrical Condensed Node for the TLM Method," IEEE Transactions on Microwave Theory and Techniques **35**, 370–377 (1987).

[1.39] C. Christopoulos, *The Transmission-Line Modeling (TLM) Method in Electromagnetics* (Morgan & Claypool, 2006).

[1.40] P. Naylor and C. Christopoulos, "A new wire node for modeling thin wires in electromagnetic field problems solved by transmission line modeling," (1990).

[1.41] A. Wlodarczyk, V. Trenkic, R. Scaramuzza, and C. Christopoulos, "A fully integrated multiconductor model for TLM," 1998 IEEE MTT-S International Microwave Symposium Digest (Cat. No.98CH36192) **3**, 1405–1408 (1998).

[1.42] V. Trenkic, A. J. Wlodarzcyk, and R. A. Scaramuzza, "Modelling of coupling between transient electromagnetic field and complex wire structures," International Journal of Numerical Modelling: Electronic Networks, Devices and Fields **12**, 257–273 (1999).

[1.43] J. Paul, C. Christopoulos, D. W. P. Thomas, and X. Liu, "Time-domain modeling of electromagnetic wave interaction with thin-wires using TLM," (2005).

[1.44] Y. K. Choong, P. Sewell, and C. Christopoulos, "New thin wire formulation for time-domain differential-equation models," International Journal of Numerical Modelling-Electronic Networks Devices and Fields **15**, 489–501 (2002).

[1.45] Y. K. Choong, P. Sewell, and C. Christopoulos, "Hybrid node for description of thin wires based on analytical field representation in EMC problems," 2002 Ieee International Symposium on Electromagnetic Compatibility, Vols 1 and 2, Symposium Record pp. 840–844 (2002).

[1.46] Y. Choong, P. Sewell, and C. Christopoulos, "Accurate modelling of an arbitrary placed thin wire in a coarse mesh," IEE Proceedings - Science, Measurement and Technology **149**, 250–253(3) (2002).

[1.47] Y. Liu, P. Sewell, K. Biwojno, and C. Christopoulos, "A generalized node for embedding subwavelength objects into 3-D transmission-line models," IEEE Transactions on Electromagnetic Compatibility **47**, 749–755 (2005).

[1.48] P. Sewell, J. G. Wykes, T. M. Benson, C. Christopoulos, D. W. P. Thomas, and A. Vukovic, "Transmission-line modeling using unstructured triangular meshes," (2004).

[1.49] P. Sewell, T. M. Benson, C. Christopoulos, D. W. P. Thomas, A. Vukovic, and J. G. Wykes, "Transmission-line modeling (TLM) based upon unstructured tetrahedral meshes," IEEE Transactions on Microwave Theory and Techniques **53**, 1919–1928 (2005).

[1.50] A. C. Cangellaris and D. B. Wright, "Analysis of the numerical error caused by the stair-stepped approximation of a conducting boundary in FDTD simulations of electromagnetic phenomena," IEEE Transactions on Antennas and Propagation **39**, 1518–1525 (1991).

[1.51] X. Meng, P. Sewell, A. Vukovic, Z. Zhang, and T. Benson, "Experimental benchmarking of unstructured transmission line modelling (UTLM) method for simulations of explicitly meshed wiring," in "2015 Computational Electromagnetics International Workshop (CEM)," (2015), pp. 1–2.

[1.52] X. Meng, P. Sewell, N. H.A. Rahman, A. Vukovic, and T. Benson, *Experimental benchmarking of Unstructured Transmission Line Modelling (UTLM) method in modelling twisted wires*, vol. 1 (2016).

[1.53] X. Meng, P. Sewell, A. Vukovic, Z. Zhang, T. M. Benson, C. Jones, S. Earl, R. Walton, and G. South, "Numerical simulation of electromagnetic coupling in explicitly meshed wiring looms and bundles," IET Science, Measurement & Technology **12**, 176–181 (2018).

2

Fundamentals of Electromagnetic Theory

2.1 Maxwell's Equations

The differential equation form of Maxwell's equations is shown below [2.1–2.3]:

$$\nabla \times \boldsymbol{E} = -\frac{\partial \boldsymbol{B}}{\partial t} \tag{2.1}$$

$$\nabla \times \boldsymbol{H} = \boldsymbol{J} + \frac{\partial \boldsymbol{D}}{\partial t} \tag{2.2}$$

$$\nabla \cdot \boldsymbol{D} = \rho \tag{2.3}$$

$$\nabla \cdot \boldsymbol{B} = 0 \tag{2.4}$$

$$\nabla \cdot \boldsymbol{J} = -\frac{\partial \rho}{\partial t} \tag{2.5}$$

$$\boldsymbol{D} = \varepsilon \boldsymbol{E} \tag{2.6}$$

$$\boldsymbol{B} = \mu \boldsymbol{H} \tag{2.7}$$

where

- E is the electric field intensity
- H is the magnetic field intensity
- D is the electric flux density
- ρ the charge density

- B is the magnetic flux density
- J is the current density
- σ is the conductivity
- ε is the electric permittivity
- μ is the magnetic permeability

The set of differential equations govern the electromagnetic field behaviour in forms of space and time rates of change at a certain point in space and time. Equation 2.1 is the Faraday's law of induction that expresses the generation of electric fields by time-varying magnetic fields. Equation 2.2 refers to the Ampere's law combining conduction and ldisplacement current components. Equation 2.3 and 2.4 refer to Gauss's law for electric and magnetic fields respectively. Equation 2.5 defines conservation of charge. The electric permittivity ε and magnetic permeability μ are defined to relate the electric flux density $\boldsymbol{D}$ to the electric field intensity $\boldsymbol{E}$ and magnetic flux density $\boldsymbol{B}$ to the magnetic field intensity $\boldsymbol{H}$ by equations:

$$\boldsymbol{D} = \varepsilon\boldsymbol{E} = \varepsilon_r\varepsilon_0\boldsymbol{E} \tag{2.8}$$

$$\boldsymbol{B} = \mu\boldsymbol{H} = \mu_r\mu_0\boldsymbol{H} \tag{2.9}$$

where $\varepsilon_0 \approx 8.854 \times 10^{-12}$ F/m is the permittivity of free space and ε_r refers to the normalised material constant with respect to the free space; $\mu_0 = 4\pi \times 10^{-7}$ H/m is the permeability of free space and μ_r refers to the relative permeability in the medium.

While equations 2.1 to 2.7 describe explicitely field vectors at any point of space at any time, Maxwell's equations can also be expressed in integral form applicable to overall regions of space:

$$\iint_S \nabla \times \boldsymbol{E} \cdot d\boldsymbol{S} = \oint_C \boldsymbol{E} \cdot d\boldsymbol{l} = \iint_S \frac{\partial \boldsymbol{B}}{\partial t} d\boldsymbol{S} \tag{2.10}$$

$$\iint_S \nabla \times \boldsymbol{H} \cdot d\boldsymbol{S} = \oint_C \boldsymbol{H} \cdot d\boldsymbol{l} = \iint_S (\boldsymbol{J} + \frac{\partial \boldsymbol{D}}{\partial t}) d\boldsymbol{S} \tag{2.11}$$

$$\oint\!\!\!\oint_S \boldsymbol{D} \cdot d\boldsymbol{S} = \iiint_V \rho \, dV \tag{2.12}$$

$$\oint\!\!\!\oint_S \boldsymbol{B} \cdot d\boldsymbol{S} = 0 \tag{2.13}$$

where equations 2.10 and 2.11 integrate equations 2.1 and 2.2 respectively over an open surface S bounded by a countour C while equations 2.12 and 2.13 integrate equations 2.3 and 2.4 respectively over a closed surface with an interior volume V.

The complex spatial forms of electromagnetic field vectors are introduced to simplify procedures when solving Maxwell's equations as the time variations of Electromagnetic waves are of consinusoidal forms

$$\boldsymbol{F}(x, y, z; t) = Re\left[\boldsymbol{F}(x, y, z)\, e^{j\omega t}\right] \tag{2.14}$$

where $\boldsymbol{F}$ refers to the field vectors and the term $j\omega$ replaces $\partial/\partial t$ in equations 2.1 - 2.5 and equations 2.10 - 2.11 to represent the time variations.

2.2 The Wave Equation and wave solutions

In order to solve for the electric and magnetic field in Maxwell's equations, it is necessary to transform the coupling first order partial differential equations in (2.1) and (2.2) to independent wave equations. First the phase form of Maxwell's equations for $\boldsymbol{E}$ and $\boldsymbol{H}$ are expressed as below:

$$\nabla \times \boldsymbol{E} = -j\omega \boldsymbol{B} \tag{2.15}$$

$$\nabla \times \boldsymbol{H} = \boldsymbol{J} + j\omega \boldsymbol{D} \tag{2.16}$$

Taking the curl of (2.15) and substitute the constitutive relationship for $\boldsymbol{B}$ gives:

$$\nabla \times \nabla \times \boldsymbol{E} = -j\omega\mu\nabla \times \boldsymbol{H} \tag{2.17}$$

Substitute (2.16) on the right-hand side and use the constitutive relationship for $\boldsymbol{D}$ and $\boldsymbol{J}$:

$$\nabla \times \nabla \times \boldsymbol{E} = \omega^2\mu\varepsilon\boldsymbol{E} - j\omega\mu\sigma\boldsymbol{E} \tag{2.18}$$

The generalized form of wave equation for $\boldsymbol{E}$ is then obtained by applying the vector identity $\nabla \times \nabla \times \boldsymbol{E} = \nabla\nabla \cdot \boldsymbol{E} - \nabla^2\boldsymbol{E}$ and substitute equations (2.3) and (2.8):

$$\nabla^2\boldsymbol{E} + k^2\boldsymbol{E} - j\omega\mu\sigma\boldsymbol{E} = \frac{\nabla\rho}{\varepsilon} \tag{2.19}$$

where $k = \omega\sqrt{\mu\varepsilon}$ represents the wavenumber that can also be obtained by $k = 2\pi/\lambda$. The wave equation for $\boldsymbol{H}$ is derived in the similar way and:

$$\nabla^2\boldsymbol{H} + k^2\boldsymbol{H} - j\omega\mu\sigma\boldsymbol{H} = 0 \tag{2.20}$$

The field vectors are therefore expressed independently and only related to the property of the medium and the charge density. These sets can be further simplified to homogeneous Helmholtz equations (2.21) and (2.22) by assuming a source-free, isotropic and homogeneous region, which is the main concern in this report.

$$\nabla^2 \boldsymbol{E} + k^2 \boldsymbol{E} = 0 \tag{2.21}$$

$$\nabla^2 \boldsymbol{H} + k^2 \boldsymbol{H} = 0 \tag{2.22}$$

The three-dimensional equations for $\boldsymbol{E}$ and $\boldsymbol{H}$ can be divided into two parts, one in the transverse plane and the other in the axial direction:

$$\nabla_t^2 \boldsymbol{\Psi} = -(k^2 - \beta^2)\boldsymbol{\Psi} \tag{2.23}$$

$$\frac{\partial^2 \boldsymbol{\Psi}}{\partial z^2} = -\beta^2 \boldsymbol{\Psi} \tag{2.24}$$

where $\boldsymbol{\Psi}$ is identified as $\boldsymbol{E}$ or $\boldsymbol{H}$, assuming the propagation function $e^{-j\beta z}$ in the z direction.

The solutions of equation (2.23) can be found by solving the z component of $\boldsymbol{E}$ and $\boldsymbol{H}$ and other components can be derived from these two components. In this report the local field solutions around cylindrical wires are concerned. Therefore the cylindrical coordinate system based on the wire centre is considered, as shown in Fig.2.1. In this case the transverse components of fields are E_ϕ and E_r and same

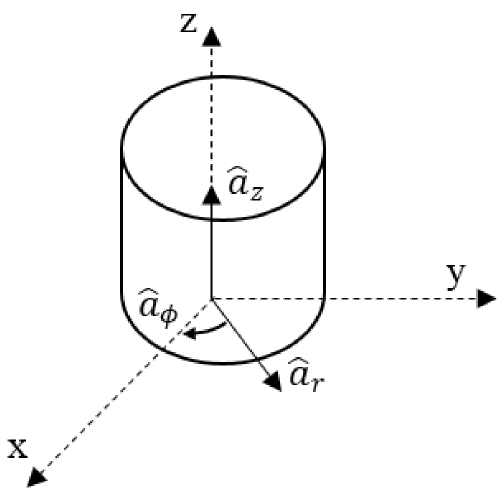

Figure 2.1 | Cylindrical coordinate system

for $\boldsymbol{H}$ components. Using the separation of variables method, the z-component can be derived in the form [2.2]:

$$E_z(r,\phi) = e^{-jn\phi}(AJ_n(k_c r) + BN_n(k_c r)) \tag{2.25}$$

where J_n and N_n are nth-order Bessel functions of first kind and second kind and A and B are the yet unknown coefficients. $k_c^2 = k^2 - \beta^2$ is the wave number in transverse plane. Due to the singularity of N_n at r=0, B is usually chosen as 0 when considering fields inside the cylinder. Hankel functions are the linear combinations of J_n and N_n in the form:

$$H_n^{(1)}(k_c r) = J_n(k_c r) + jN_n(k_c r) \tag{2.26}$$

$$H_n^{(2)}(k_c r) = J_n(k_c r) - jN_n(k_c r) \tag{2.27}$$

which are used in this report to represent fields outside the wire.

The transverse components can directly derived from E_z and H_z [2.2]:

$$E_r = -\frac{j}{k_c^2}\left(\beta\frac{\partial E_z}{\partial r} + \frac{\omega\mu}{r}\frac{\partial H_z}{\partial \phi}\right) \tag{2.28}$$

$$E_\phi = \frac{j}{k_c^2}\left(-\frac{\beta}{r}\frac{\partial E_z}{\partial \phi} + \omega\mu\frac{\partial H_z}{\partial r}\right) \tag{2.29}$$

$$H_r = \frac{j}{k_c^2}\left(\frac{\omega\varepsilon}{r}\frac{\partial E_z}{\partial \phi} - \beta\frac{\partial H_z}{\partial r}\right) \tag{2.30}$$

$$H_\phi = -\frac{j}{k_c^2}\left(\omega\varepsilon\frac{\partial E_z}{\partial r} + \frac{\beta}{r}\frac{\partial H_z}{\partial \phi}\right) \tag{2.31}$$

2.3 Boundary Conditions

In a region consisting of several media that have different material properties, which is denoted as μ and ε, the boundary condition of field solution on the adjacent sides of the boundary needs to be properly considered. Due to the fact that field functions and their derivatives are discontinuous across the boundary dividing two media, the integral form of Maxwell's equations stated previously is applied. An illustration of a surface diving the space into two regions with different media properties and field components is shown in Fig. (2.2). The integral form of Faraday's Law in(2.10)

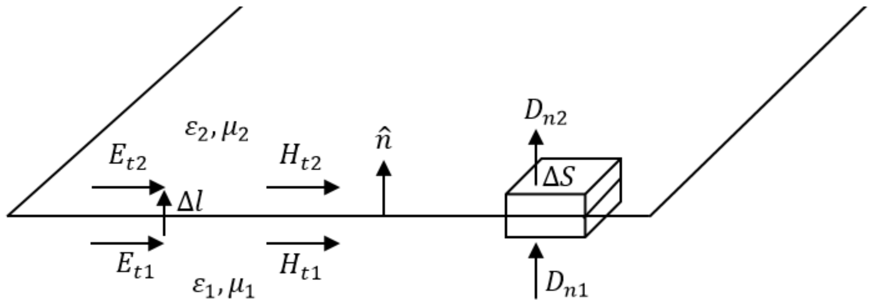

Figure 2.2 | Field and flux components on both sides of boundary

indicates an line integral of electric field along the path from one side of the boundary to the other and return with an infinitesimal distance Δl:

$$\oint \boldsymbol{E} \cdot dl = (E_{t1} - E_{t2})\Delta l \tag{2.32}$$

The infinitesimal length of Δl indicates an zero area enclosed by the path hence the magnetic flux change in the path can be regarded as zero. Therefore the change of tangential electric field presented in (2.32) can be considered zero hence the continuity of tangential components of electric field is confirmed:

$$E_{t1} - E_{t2} = 0 \quad or \quad \hat{n} \times (\boldsymbol{E}_1 - \boldsymbol{E}_2) = 0 \tag{2.33}$$

Similarly the integral form of Ampere's law shown in (2.11) provides a same result for tangential components of magnetic fields since the current density $\boldsymbol{J}$ and the rate of change of electric flux density $\frac{\partial \boldsymbol{D}}{\partial t}$ are finite:

$$H_{t1} - H_{t2} = 0 \quad or \quad \hat{n} \times (\boldsymbol{H}_1 - \boldsymbol{H}_2) = 0 \tag{2.34}$$

The integral form of Gauss's Law in (2.12) presents the normal component of electric flux density at both sides of the boundary in the form of:

$$D_{n1} - D_{n2} = \rho_S \tag{2.35}$$

which indicates a discontinuity condition of normal components of electric flux density due to the presence of surface charge density. This can be modified to be continuous in the case of charge-free boundary. Since the magnetic charge is assumed zero in this report as shown in (2.13), the magnetic flux density is continuous across the boundary:

$$B_{n1} - B_{n2} = 0 \tag{2.36}$$

A special case of boundary conditions is emphasized here when perfect conductors are involved in the problem space such as the presence of wires and metal components. Perfect conductors imply infinite conductivity hence drive zero electric and magnetic fields inside the conductor. Therefore to maintain the continuity at the boundary, the tangential components of electric fields and magnetic fields converge to zero at the boundary.

References

[2.1] R. E. Collin, *Field Theory of Guided Waves* (Wiley-IEEE Press, 1991), 2nd ed.

[2.2] S. Ramo, J. R. Whinnery, and T. Van Duzer, *Fields and waves in communication electronics* (John Wiley & Sons, 2008).

[2.3] J. G. Van Bladel, *Electromagnetic Fields*, IEEE Press Series on Electromagnetic Wave Theory (Wiley, 2007).

3

Local Field Solutions for Multi-Wire Systems

This chapter presents the formulation of local field solutions for two-dimensional multi-wire systems. This method solves wave propagation problems in the presence of wires. Cylindrical harmonics in the form of Bessel functions are employed to express general solutions for fields scattered by multiple conductor and modes of propagation are found in a numerical way. To start with, a two-wire system of perfect electric conductors (PEC) in homogeneous medium is studied. The system then extends to multiple conductors of various positions. Further more, the effect of dielectric coating around wires is considered. The method enables analysis of wave propagation within multi-core wire bundles of arbitrary shape and complex configurations.

***

3.1 Introduction

Local field solutions for thin wires have been applied in Transmission Line Modelling (TLM) method for modelling wire coupling problems in relatively coarse mesh environment [3.1–3.5]. In this thesis, the general approach for understanding wave propagation within a multi-core wire bundle is considered and the presence of dielectric coating is taken into consideration.

As is introduced in chapter (2), an electromagnetic wave can be divided into longitudinal component and transverse components. This way makes it easier to analyse the wave behaviour in the cross-sectional plane of multi-wire systems. The principle approach of finding appropriate field solutions for a multi-wire system is to find the correct longitudinal component of the wave number β and hence understand the mode of propagation. A numerical searching method is introduced to find correct values of β.

As described in the previous chapter, the general wave solution for scattered fields from wire conductors can be expressed as a series of Bessel or Hankel functions in the cylindrical coordinate system centred on the wire origin. Three field components are considered based on cylindrical coordinate system, Ψ_r the radial component, Ψ_ϕ the azimuthal component and Ψ_z the axial component. Ψ_z is the fundamental variable to be solved in the field solution and the other two components are able to be solved in terms of Ψ_z [3.6].

Boundary conditions are imposed on the interface of each wire to solve the unknown coefficients in the general solutions. For perfect electric conductors (PEC), due to the fact that there is no electric field inside the conductor, the tangential components of electric fields vanish on the conductor surface. When dielectric coating is presented, the boundary condition need be extended to the interface between the dielectric layer and the free space, thereby imposing the continuousness of tangential components of both electric and magnetic fields. For imperfect conductors, fields penetrate into the conductor and vanish exponentially. This is usually referred to the skin depth. The tangential electric and magnetic fields in such conductors also satisfy the continuous condition on the conductor interface.

Fig. 3.1 shows a general process to find the local fields solution for a multi-wire system. The boundary conditions for each wire form a square matrix corresponding to the specific value of β. The singular value decomposition method will be employed to find the determinant of the matrix in order to solve the boundary value problem. More details are discussed in subsequent sections regarding to different situations.

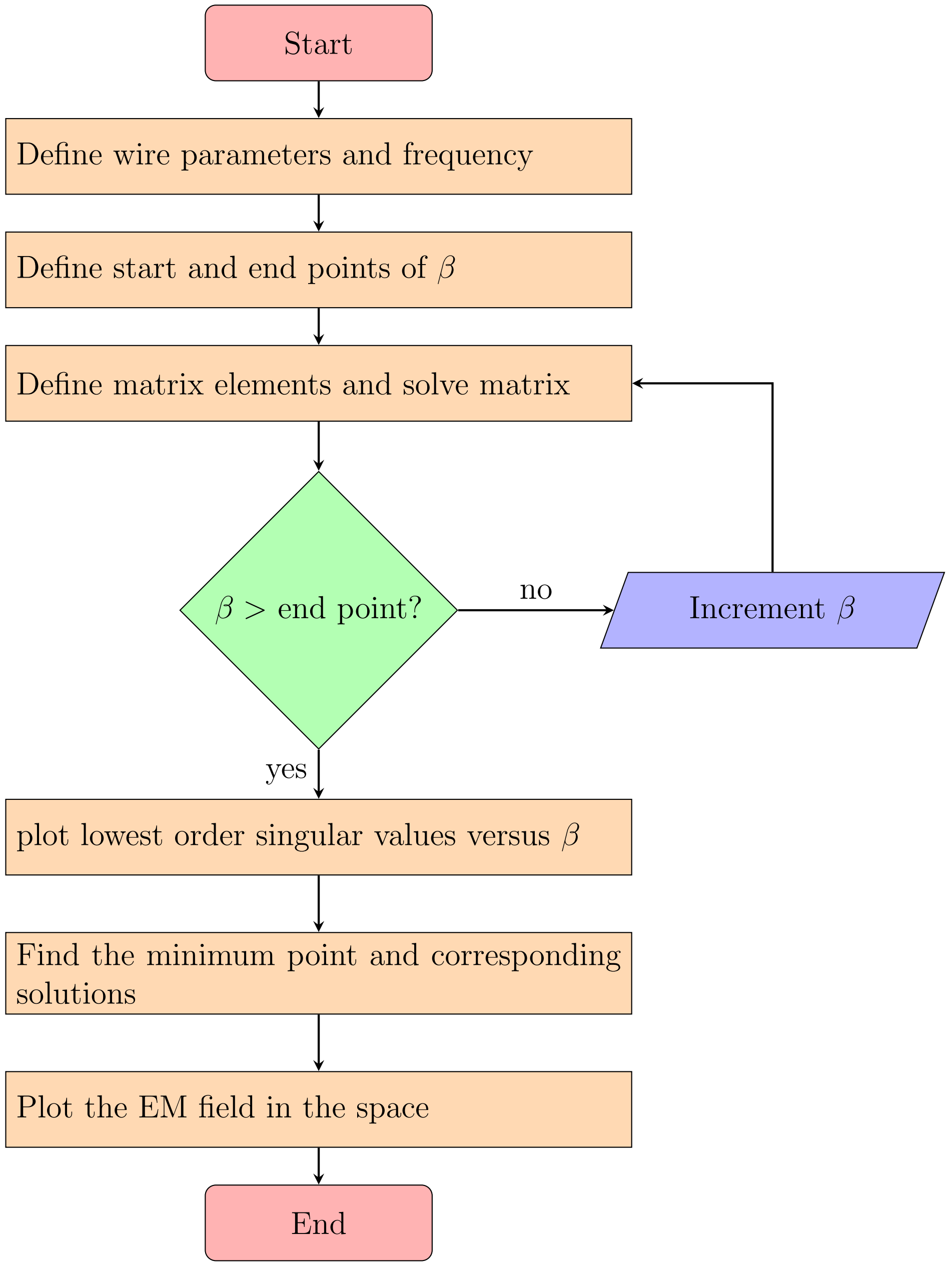

Figure 3.1 | Flow chart for local field solutions of a multi-wire system

3.2 Perfect Electric Conductor in Homogeneous medium

In this section, the general solution and formulations for PEC in homogeneous environment are introduced. Assuming that all wires have circular cross-section, the cylindrical coordinate system is employed. The wire origin is considered to be the origin of the coordinate system when looking at one specific wire. The general field solution in the transverse plane is expressed as a series of Bessel and Hankel functions related to the medium property and distance to the wire origin. A transformation formula is also introduced in order to express all fields with respect to the same coordinate system.

The axial component of electric and magnetic fields in the free space scattered by a wire conductor can be expressed as a series of Hankel functions of second kind in the cylindrical coordinate system centred on the wire origin:

$$\Psi_z = \sum_{n=-\infty}^{\infty} e^{-jn\phi} \frac{H_n^{(2)}(k_c r)}{H_n^{(2)}(k_c a)} X_n = \sum_{n=-\infty}^{\infty} f_n X_n = \boldsymbol{f}^T \boldsymbol{X} \tag{3.1}$$

where Ψ_z is identified as E_z or H_z component along z-direction. $f_n = e^{-jn\phi} \frac{H_n^{(2)}(k_c r)}{H_n^{(2)}(k_c a)}$ and X_n is the unknown coefficient. $k_c^2 = \omega^2 \mu \varepsilon - \beta^2$ is the wavenumber in the transverse plane and r is the distance from the observation point to the wire centre. The incident field is expressed as a series of Bessel functions of first kind centred on the TLM node centre:

$$F_i = \sum_{n=-\infty}^{\infty} e^{-jn\phi} \frac{J_n(kr)}{J_n(ka)} = \boldsymbol{g}_0^T \boldsymbol{X}_0 \tag{3.2}$$

The total field inside a mesh cell in the presence of several wires can be generalized as the superposition of total incident and scattered fields:

$$F_t = F_i + F_s \tag{3.3}$$

where t, i and s denote total, incident and scattered fields respectively. F_s is the sum of fields scattered by each individual wire in the model. At this stage the incident field and scattered fields are expressed with respect to their own coordinate system, therefore necessary transformation process must be carried out to express the total field in one coordinate system. The summation theorem for Bessel functions is utilised to address the transformation of field from one wire system to the desired coordinate system. Fig. 3.2 illustrates the relationship between two wires in cross section and the parameters used to process the transformation. For simplicity the example of two wires located arbitrarily in the x-y plane and off-site the centre are presented.

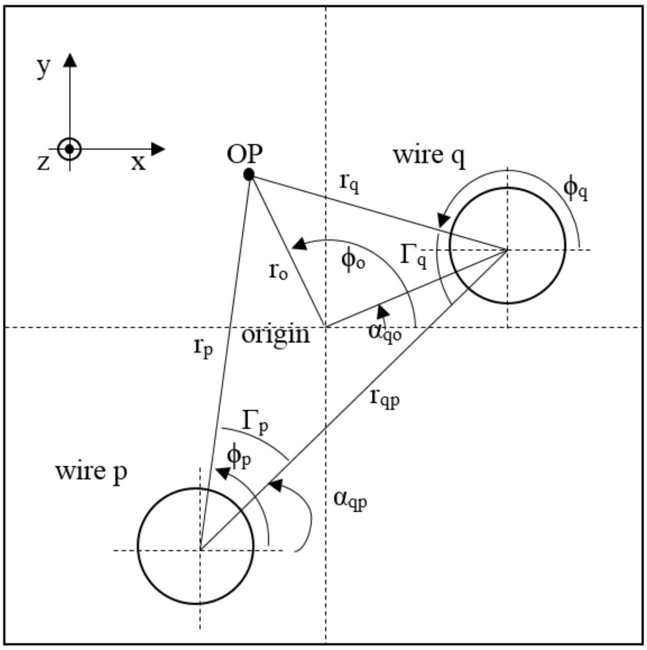

Figure 3.2 | TLM node embedding off-site thin wires

In Fig. 3.2 the reference wire is denoted as the wire p, and the transfer wire is denoted as the wire q. OP denotes the observation point hence r_p, r_q and r_o represent the distance between OP and p's centre, q's centre and node centre respectively. The radius of each wire is represented by a_p and a_q respectively. r_{qp} is the length between wire centres p and q and α_{qp} is the angle from positive x axes to r_{qp}. Γ_q and Γ_p

represent the angle between r_q, r_p and r_{qp} respectively. Therefore the field scattered from wire q at OP centred in wire p's coordinate system:

$$\begin{aligned} e^{-jn\phi_q}\frac{H_m^{(2)}(kr_q)}{H_m^{(2)}(ka_q)} &= \sum_{n=-\infty}^{\infty} e^{-j(m-n)\alpha_{qp}}\frac{J_n(kr_p)}{J_n(ka_p)}\frac{H_{m-n}^{(2)}(kr_{qp})}{H_m^{(2)}(ka_q)}J_n(ka_p)e^{-jn\phi_p} \\ &= \sum_{m=-\infty}^{\infty} e^{-jn\phi_p}\frac{J_n(kr_p)}{J_n(ka_p)}[T_{qp}]_{nm} \end{aligned} \tag{3.4}$$

where $[\boldsymbol{T}_{qp}]$ is called the transformation matrix with element

$$[T_{qp}]_{nm} = e^{-j(m-n)\alpha_{qp}}\frac{H_{m-n}(kr_{qp})}{H_m^{(2)}(ka_q)}J_n(ka_p)$$

Hence the total scattered field F_s in a multiconductor system can be expressed in the form:

$$\begin{aligned} F_s &= \boldsymbol{f}_p^T\boldsymbol{X}_p + \sum_{q\neq p}\boldsymbol{f}_q^T\boldsymbol{X}_q \\ &= \boldsymbol{f}_p^T\boldsymbol{X}_p + \sum_{q\neq p}\boldsymbol{g}_p^T\boldsymbol{T}_{qp}\boldsymbol{X}_q \end{aligned} \tag{3.5}$$

where $g_n = e^{-jn\phi}\frac{J_n(kr_p)}{J_n(ka_p)}$. Similarly the incident field in equation 3.2 with respect to the node centre is transformed to the coordinate system centred on the wire p:

$$F_i = \boldsymbol{g}_p^T\boldsymbol{U}_{0p}\boldsymbol{X}_0 \tag{3.6}$$

where

$$[U_{0p}]_{nm} = e^{-j(m-n)\phi_p}J_{m-n}(kr_{0p})$$

The total z-directional field distributed in the cross-sectional plane with respect to the cylindrical coordinate system centred on wire p can therefore be generalized:

$$F_t = \boldsymbol{g}_p^T\boldsymbol{U}_{0p}\boldsymbol{X}_0 + \boldsymbol{f}_p^T\boldsymbol{X}_p + \sum_{q\neq p}\boldsymbol{g}_p^T\boldsymbol{T}_{qp}\boldsymbol{X}_q \tag{3.7}$$

In this report, the static field solution with a source free environment is the main concern. Therefore the incident field, which is expressed as the first term in the equation above, is negligible. Once E_z and H_z are obtained, the other field components of electric and magnetic fields in the cylindrical coordinate can be solved using a straightforward transformation [3.6]:

$$E_r = -\frac{j}{k_c^2}\left(\beta\frac{\partial E_z}{\partial r} + \frac{\omega\mu}{r}\frac{\partial H_z}{\partial \phi}\right) \tag{3.8}$$

$$E_\phi = \frac{j}{k_c^2}\left(-\frac{\beta}{r}\frac{\partial E_z}{\partial \phi} + \omega\mu\frac{\partial H_z}{\partial r}\right) \tag{3.9}$$

$$H_r = \frac{j}{k_c^2}\left(\frac{\omega\varepsilon}{r}\frac{\partial E_z}{\partial \phi} - \beta\frac{\partial H_z}{\partial r}\right) \tag{3.10}$$

$$H_\phi = -\frac{j}{k_c^2}\left(\omega\varepsilon\frac{\partial E_z}{\partial r} + \frac{\beta}{r}\frac{\partial H_z}{\partial \phi}\right) \tag{3.11}$$

The next step is then to impose suitable boundary conditions in the model to characterize unknown coefficients in the equation (3.1).

3.2.1 Boundary Conditions

The general solutions of field distributions in the transverse plane is further analysed here to solve the fields around perfect electric conductors (PEC). Since the wave is scattered by the wire conductors, the boundary conditions at the surface of wires need to be specified. For perfect electric conductors (PEC), the tangential electric field, which consists of axial component E_z and azimuthal component E_ϕ, vanishes at the conductor surface. The azimuthal component of the electric field E_ϕ in cylindrical coordinate system can be derived explicitly by longitudinal electric field E_z and magnetic field H_z from equation (3.9) [3.6]:

$$E_\phi = \frac{j}{k_c^2}\left[\frac{\beta}{r}\frac{\partial E_z}{\partial \phi} + \omega\mu\frac{\partial H_z}{\partial r}\right] \tag{3.12}$$

where $k_c^2 = k_o^2 - \beta^2$ is the propagation constant in transverse plane. Two equations are imposed here to solve the unknown coefficients for E_z and H_z:

$$E_z = \boldsymbol{f}_p^T \boldsymbol{X}_{p(e_z)} + \sum_{q \neq p} \boldsymbol{g}_p^T \boldsymbol{T}_{qp} \boldsymbol{X}_{q(e_z)} = 0 \tag{3.13}$$

$$\begin{aligned} E_\phi = \frac{j}{k_c^2}\Bigg(- \frac{\beta}{r}\frac{\partial}{\partial \phi}\Big(\boldsymbol{f}_p^T \boldsymbol{X}_{p(e_z)} + \sum_{q \neq p} \boldsymbol{g}_p^T \boldsymbol{T}_{qp} \boldsymbol{X}_{q(e_z)}\Big) \\ + \omega\mu\Big(\boldsymbol{f}_p'^T \boldsymbol{X}_{p(h_z)} + \sum_{q \neq p} \boldsymbol{g}_p'^T \boldsymbol{T}_{qp} \boldsymbol{X}_{q(h_z)}\Big)\Bigg) = 0 \end{aligned} \tag{3.14}$$

Explicitly as a matrix,

$$\begin{bmatrix} f_{pn} & 0 & g_{pn}T_{pqnm} & 0 \\ -\frac{j}{k_c^2}\frac{\beta}{r}\frac{\partial f_{pn}}{\partial \phi} & \frac{j}{k_c^2}\omega\mu f'_{pn} & -\frac{j}{k_c^2}\frac{\beta}{r}\frac{\partial g_{pn}}{\partial \phi}T_{pqnm} & \frac{j}{k_c^2}\omega\mu g'_{pn}T_{pqnm} \\ g_{qn}T_{qpnm} & 0 & f_{qn} & 0 \\ -\frac{j}{k_c^2}\frac{\beta}{r}\frac{\partial g_{qn}}{\partial \phi}T_{qpnm} & \frac{j}{k_c^2}\omega\mu g'_q T_{qpnm} & -\frac{j}{k_c^2}\frac{\beta}{r}\frac{\partial f_{qn}}{\partial \phi} & \frac{j}{k_c^2}\omega\mu f'_{qn} \end{bmatrix} \begin{bmatrix} X_{pn(e_z)} \\ X_{pn(h_z)} \\ X_{qn(e_z)} \\ X_{qn(h_z)} \end{bmatrix} = \mathbf{0} \tag{3.15}$$

where $f_{pn} = e^{-jn\phi_p}\frac{H_n(kr_p)}{H_n(ka_p)}$, $g_{pn} = \frac{J_n(kr_p)}{J_n(ka_p)}$

The equation above can be solved when the matrix in equation 3.15 is singular. This is done by computing the singular value decomposition of the matrix and find the point of β when the singular value reaches minimum. The corresponding singular vector is then the demanding coefficient vector. Using the calculated coefficient vector, the field intensity at arbitrary point in the space can therefore be calculated using equation (3.1).

3.2.2 Two cores wire loom evaluation

This section presents the evaluation of a two-core wire loom example as shown in Fig. 3.3. Two cores with radius of 1mm are placed along x-axis in the transverse plane, with a separation distance 4mm between core centres.

The operating frequency for this model is chosen as $f = 1$ MHz, which gives an operation wavenumber in the free space by:

$$k_0 = \omega\sqrt{\mu_0\varepsilon_0} = 2\pi f\sqrt{\mu_0\varepsilon_0}$$

where $\mu_0 = 4\pi^{-7}H/m$ and $\varepsilon_0 \approx 8.854 \times 10^{-12}F/m$.

Following the flow chart shown in Fig. 3.1, the varying range of β is chosen from $0.95k_0$ to $1.1k_0$. Fig. 3.4 shows the singular value plot against β/k_0. The figure clearly shows the decreasing trend of singular values from $0.95k_0$ and reaches the minima near k_0. This point is therefore considered to be the desired value of β that solves the equation (3.15), and its corresponding singular vector is considered solutions of the coefficient vector $\boldsymbol{X}$. Once the coefficient vector in equation (3.15)

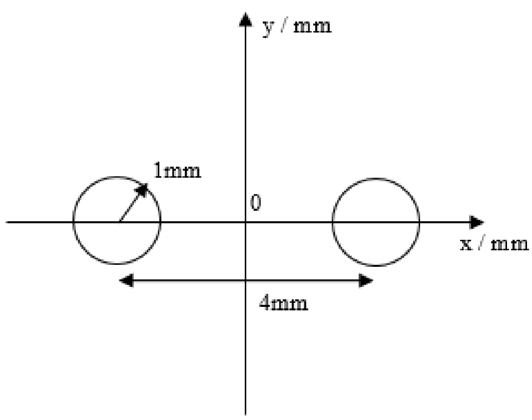

Figure 3.3 | Modelling example of a two-conductor line

is solved, the unique field solution is obtained by substituting back the coefficients to the general solution of axial field components E_z and H_z, which then derive the transverse field components E_ϕ, E_r, H_ϕ and H_r using equations (3.9), (3.8), (3.11) and (3.10). Fig. 3.5a and 3.5b show respectively, the magnitude of transverse electric field components and magnetic field components around wires.

For validation of the method, the characteristic impedance between to wires is cal-

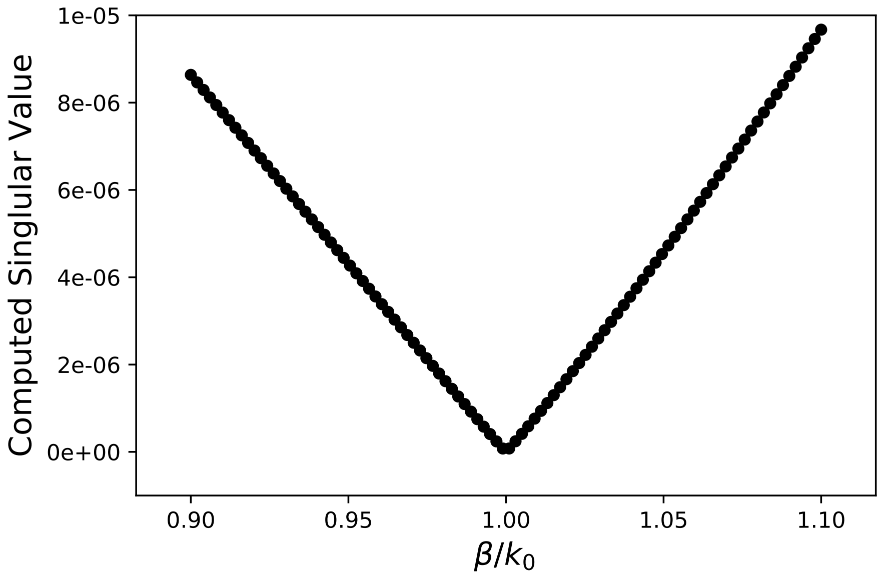

Figure 3.4 | Computed lowest order singular value against transverse propagation constant (β) normalised with respect to the wavenumber (k_0) in the air

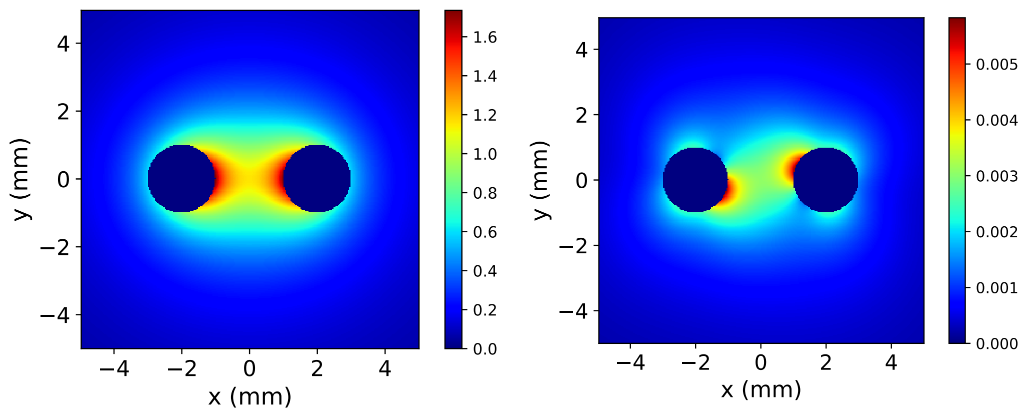

(a) Electric fields

(b) Magnetic fields

Figure 3.5 | Transverse electric and magnetic field distribution around wires in the cross-sectional plane

culated by computing:

$$Z_0 = \frac{V}{I}$$

where the voltage is obtained from integral of electric fields along the path between two wires and the current is obtained by integral of magnetic fields along the close path around each wire respectively. The theoretical value of characteristic impedance between two circular conductors can be calculated by [3.7]:

$$Z_{theory} = \frac{\eta}{\pi} acosh(\frac{D}{d}) = 157.9\Omega$$

Fig. 3.6 shows the convergence of computed impedances with increasing numbers of integration points for computing voltages and currents respectively. Although the figure shows convergence achieved over 300 points, the difference between 50 and 300 integration points is only 0.05%.

Fig. 3.7 shows the change of characteristic impedances due to increase of harmonic terms that describe the general field solution. It can be seen that the computational result is slightly lower than the theoretical value, but the difference is negligible. Besides, the convergence of impedance is obtained with more than 4 harmonic terms that describe the general field solutions in expression (3.1).

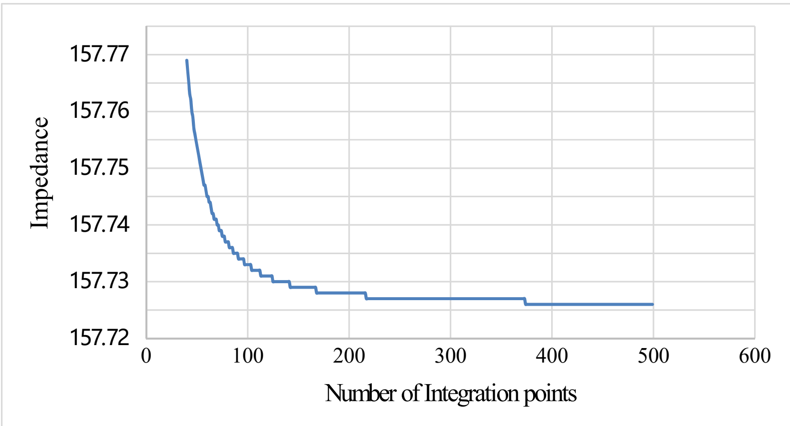

Figure 3.6 | Computed Impedance as a function of number of integration points for calculating voltage and current

Furthermore, the evaluation of impedances with various distance-to-diameter ratio and different frequencies is shown in Fig. 3.8 and 3.9. The accuracy of this method is demonstrated compared to theoretical values and the stability over different frequencies is observed.

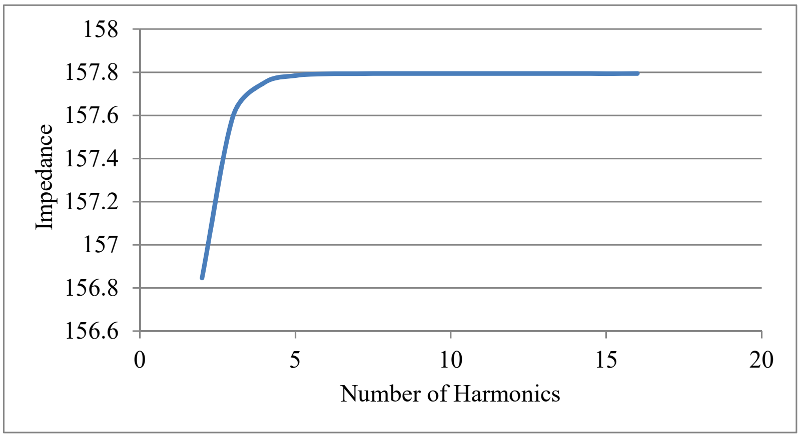

Figure 3.7 | Computed Impedance as a function of number of harmonic terms for field approximate expressions

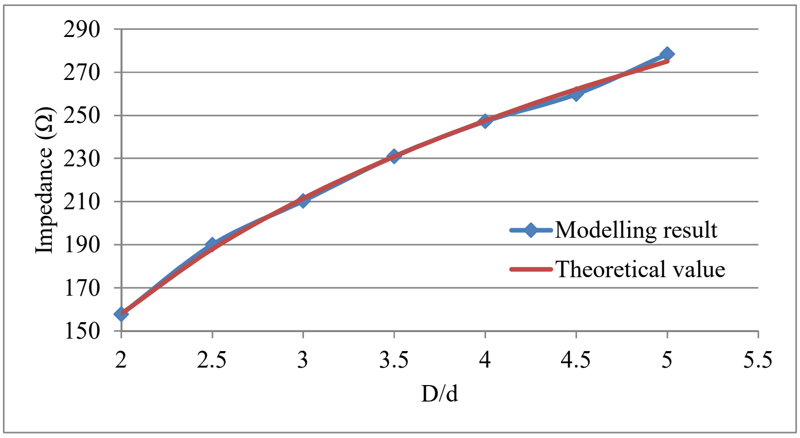

Figure 3.8 | Computed characteristic impedance (Z_0) as a function of wire separation-to-diameter (D/d) ratio

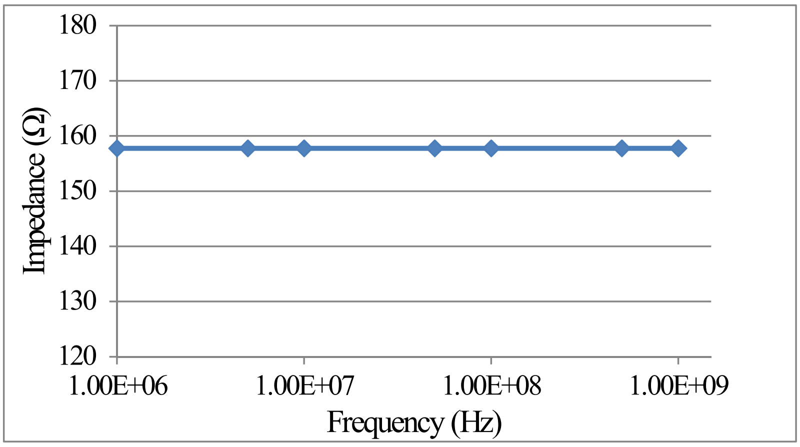

Figure 3.9 | Computed characteristic impedance (Z_0) as a function of operation frequency (f)

3.2.3 Three cores wire loom evaluation

The modelling of multi-core wire looms becomes more complicated due to the cross coupling between each conductor in the system, which increases the size of the matrix in equation (3.15). In this report two models of three-conductor lines are explored, one referred to the ribbon cable with three wires placed along the axis and the other placed asymmetrically in the space.

Fig. 3.10 shows the position of three wires placed aligned along the x-axis of the coordinate system, whose origin locates at the centre of the middle wire. The other two wires are placed 3mm away from the middle wire on the x-axis. The three wires have the same radius of 1mm.

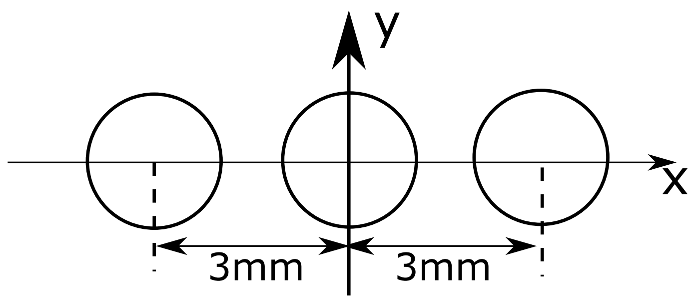

Figure 3.10 | Cross section of three wires on x-axis

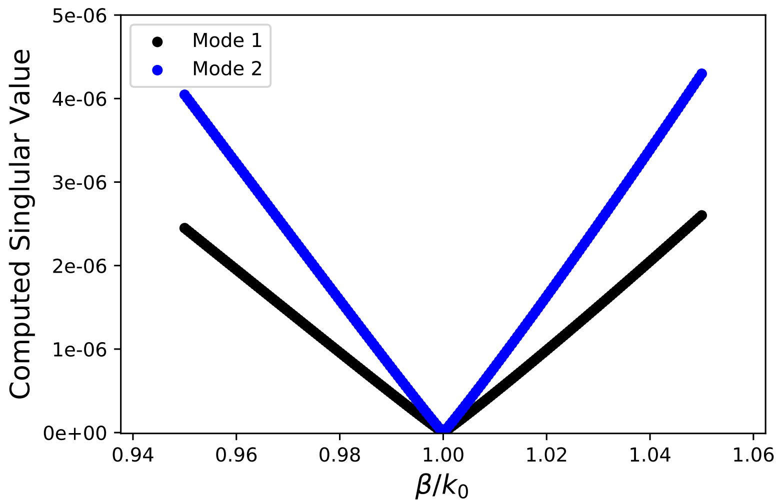

Figure 3.11 | Two sets of computed singular values against transverse propagation constant (β) normalised with respect to the wavenumber (k_0) in the air

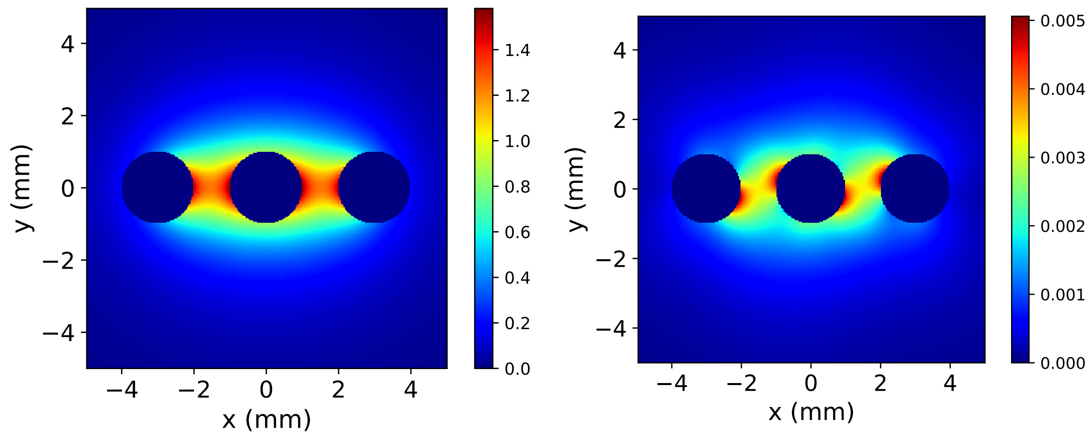

(a) Transverse electric field

(b) Transverse magnetic field

Figure 3.12 | Transverse Field plot for the first mode

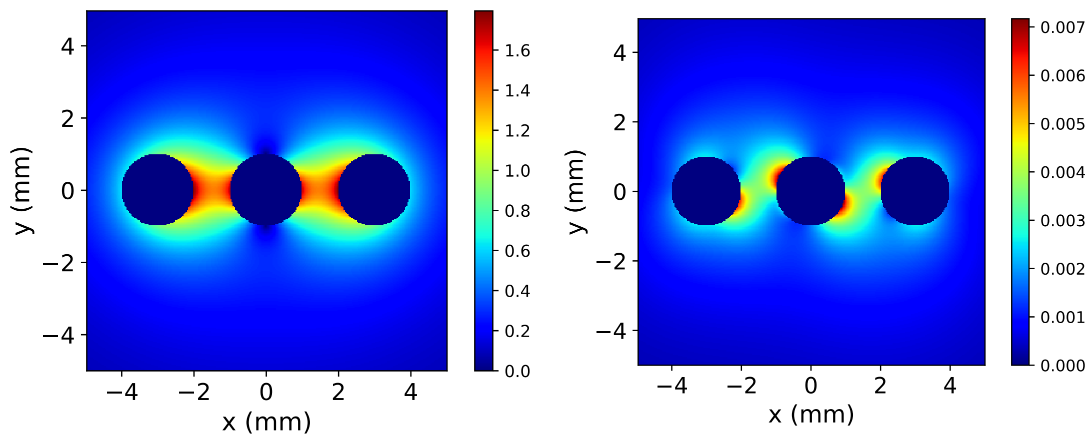

(a) Transverse electric field

(b) Transverse magnetic field

Figure 3.13 | Transverse Field plot for the second mode

The plot of singular values for the symmetrical model in Fig. 3.11 shows two curves of singular values with same values of β at the minima. The corresponding coefficient vectors obtained with respect two modes above provide two sets of field solutions that fit the wave equation and boundary condition requirement. The field magnitude distribution are shown in Fig. 3.12 and 3.13.

Another example is three wires locating asymmetrically in the coordinate system, with the cross section as shown in Fig. 3.14. Two wires sit on the x-axis, with a distance of 3mm away from the coordinate origin and the third locates at the coordinates (1,3).

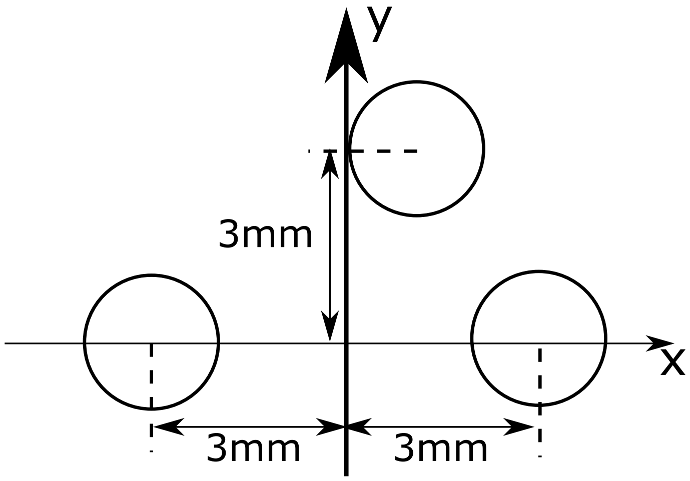

Figure 3.14 | **Cross section of three wires with asymmetrical position**

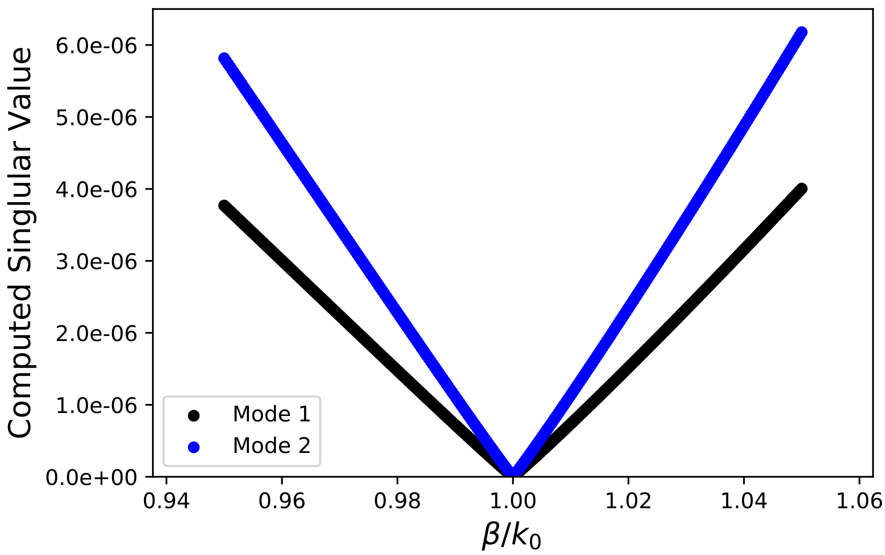

Figure 3.15 | Singular value plot against the transverse propagation constant (β) normalised with respect to the wavenumber in the air (k_0)

The singular value plot in Fig. 3.15 shows again two curves that reaches the same minima at $\beta = k_0$, which are considered two modes of field solutions for this model.

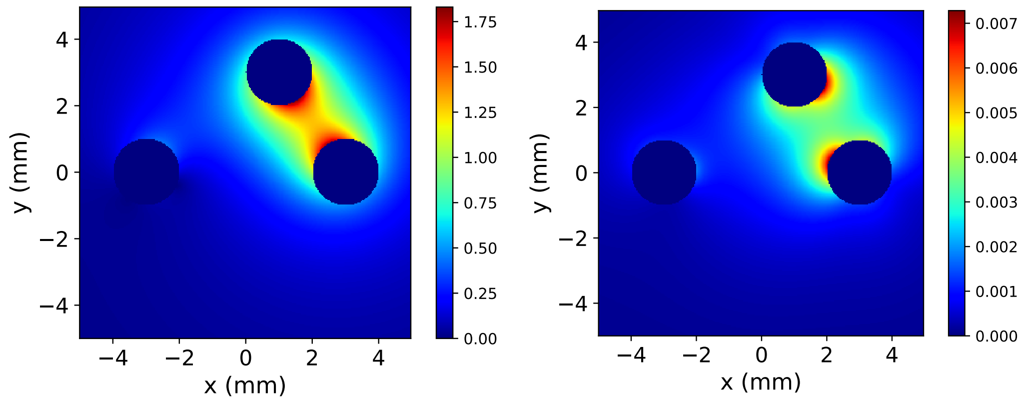

(a) Transverse electric field

(b) Transverse magnetic field

Figure 3.16 | Transverse Field plot for the first mode

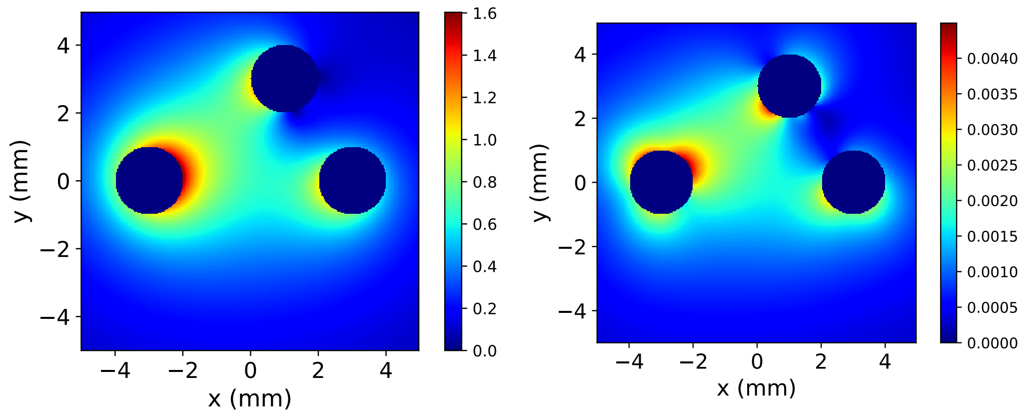

(a) Transverse electric field

(b) Transverse magnetic field

Figure 3.17 | Transverse Field plot for the second mode

The magnitude of transverse electric and magnetic fields are plot in Fig. 3.16 and 3.17 respectively.

It can be seen that for multi-core wire loom systems consisting of PECs in homogeneous medium, the longitudinal component of the propagation constant is same as the wavenumber in that medium. This field propagation follows the Transverse Electromagnetic (TEM) rule, with zero longitudinal electric and magnetic field components and standing transverse field components. When more wire conductors added to the system, it is expected to see more distribution modes of transverse field components.

3.3 PEC in Inhomogeneous Medium

The effect of dielectric coating surrounding wires is explored in this section, with the inside conductor remaining PEC. Fig. 3.18 shows a basic two wire coupling model with dielectric coating around each wire. Where ε_0 denotes the electric permittivity

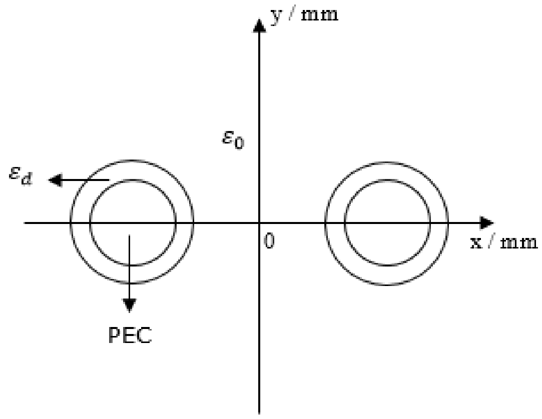

Figure 3.18 | Wires with dielectric coating

in the free space and ε_d indicates the electric permittivity in the dielectric coating layer. For such wires with inhomogeneous medium presented, boundary conditions need to be imposed on any interface that exhibits different medium properties. The field outside the wire is still expressed in terms of Hankel functions of second kind, as presented in equation (3.1) and (3.5) for total scattered field. The field inside the dielectric region imposes a different medium property, mainly the change of the permittivity ε_d, which is shown in Fig. 3.18, and does not couple to the scattered field from other wires. It can be expressed in terms of the sum of Bessel functions of the first kind and the second kind:

$$\Psi_z = \sum_{n=-\infty}^{\infty} e^{-jn\phi}\left(\frac{J_n(k_{cd}r)}{J_n(k_{cd}a_1)}A_n + \frac{N_n(k_{cd}r)}{N_n(k_{cd}a_1)}B_n\right) = \sum_{n=-\infty}^{\infty} gj_nA_n + gy_nB_n = \boldsymbol{gj}^T\boldsymbol{A} + \boldsymbol{gy}^T\boldsymbol{B} \tag{3.16}$$

where $k_{cd}^2 = \omega^2\mu\varepsilon_d - \beta^2$. $gj_n = e^{-jn\phi}\frac{J_n(k_{cd}r)}{J_n(k_{cd}a_1)}$ and $gy_n = e^{-jn\phi}\frac{N_n(k_{cd}r)}{N_n(k_{cd}a_1)}$. A_n and B_n are the unknown coefficients.

In general, the longitudinal field component at an arbitrary point in the cross-sectional plane can be identified according to its medium material:

$$\Psi_z = \begin{cases} 0 & \text{conductor} \\ \boldsymbol{gj}^T \boldsymbol{A}_p + \boldsymbol{gy}^T \boldsymbol{B}_p & \text{dielectric} \\ \boldsymbol{f}_p^T \boldsymbol{X}_p + \sum_{q \neq p} \boldsymbol{g}_p^T \boldsymbol{T}_{qp} \boldsymbol{X}_q & \text{air} \end{cases} \tag{3.17}$$

The transverse components in cylindrical coordinates are easily derived using equations (3.8 - 3.11).

3.3.1 Boundary Conditions

Due to the presence of the dielectric coating, the boundary condition and thereby the equation for field solutions become more complicated. Each boundary in the system needs to be evaluated. On the interface of the conductor and the dielectric layer, the tangential electric field components, E_z along axial axis and E_ϕ in the transverse plane, are enforced to vanish. Assuming the radius at the inner surface is a_1, the equation for the boundary condition at $r = a_1$ is given by:

$$E_z = \boldsymbol{gj}_p^T \boldsymbol{A}_{p(e_z)} + \boldsymbol{gy}_p^T \boldsymbol{B}_{p(e_z)} = 0 \tag{3.18}$$

$$E_\phi = \frac{j}{k_c^2}\Big(-\frac{\beta}{a_1}\frac{\partial}{\partial \phi}\Big(\boldsymbol{gj}_p^T \boldsymbol{A}_{p(e_z)} + \boldsymbol{gy}_p^T \boldsymbol{B}_{p(e_z)}\Big) + \omega\mu\Big(\boldsymbol{gj}_p'^T \boldsymbol{A}_{p(h_z)} + \boldsymbol{gy}_p'^T \boldsymbol{B}_{p(h_z)}\Big)\Big) = 0 \tag{3.19}$$

where $\boldsymbol{A_{p(e_z)}}$, $\boldsymbol{B_{p(e_z)}}$, $\boldsymbol{A_{p(h_z)}}$, $\boldsymbol{B_{p(h_z)}}$ denote the coefficient vector of axial field components from the p^{th} wire for both electric (e_z) and magnetic fields (h_z) respectively.

On the interface between the free space and the dielectric layer, the tangential components of both electric and magnetic fields are required to be continuous across the interface. This imposes four field continuity equations, assuming the radius of the outer layer of the wire is a_2, expressed as:

$$E_z(k_{cd}a_2) \; - \; E_z(k_{co}a_2) = 0 \tag{3.20}$$

$$E_\phi(k_{cd}a_2) \; - \; E_\phi(k_{co}a_2) = 0 \tag{3.21}$$

$$H_z(k_{cd}a_2) \; - \; H_z(k_{co}a_2) = 0 \tag{3.22}$$

$$H_\phi(k_{cd}a_2) \; - \; H_\phi(k_{co}a_2 = 0 \tag{3.23}$$

where k_{cd} and k_{co} are the transverse wavenumber in the dielectric and the air respectively. E_z and H_z are obtained from equation 3.17 and they are further utilised to derive E_ϕ and H_ϕ components using equations (3.9) and (3.11). Consequently the boundary equations become a series of equations related to longitudinal components only:

$$\{E_z\} \qquad (\boldsymbol{gj}_p^T\boldsymbol{A}_{p(e_z)} + \boldsymbol{gy}_p^T\boldsymbol{B}_{p(e_z)}) \; - \; (\boldsymbol{f}_p^T\boldsymbol{X}_{p(e_z)} + \sum_{q\neq p}\boldsymbol{g}_p^T\boldsymbol{T}_{qp}\boldsymbol{X}_{q(e_z)}) = 0 \tag{3.24}$$

$$\begin{aligned}\{E_\phi\} \quad & \frac{j}{k_{cd}^2}\Bigg(-\frac{\beta}{a_2}\frac{\partial}{\partial\phi}\Bigg(\big(\boldsymbol{gj}_p^T\boldsymbol{A}_{p(e_z)} + \boldsymbol{gy}_p^T\boldsymbol{B}_{p(e_z)}\big) - \Bigg(\boldsymbol{f}_p^T\boldsymbol{X}_{p(e_z)} + \sum_{q\neq p}\boldsymbol{g}_p^T\boldsymbol{T}_{qp}\boldsymbol{X}_{q(e_z)}\Bigg)\Bigg) \\ & +\omega\mu\Bigg(\big(\boldsymbol{gj}_p'^T\boldsymbol{A}_{p(h_z)} + \boldsymbol{gy}_p'^T\boldsymbol{B}_{p(h_z)}\big) - \Bigg(\boldsymbol{f}_p'^T\boldsymbol{X}_{p(h_z)} + \sum_{q\neq p}\boldsymbol{g}_p'^T\boldsymbol{T}_{qp}\boldsymbol{X}_{q(h_z)}\Bigg)\Bigg)\Bigg) = 0\end{aligned} \tag{3.25}$$

$$\{H_z\} \qquad (\boldsymbol{gj}_p^T\boldsymbol{A}_{p(h_z)} + \boldsymbol{gy}_p^T\boldsymbol{B}_{p(h_z)}) \; - \; (\boldsymbol{f}_p^T\boldsymbol{X}_{p(h_z)} + \sum_{q\neq p}\boldsymbol{g}_p^T\boldsymbol{T}_{qp}\boldsymbol{X}_{q(h_z)}) = 0 \tag{3.26}$$

$$\begin{aligned}\{H_\phi\} \quad & -\frac{j}{k_{cd}^2}\Bigg(\omega\varepsilon_d\big(\boldsymbol{gj}_p'^T\boldsymbol{A}_{p(e_z)} + \boldsymbol{gy}_p'^T\boldsymbol{B}_{p(e_z)}\big) - \omega\varepsilon_o\Bigg(\boldsymbol{f}_p'^T\boldsymbol{X}_{p(e_z)} + \sum_{q\neq p}\boldsymbol{g}_p'^T\boldsymbol{T}_{qp}\boldsymbol{X}_{q(e_z)}\Bigg) \\ & +\frac{\beta}{a_2}\frac{\partial}{\partial\phi}\Bigg(\big(\boldsymbol{gj}_p^T\boldsymbol{A}_{p(h_z)} + \boldsymbol{gy}_p^T\boldsymbol{B}_{p(h_z)}\big) - \Bigg(\boldsymbol{f}_p^T\boldsymbol{X}_{p(h_z)} + \sum_{q\neq p}\boldsymbol{g}_p^T\boldsymbol{T}_{qp}\boldsymbol{X}_{q(h_z)}\Bigg)\Bigg)\Bigg) = 0\end{aligned} \tag{3.27}$$

Combing equations above with equations for the first layer boundary in (3.18) and (3.19), a matrix equation can be derived in the form:

$$\begin{bmatrix} \boldsymbol{A}_{pn} & \boldsymbol{T}_{pqnm} & \cdots \\ \boldsymbol{T}_{qpnm} & \boldsymbol{A}_{qn} & \cdots \\ \vdots & \vdots & \ddots \end{bmatrix} \begin{bmatrix} \boldsymbol{X}_{pn} \\ \boldsymbol{X}_{qn} \\ \vdots \end{bmatrix} = \mathbf{0} \tag{3.28}$$

where $\boldsymbol{A}_{pn}$ is referred to the element block of the p^{th} wire of the n^{th} harmonic and $\boldsymbol{T}_{pqnm}$ is referred to the transfer elements of the q^{th} wire of the m^{th} order transferred to the cylindrical coordinate centred on the p^{th} wire of the n^{th} harmonic. More explicitly,

$$\begin{bmatrix} \boldsymbol{A}_{pn} \end{bmatrix} = \begin{bmatrix} gj & gy & 0 & 0 & 0 & 0 \\ \frac{\partial gj}{\partial \phi} & \frac{\partial gy}{\partial \phi} & gj' & gy' & 0 & 0 \\ gj & gy & 0 & 0 & -f & 0 \\ 0 & 0 & gj & gy & 0 & -f \\ \frac{\partial gj}{\partial \phi} & \frac{\partial gy}{\partial \phi} & gj' & gy' & -\frac{\partial f}{\partial \phi} & -f' \\ gj' & gy' & \frac{\partial gj}{\partial \phi} & \frac{\partial gy}{\partial \phi} & -f' & -\frac{\partial f}{\partial \phi} \end{bmatrix} \tag{3.29}$$

$$\begin{bmatrix} \boldsymbol{T}_{pqnm} \end{bmatrix} = \begin{bmatrix} 0 & 0 & 0 & 0 & 0 & 0 \\ 0 & 0 & 0 & 0 & 0 & 0 \\ 0 & 0 & 0 & 0 & -gT_{pqnm} & 0 \\ 0 & 0 & 0 & 0 & 0 & -gT_{pqnm} \\ 0 & 0 & 0 & 0 & -\frac{\partial g}{\partial \phi}T_{pqnm} & -g'T_{pqnm} \\ 0 & 0 & 0 & 0 & -g'T_{pqnm} & -\frac{\partial g}{\partial \phi}T_{pqnm} \end{bmatrix} \qquad \begin{bmatrix} \boldsymbol{X}_{pn} \end{bmatrix} = \begin{bmatrix} A_{p(e_z)} \\ B_{p(e_z)} \\ A_{p(h_z)} \\ B_{p(h_z)} \\ X_{p(e_z)} \\ X_{p(h_z)} \end{bmatrix} \tag{3.30}$$

where $gj_{pn} = e^{-jn\phi}\frac{J_n(k_{c2}r)}{J_n(k_{c2}a_1)}$, $gy_{pn} = e^{-jn\phi}\frac{N_n(k_{c2}r)}{N_n(k_{c2}a_1)}$, $f_{pn} = e^{-jn\phi}\frac{H_n(k_{co}r)}{H_n(k_{co}a_2)}$ and $g_{pn} = e^{-jn\phi}\frac{J_n(k_{co}r)}{J_n(k_{co}a_2)}$. The size of each block, according to the number of equations, is $6 \times 6 = 36$. Therefore the total size of the matrix in equation 3.28, depending on the number of wires x in the system and the number of harmonic terms n for the expression, can be found as $(x \times n \times 6)$ by $(x \times n \times 6)$.

3.3.2 Two cores wire loom evaluation

The mode searching and field solutions for a two-core wire loom with dielectric coating is presented in this section. The operation frequency is set as 1 MHz. The longitudinal propagation constant β with respect to the wave number k_0 in the free space is searched. The resultant field solutions are obtained from the computed β and plot in the transverse plane. For the purpose of validating the modelling result, the continuity condition at the boundary interface is explored. A straightforward way is to plot $\varepsilon_r E_x$ along x-axis, where E_x denotes normal electric field along x-axis, for the normal component of the electric flux density $\boldsymbol{D} = \varepsilon \boldsymbol{E}$ is continuous in a charge free boundary according to section 2.3.

Similar to the homogeneous case, the wires are placed along x-axis in the cross-sectional plane, with a separation distance 4 mm between two centres as shown in Fig. 3.18. The conductor radius is set 1 mm and the coating thickness is set 0.2mm. The relative permittivity in the dielectric layer is set as $\varepsilon_d = 2.25$.

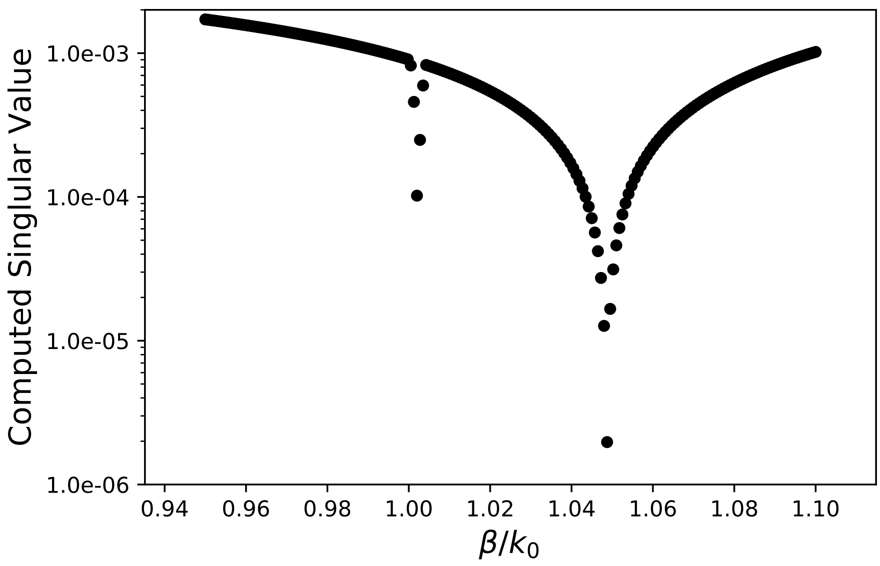

Figure 3.19 | Singular value plot against β/k_o

First the proper mode of the system is found by varying longitudinal propagation constant β with respect to the overall wave number k_0 in the free space and finding the minimum singular value point for the matrix equation 3.28. Fig. 3.19 illustrates two local minimum in the search domain. One locates at the point $\beta/k_0 = 1$ and the other at the point $\beta/k_0 = 1.04874$. Further study indicates that the first minimum point is not a mode but a fact caused by the term $1/k_c^2$ in the equations. Therefore the second minimum point is found to be the only mode in a two-conductor wire system. Compared to the homogeneous case in the previous section, the value of *beta* shifts to the right of k_0, but lower than k_r for the dielectric medium. This addresses the effect of dielectric coating around conductors on the wave propagation.

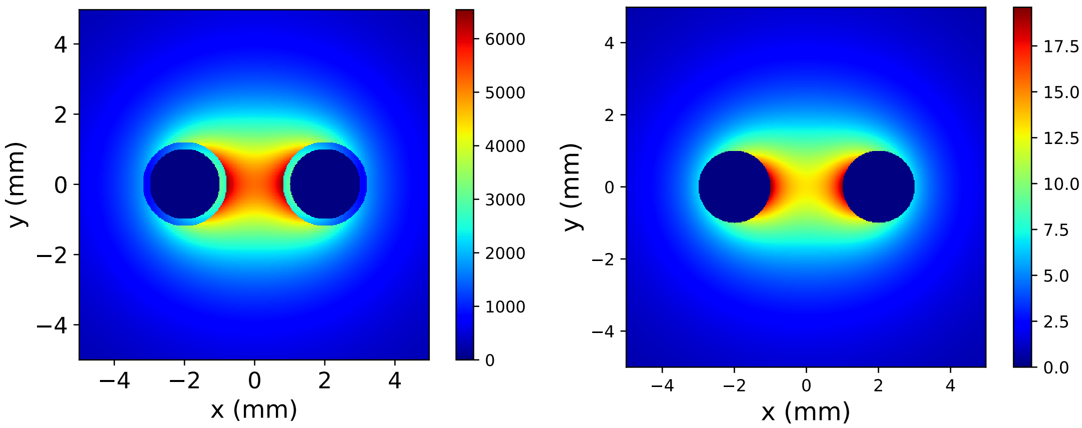

(a) Transverse electric field

(b) Transverse magnetic field

Figure 3.20 | Transverse Field plot for two cores wire loom with dielectric coating

Fig. 3.20 shows the transverse electric and magnetic field plot in the cross-sectional plane. Due to the discontinuity of electric permittivity around two wires, the electric field experiences discontinuity at the interface between the dielectric layer and the air. However since the dielectric is not ferromagnetic and has a permeability of free space, the magnetic field distribution shown in Fig. 3.20b does not see any boundary of medium change. Fig. 3.21 demonstration the validation of the mode by showing the continuity of normal electric flux components across the dielectric-air interface.

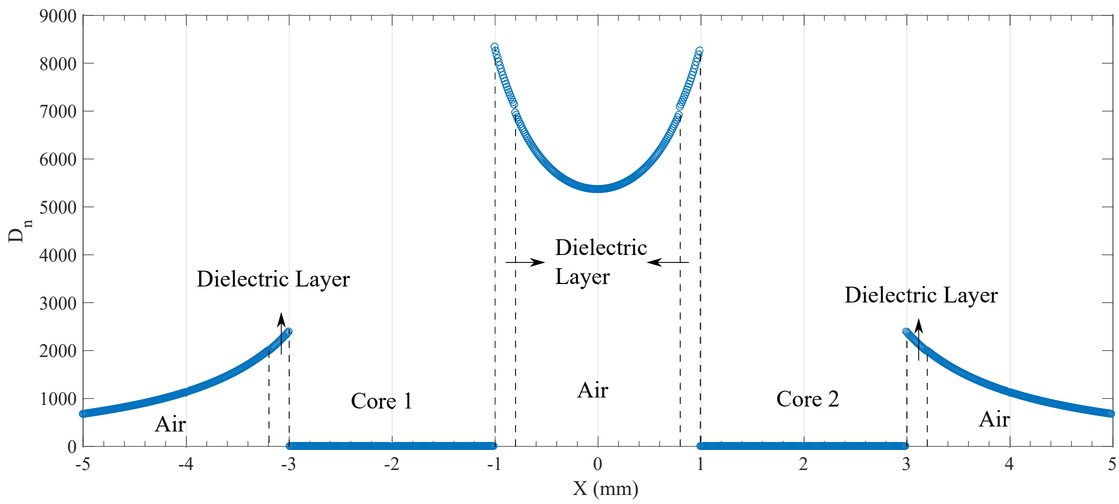

Figure 3.21 | Normal electric flux (D_n) along x axes

3.4 Three cores wire loom evaluation

In this section two sets of three-core wire looms, with symmetrical and asymmetrical positioning respectively, are explored. In the first model the three wires are placed horizontally along the x axis, with a separation distance 3 cm between two adjacent wires, as shown in Fig. 3.22a. The second model moves the middle wire to the place (1,3) in the coordinate systemand keeps the other two wires unmoved, as shown in Fig. 3.22b. Both cases have same wire radius 1 mm and perfect electric conductivity. Dielectric coating is applied to each wire, with thickness 0.2 mm and relative permittivity $\varepsilon = 2.25$

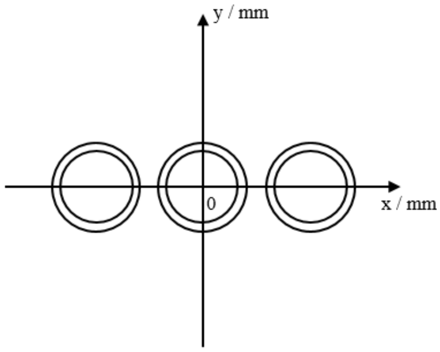

(a) Model 1

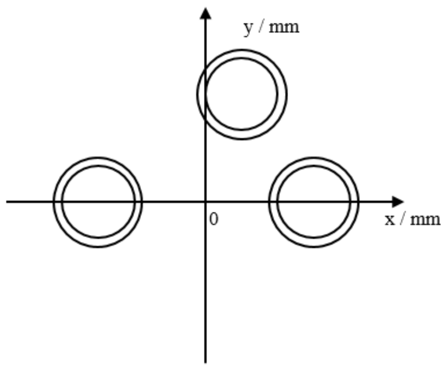

(b) Model 2

Figure 3.22 | Cross section of three-wire system with a) horizontally placed, b) arbitrary placed

Fig. 3.23 shows the lowest order singular value plot against the ratio of longitudinal propagation constant (β) over the total propagation constant in the free space (k_0). It can be seen that three local minima are displayed in the figure. Again, the point at $\beta = k_0$ is found to be caused by the term $1/k_c^2$ in equations when $\beta = k_0$ and therefore is not considered to be a solution. The other two minima indicate two explicit modes at $\beta = 1.068k_0$ and $\beta = 1.095k_0$ respectively. It is observed that in the presence of dielectric coating, the value of β exceeds k_0 in order to achieve desired boundary conditions at the surface between the dielectric layer and the air.

Fig. 3.24 and 3.25 plots the electric and magnetic field around three wire in the transverse plane for the two modes respectively. Similar results to the models without dielectric coating in section (3.2.3) are found , apart from the discontinuity of electric fields in different media due to change of electric permittivity.

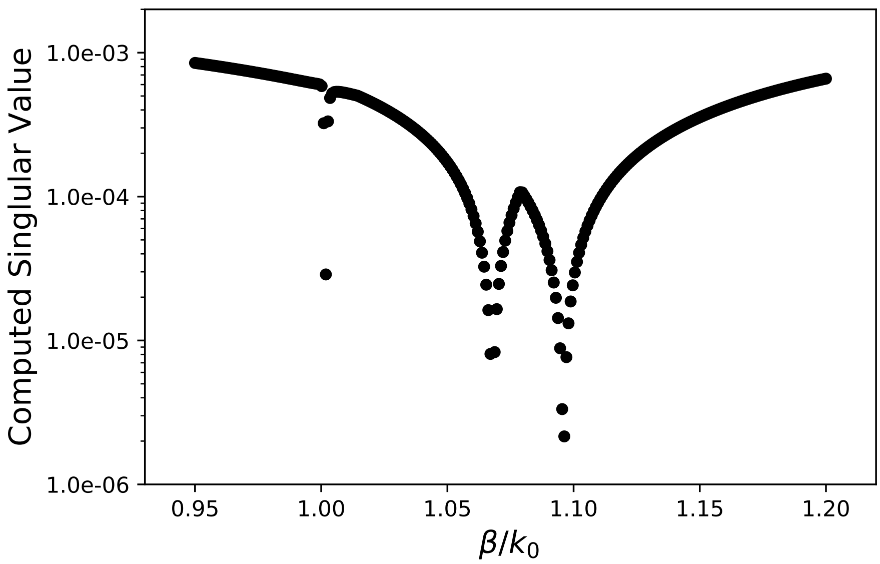

Figure 3.23 | Singular value plot against β/k_o

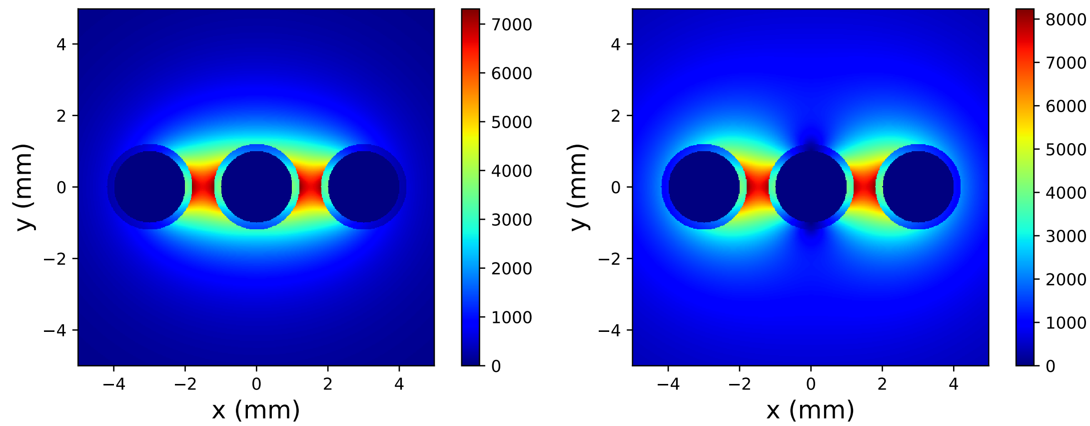

(a) Mode 1

(b) Mode 2

Figure 3.24 | Transverse Electric Field (E_t) distribution in the space

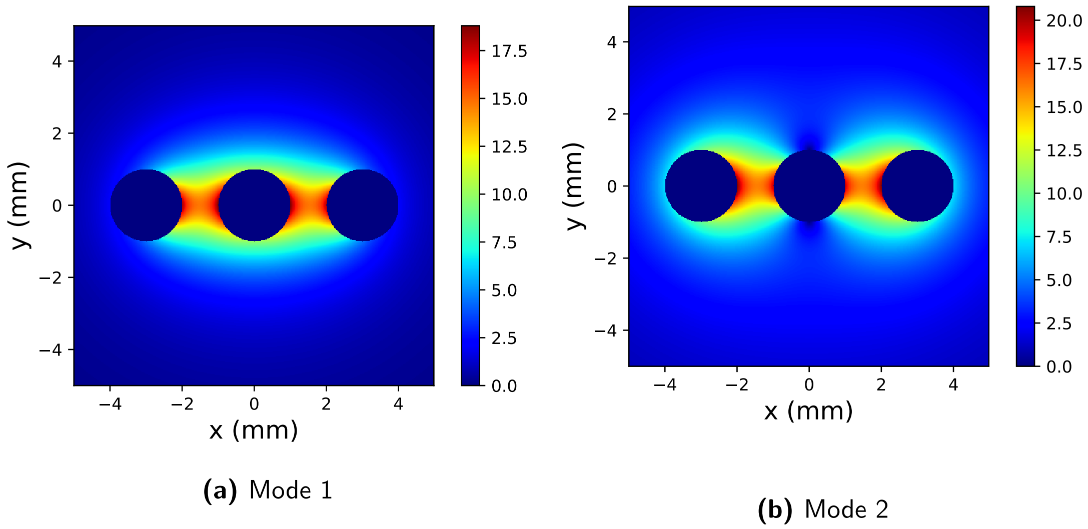

Figure 3.25 | Transverse Magnetic Field (H_t) distribution in the space

Fig. 3.26 presents the lowest singular value plot of second three-wire loom model as shown in Fig. 3.22b, Two modes of propagation with $\beta = 1.035k_0$ and $\beta = 1.057k_0$ respectively. It can be seen that the change of position of wires in the space affect the propagation constant. Fig. 3.27 and 3.28 show the transverse electric and magnetic fields for each mode respectively.

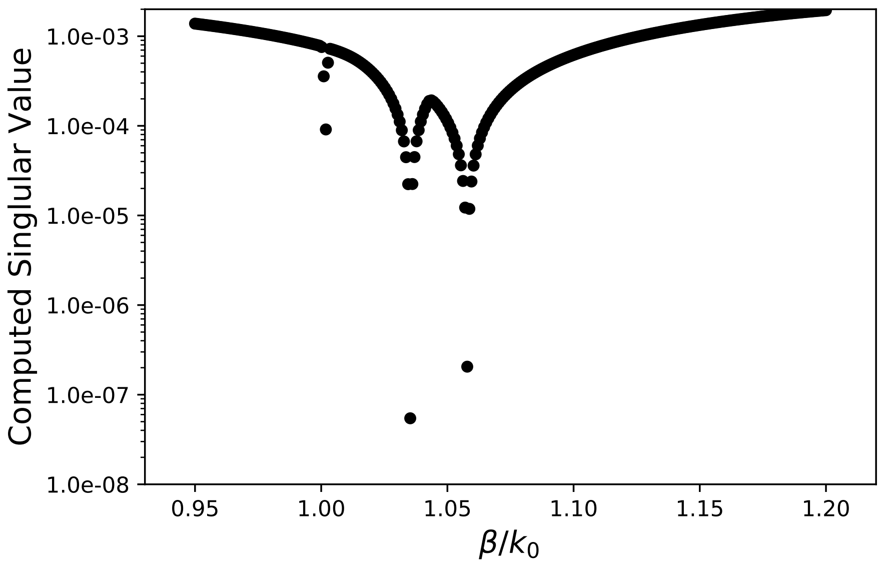

Figure 3.26 | **Singular value plot against** β/k_o

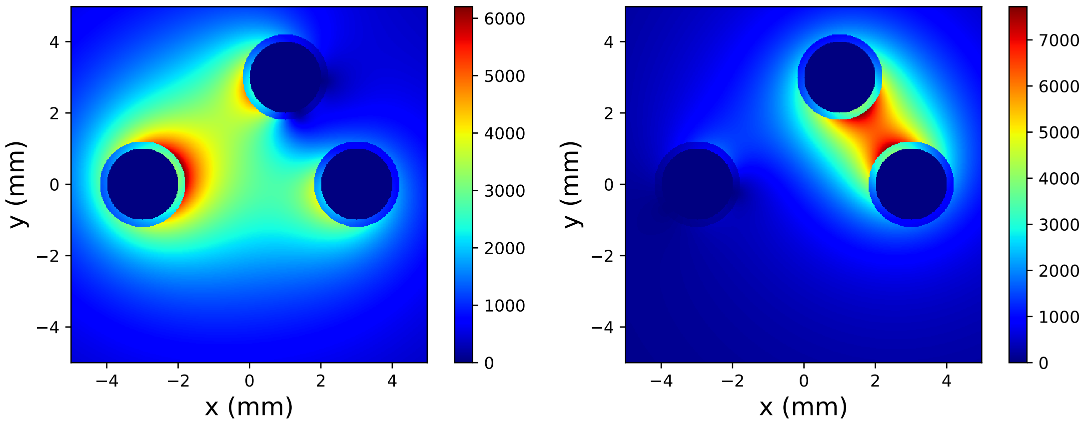

(a) Mode1

(b) Mode2

Figure 3.27 | Transverse Electric Field (E_t) distribution in the space

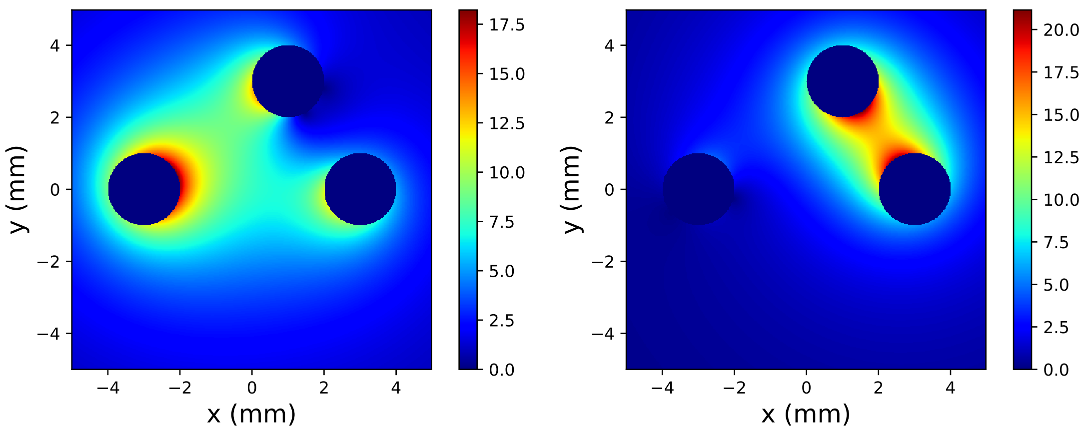

(a) Mode1

(b) Mode2

Figure 3.28 | Transverse Magnetic Field (H_t) distribution in the space

3.5 Conclusion

This chapter presents the analysis of wave propagation and local field solutions in multi-core wire systems in the cross-sectional plane. A numerical method is used to find appropriate propagation constants of waves in the presence of multiple wires with and without dielectric coatings. It is found that when the medium is homogeneous, the longitudinal propagation constant β is same as the total wave number k_0. This is referred to the Transverse Electromagnetic (TEM) mode of propagation. When more than two conductors presented, different modes of transverse field distribution is based on same value of β.

In the situation of inhomogeneous surrounding medium, β is found slightly shift from k_0. This shift is usually small and the wave propagating in such system follows quasi-TEM mode. When more than two conductors presented in the space, different values of β that correspond to different modes of field solutions for transverse field components are explicitly defined.

References

[3.1] Y. K. Choong, P. Sewell, and C. Christopoulos, "Hybrid node for description of thin wires based on analytical field representation in EMC problems," 2002 Ieee International Symposium on Electromagnetic Compatibility, Vols 1 and 2, Symposium Record pp. 840–844 (2002).

[3.2] Y. K. Choong, P. Sewell, and C. Christopoulos, "New thin wire formulation for time-domain differential-equation models," International Journal of Numerical Modelling-Electronic Networks Devices and Fields **15**, 489–501 (2002).

[3.3] Y. Choong, P. Sewell, and C. Christopoulos, "Accurate modelling of an arbitrary placed thin wire in a coarse mesh," IEE Proceedings - Science, Measurement and Technology **149**, 250–253(3) (2002).

[3.4] P. Sewell, Y. K. Choong, and C. Christopoulos, "An accurate thin-wire model for 3-D TLM simulations," Electromagnetic Compatibility, IEEE Transactions on **45**, 207–217 (2003).

[3.5] Y. Liu, P. Sewell, K. Biwojno, and C. Christopoulos, "A generalized node for embedding subwavelength objects into 3-D transmission-line models," IEEE Transactions on Electromagnetic Compatibility **47**, 749–755 (2005).

[3.6] S. Ramo, J. R. Whinnery, and T. Van Duzer, *Fields and waves in communication electronics* (John Wiley & Sons, 2008).

[3.7] S. J Orfanidis, *Electromagnetic Waves and Antennas* (2014).

4

Transmission Line Modelling (TLM) Method

This chapter introduces the working principles of the time-domain numerical modelling method, the Transmission Line Modelling (TLM) method. The TLM method and its derivative, the UTLM method is of important role in current Electromagnetic Compatibility (EMC) simulation. It is necessary to understand the operation principle before developing suitable thin-wire models to be embedded into the network. A more systematic description of the theory can be found in [4.1,4.2]. In addition the theory of two-dimensional unstructured TLM (UTLM) is introduced based on [4.2–4.4].

***

4.1 Introduction to TLM

The history and background of the Transmission Line Modelling method have been introduced in chapter (1). This chapter introduces fundamental theories of TLM from One-dimensional space to Three-dimensional space, and further more, presents theories of UTLM in unstructured meshing environment.

It is worth briefly discussing the analogy between transmission line network and electromagnetic fields before introducing detailed theory of TLM. A simple one-dimensional transmission line circuit is shown in Fig.4.1. The time dependent voltage v and current i along horizontal propagation direction in a transmission line network follows Kirchhoff's voltage (KVL) and current (KCL) laws [4.1]:

$$-\frac{\partial v}{\partial x}\Delta x = L\frac{\partial i}{\partial t}, \tag{4.1}$$

$$-\frac{\partial i}{\partial x}\Delta x = C\frac{\partial v}{\partial t} + \frac{v}{R}, \tag{4.2}$$

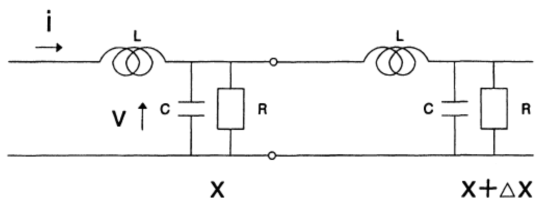

Figure 4.1 | Transmission Line Network

Equations (4.1) and (4.2) can then be manipulated to one variable form:

$$\frac{\partial^2 i}{\partial x^2} = \frac{LC}{(\Delta x)^2}\frac{\partial^2 i}{\partial t^2} + \frac{L}{(\Delta x)^2 R}\frac{\partial i}{\partial t} \tag{4.3}$$

Similar equation form can be found in one-dimensional electromagnetic field problem, for example the current density j in a lossy medium:

$$\frac{\partial^2 j}{\partial x^2} = \mu\varepsilon \frac{\partial^2 j}{\partial t^2} + \mu\sigma \frac{\partial j}{\partial t} \tag{4.4}$$

Where μ, ε and σ represent the magnetic permeability, electric permittivity and electrical conductivity of the medium respectively. Similar results can also be found for field components in three-dimensional models. This implies the similarity of laws governing circuit behaviour and field behaviour. Therefore electromagnetic field problems can be understood by studying proper models of transmission line circuits.

4.2 One-Dimensional TLM

A one-dimensional TLM network can be treated as a cascade of transmission line segments where voltage and current only vary in one coordinate. A simple lossy electric circuit segment can be seen in Fig.4.2(a), where R, G, L and C are the per-segment length parameters that represent series resistance, shunt admittance, series inductance and shunt capacitance respectively. The model can be transferred to a transmission line equivalent with a characteristic impedance $Z_o = \sqrt{L/C}$ representing the series inductance and shunt capacitance as shown in Fig.4.2(b). A 1-D TLM network consists of several such segments with nodes connecting each

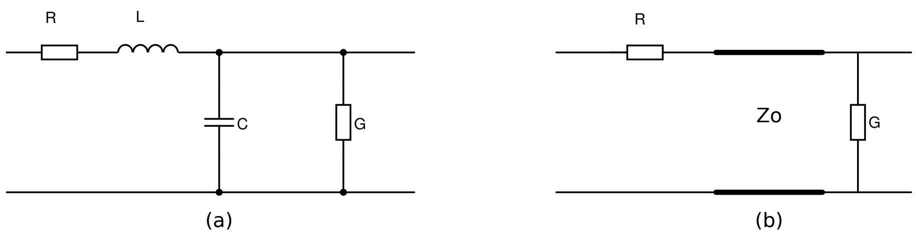

Figure 4.2 | (a)Basic electric circuit segment, (b)its transmission line model

other, as depicted in Fig. 4.3. ${}_kVL_n^i$, ${}_kVL_n^r$, ${}_kVR_n^i$, ${}_kVR_n^r$ are voltage pulses incident to and reflected from node n at time-step k, where i stands for incident pulses and r represents reflected pulses. In this example it is assumed that the space-step Δx for each segment is same through the problem for simplicity. It is also assumed that parameters for each segment are same, therefore the transit time for each segment $\Delta t = \sqrt{LC}$ is same. The Thevenin equivalent circuit in Fig. 4.4 shows the condition

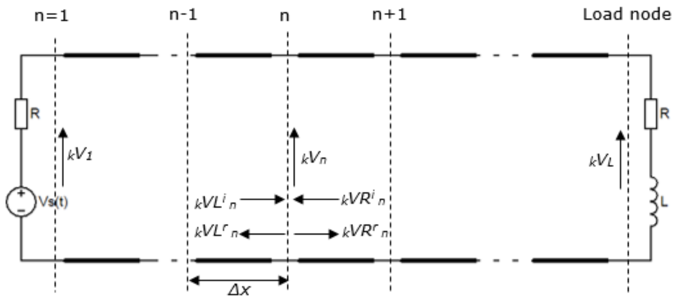

Figure 4.3 | **One-dimensional TLM model**

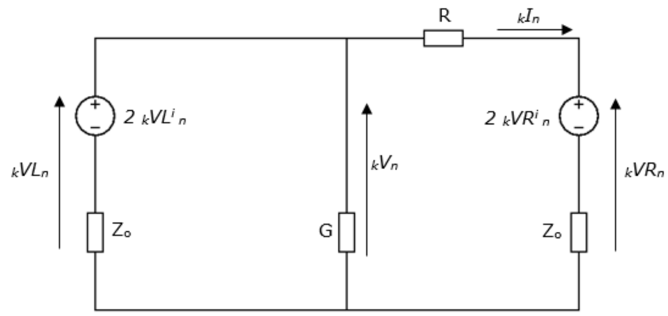

Figure 4.4 | Thevenin equivalent circuit for an arbitrary node in TLM model

for node n connecting two sections at times-step k. It can be seen clearly that the total voltage at node n at time-step k is a result of voltage pulses incident from left and right sections. According to Millman's Theorem [4.1]:

$$_kV_n = \frac{\frac{2_kVL^i}{Z_o} + \frac{2_kVR^i}{Z_o+R}}{\frac{1}{Z_o} + \frac{1}{Z_o+R} + G} \tag{4.5}$$

Therefore the current at the node as well as the total voltage on the left of the node and on the right are obtained through equations:

$$_kI_n = \frac{_kV_n - 2_kVR_n^i}{R + Z_o} \tag{4.6}$$

$$_kVL_n = \ _kV_n \tag{4.7}$$

$$_kVR_n = \ 2_kVR_n^i + {_kI_n}Z_o \tag{4.8}$$

The total voltages on the left and right of the node is the sum of incident voltages to the node and reflected voltages from the node. Therefore voltage pulses reflected into line segments on both sides of the node are:

$$_kVL_n^r = \ _kVL_n - {_kVL_n^i} \tag{4.9}$$

$$_kVR_n^r = \ _kVR_n - {_kVR_n^i} \tag{4.10}$$

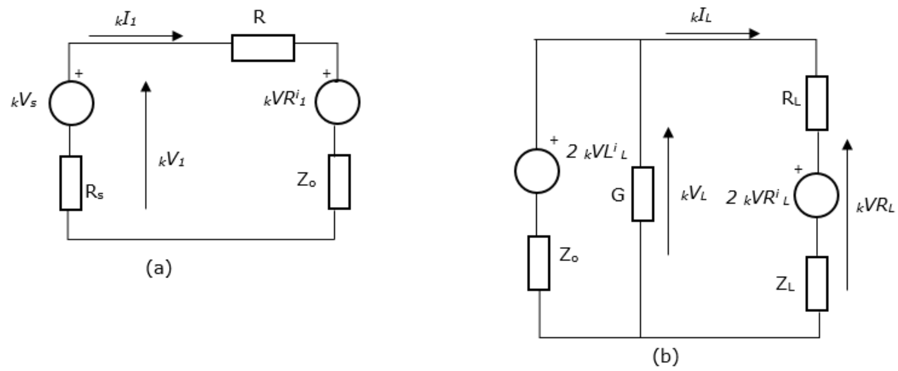

Figure 4.5 | Thevenin equivalent circuit for (a) source node, (b) load node in TLM model

The new incident voltage at time-step *k+1* to the node is the same value of reflected voltage from adjacent nodes at time-step k:

$$_{k+1}VL_n^i = \ _kVR_{n-1}^r \tag{4.11}$$

$$_{k+1}VR_n^i = \ _kVL_{n+1}^r \tag{4.12}$$

Equations above need to be modified for the first node and last node, because they connect to source and load. For the source node, the Thevenin equivalent circuit is shown in Fig.4.5(a). Therefore the total voltage at first node is a result of source voltage and incident voltage from right side of first node:

$$_kV_1 = \frac{\frac{V_s}{R_s} + \frac{2\,_kVR_1^i}{R+Z_o}}{\frac{1}{Rs} + \frac{1}{R+Z_o}} \tag{4.13}$$

Therefore other pulses can be got as:

$$_kI_1 = \frac{_kV_1 - 2\,_kVR_1^i}{R + Z_o} \tag{4.14}$$

$$_kVR_1 = 2\,_kVR_1^i + \ _kI_1\ Z_o \tag{4.15}$$

$$_kVR_1^r = \ _kVR_1 - \ _kVR_1^i \tag{4.16}$$

$$\tag{4.17}$$

And the incident voltage from right side of node *1* at time-step *k+1* is same as the reflected voltage from node *2* at time-step k:

$$ {}_{k+1}VR_1^i = {}_kVL_2^r \tag{4.18} $$

For the load node, the Thevenin equivalent circuit is shown in Fig.4.5(b). The load inductance is replaced by a load impedance $Z_L = 2L_o/\Delta t$ where Δt is the round trip transit time at the load. The total voltage across load is therefore:

$$ {}_kV_L = \frac{\frac{2\,{}_kVL_L^i}{Z_o} + \frac{2\,{}_kVR_L^i}{R_L+Z_L}}{\frac{1}{Z_o} + \frac{1}{R_Z+Z_L} + G} \tag{4.19} $$

Therefore the load current and other voltages are:

$$ {}_kI_L = \frac{{}_kV_L - 2\,{}_kVR_L^i}{R_L + Z_L} \tag{4.20} $$

$$ {}_kVR_L = 2\,{}_kVR_L^i + {}_kI_L\ Z_L \tag{4.21} $$

$$ {}_kVR_L^r = {}_kVR_L - {}_kVR_L^i \tag{4.22} $$

$$ {}_{k+1}VR_L^i = -\,{}_kVR_L^r \tag{4.23} $$

$$ {}_kVL_L^r = {}_kV_L - {}_kVL_L^i \tag{4.24} $$

4.3 Two-Dimensional TLM

The 2D TLM is understood by analogy to Huygens theorem [4.1], which states that the wave of a point on a wavefront propagates as an isotropic spherical radiator. Therefore the new wavefront is created by the superposition of waves from all the points on the previous wave, just like a little stone dropping to the surface of a calm lake and causing the propagation of ripples.

There are basically two configurations in 2D TLM models representing the transverse electric(TE) modes that contain H_z components only and the transverse magnetic(TM) modes that contain E_z components only, named as "series" and "shunt" nodes respectively. The details of these two models will be discussed in following sections.

4.3.1 Series TLM node

The series node models transverse electric (TE) mode fields in a 2D TLM problem, hence only E_x, E_y, and H_z components exist in the model. Maxwell's equations therefore become:

$$\frac{\partial H_z}{\partial y} = \varepsilon \frac{\partial E_x}{\partial t} \tag{4.25}$$

$$-\frac{\partial H_z}{\partial x} = \varepsilon \frac{\partial E_y}{\partial t} \tag{4.26}$$

$$\frac{\partial E_y}{\partial x} - \frac{\partial E_x}{\partial y} = -\mu \frac{\partial H_x}{\partial t} \tag{4.27}$$

These equations can be manipulated to the wave equation with H_z components only:

$$\frac{\partial^2 H_z}{\partial x^2} + \frac{\partial^2 H_z}{\partial y^2} = \mu\varepsilon \frac{\partial^2 H_z}{\partial t^2} \tag{4.28}$$

The structure of a series node can be modelled by four transmission line segments with same characteristic impedance Z_{TL} connected in series, as shown in Fig. 4.6.

The meshing cell is assumed to be square, with both Δx and Δy equal to Δl.

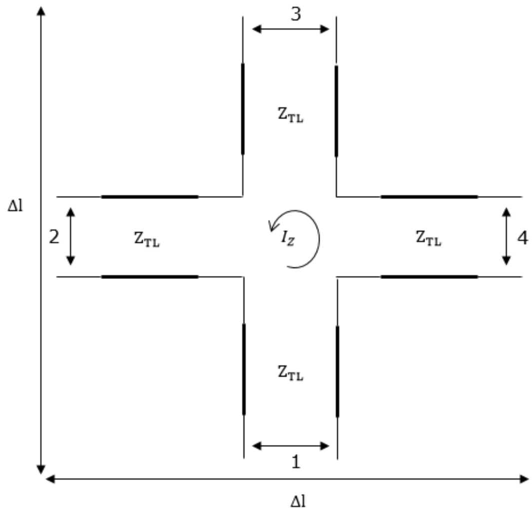

Figure 4.6 | Structure of the series node for 2D-TLM model

The Thevenin Equivalent circuit of the series node at time-step k can be obtained by replacing the transmission line segments by its Thevenin equivalent, which contains a voltage source 2_kV^i and an impedance Z_{TL}, as shown in Fig. 4.7.

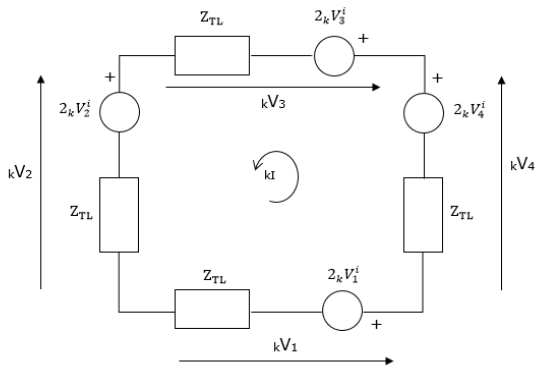

Figure 4.7 | Thevenin equivalent circuit of the series node

From Fig. 4.7, the current in the circuit can be obtained by:

$$ {}_kI = \frac{2\,{}_kV_1^i + 2\,{}_kV_4^i - 2\,{}_kV_2^i - 2\,{}_kV_3^i}{4Z_{TL}} \tag{4.29}$$

The electric and magnetic field components can be obtained from the voltages and current:

$$_kE_x = -\frac{_kV_1^i + {_kV_3^i}}{\Delta l} \tag{4.30}$$

$$_kE_y = -\frac{_kV_2^i + {_kV_4^i}}{\Delta l} \tag{4.31}$$

$$_kH_z = \frac{2\,{_kV_1^i} + 2\,{_kV_4^i} - 2\,{_kV_2^i} - 2\,{_kV_3^i}}{4\Delta l Z_{TL}} \tag{4.32}$$

Similar to the last section for 1D TLM, the reflected voltages can be obtained by subtracting the incident voltage from the total voltage on the port:

$$_kV_n^r = {_kV_n} - {_kV_n^i} = 2\,{_kV_n^i} - {_kIZ_{TL}} - {_kV_n^i} = {_kV_n^i} - {_kIZ_{TL}} \tag{4.33}$$

Therefore the reflected voltages on at all ports of one node can be expressed as an incident voltage vector $_{\boldsymbol{k}}\boldsymbol{V^i}$ times a scattering matrix $\boldsymbol{S}$:

$$_{\boldsymbol{k}}\boldsymbol{V^r} = \boldsymbol{S}\,{_{\boldsymbol{k}}\boldsymbol{V^i}} \tag{4.34}$$

where

$$_{\boldsymbol{k}}\boldsymbol{V^r} = [\,{_kV_1^r} \quad {_kV_2^r} \quad {_kV_3^r} \quad {_kV_4^r}]^T \tag{4.35}$$

$$_{\boldsymbol{k}}\boldsymbol{V^i} = [\,{_kV_1^i} \quad {_kV_2^i} \quad {_kV_3^i} \quad {_kV_4^i}]^T \tag{4.36}$$

$$\boldsymbol{S} = 0.5\begin{bmatrix} 1 & 1 & 1 & -1 \\ 1 & 1 & -1 & 1 \\ 1 & -1 & 1 & 1 \\ -1 & 1 & 1 & 1 \end{bmatrix} \tag{4.37}$$

The incident voltages on the ports for next time-step are obtained by the reflected voltages from adjacent nodes, same as in the 1D TLM model.

4.3.2 Shunt TLM Node

The modelling procedure for shunt TLM node is similar to for series node, with TE modes field becoming TM modes (H_x, H_y and E_z). This results in the Maxwell's equations reduced to:

$$\frac{\partial E_z}{\partial y} = -\mu \frac{\partial H_x}{\partial t} \tag{4.38}$$

$$-\frac{\partial E_z}{\partial x} = -\mu \frac{\partial H_y}{\partial t} \tag{4.39}$$

$$\frac{\partial H_y}{\partial x} - \frac{\partial H_x}{\partial y} = \varepsilon \frac{\partial E_z}{\partial t} \tag{4.40}$$

The wave equation for TM modes propagation can therefore be obtained by manipulating these equations as:

$$\frac{\partial^2 E_z}{\partial x^2} + \frac{\partial^2 E_z}{\partial y^2} = \mu\varepsilon \frac{\partial^2 E_z}{\partial t^2} \tag{4.41}$$

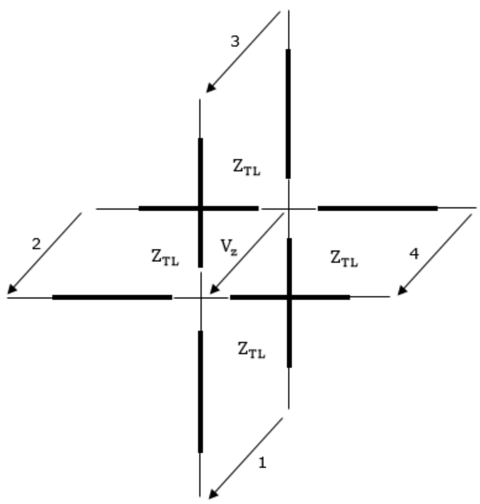

Figure 4.8 | Structure of the shunt node for 2D-TLM model

The Thevenin equivalent circuit for the shunt node is shown in Fig. 4.9.

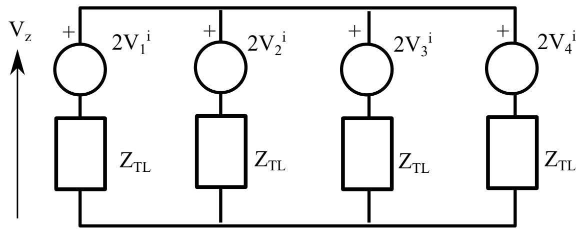

Figure 4.9 | Thevenin equivalent circuit of the shunt node in for 2-D TLM

From Fig. the voltage at the node is given by:

$$V_z = 0.5(V_1^i + V_2^i + V_3^i + V_4^i) \tag{4.42}$$

And the current components are:

$$I_x = \frac{V_2^i - V_4^i}{Z_{TL}} \tag{4.43}$$

$$I_y = \frac{V_1^i - V_3^i}{Z_{TL}} \tag{4.44}$$

The field components are therefore obtained from the equivalence between field and circuit:

$$E_z = -0.5\frac{V_1^i + V_2^i + V_3^i + V_4^i}{\Delta z} \tag{4.45}$$

$$H_y = \frac{V_2^i - V_4^i}{Z_{TL}\Delta y} \tag{4.46}$$

$$H_x = \frac{V_3^i - V_1^i}{Z_{TL}\Delta x} \tag{4.47}$$

The reflected voltages can be obtained by subtracting the incident voltages on the port from the total voltage V_z:

$$_kV_n^r = V_z - \ _kV_n^i \tag{4.48}$$

Therefore the scattering matrix **S** becomes:

$$\boldsymbol{S} = 0.5 \begin{bmatrix} -1 & 1 & 1 & 1 \\ 1 & -1 & 1 & 1 \\ 1 & 1 & -1 & 1 \\ 1 & 1 & 1 & -1 \end{bmatrix}$$

The connection process for next time-step operates same as for the 1-D TLM.

4.4 Three-Dimensional TLM

The three-dimensional TLM is based upon the symmetrical condensed node(SCN) [4.1,4.2,4.5]. The structure of a SCN model is shown in Fig. 4.10. The 3-D node consists of six faces, each containing two ports that correspond to two set of incident voltages of orthogonal polarisations respectively.

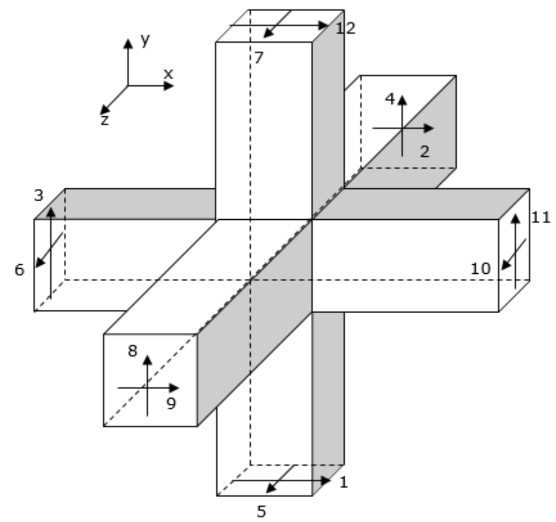

Figure 4.10 | Structure of the 3D Symmetrical Condensed Node (SCN) model

The scattering matrix that relates the reflected voltage to incident voltage ${}_k\mathbf{V^r} = \mathbf{S}\,{}_\mathbf{k}\mathbf{V^i}$ now becomes:

$$\boldsymbol{S} = 0.5 \begin{bmatrix} 0 & 1 & 1 & 0 & 0 & 0 & 0 & 0 & 1 & 0 & -1 & 0 \\ 1 & 0 & 0 & 0 & 0 & 1 & 0 & 0 & 0 & -1 & 0 & 1 \\ 1 & 0 & 0 & 1 & 0 & 0 & 0 & 1 & 0 & 0 & 0 & -1 \\ 0 & 0 & 1 & 0 & 1 & 0 & -1 & 0 & 0 & 0 & 1 & 0 \\ 0 & 0 & 0 & 1 & 0 & 1 & 0 & -1 & 0 & 1 & 0 & 0 \\ 0 & 1 & 0 & 0 & 1 & 0 & 1 & 0 & -1 & 0 & 0 & 0 \\ 0 & 0 & 0 & -1 & 0 & 1 & 0 & 1 & 0 & 1 & 0 & 0 \\ 0 & 0 & 1 & 0 & -1 & 0 & 1 & 0 & 0 & 0 & 1 & 0 \\ 1 & 0 & 0 & 0 & 0 & -1 & 0 & 0 & 0 & 1 & 0 & 1 \\ 0 & -1 & 0 & 0 & 1 & 0 & 1 & 0 & 1 & 0 & 0 & 0 \\ -1 & 0 & 0 & 1 & 0 & 0 & 0 & 1 & 0 & 0 & 0 & 1 \\ 0 & 1 & -1 & 0 & 0 & 0 & 0 & 0 & 1 & 0 & 1 & 0 \end{bmatrix}$$

The connection process is processed by directing reflected voltages toward adjacent port of the adjacent node as the incident voltage for the next time step.

4.5 Two-Dimensional Unstructured TLM

The demand for unstructured meshes in TLM simulation arises dramatically when describing curved boundaries and material interfaces due to the apparent staircase phenomenon caused by using Cartesian meshing [4.3]. The meshing method is based upon the triangular mesh used regularly in the finite-element method (FEM) with the requirement of satisfying Delaunay criteria [4.6]. The theory of two-dimensional (2D) unstructured TLM (UTLM) is based on local field solutions of wave equations.

An arbitrary 2D UTLM node consisting of three ports is shown in Fig. 4.3. The ports connect to adjacent nodes with a distance Δ_i between two node centres. ϕ_i denotes the angle between two ports. By inspection the fields around the node can be described by a set of cylindrical harmonics, which are solutions of the 2D wave-equation, centred on the node centre. For the triangular mesh of sufficiently small size, it is suggested that first three order harmonics are accurate to represent the solution [4.3]:

$$E_z = J_0(kr)X_{c0} + cos(\theta)J_1(kr)\frac{2X_{c1}}{k} + sin(\theta)J_1(kr)\frac{2X_{s1}}{k} \tag{4.49}$$

$$-j\omega\mu_o H_\theta = \frac{\partial E_z}{\partial r} \tag{4.50}$$

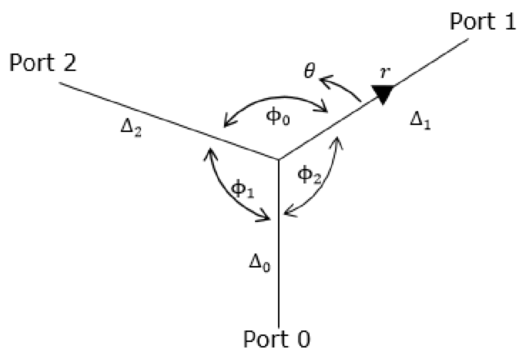

Figure 4.11 | 2D UTLM node structure

Where k is the wave number in the medium and $k = 2\pi/\lambda$ where λ is the wavelength in the medium. Xs are the coefficients of the three terms that sample the tangential fields at the ports. The E_z and H_θ fields can therefore be expressed in matrix form with respect to the nodal ports:

$$\underline{E} = \underline{\underline{T}}_e \, \underline{X} \tag{4.51}$$

$$j\omega\mu_0 \Delta^D \underline{H}_\theta = \underline{\underline{T}}_h \, \underline{X} \tag{4.52}$$

Where $\Delta^D = diag\{\Delta_1 \quad \Delta_2 \quad \Delta_0\}$. When the node size is considerably small, typically less than one tenth of the wavelength, the small argument approximation of the Bessel function can be applied [4.3]:

$$J_0(kr)|_{kr<<1} = 1 \tag{4.53}$$

$$J_1(kr)|_{kr<<1} = \frac{kr}{2} \tag{4.54}$$

$$\frac{\partial J_0(kr)}{\partial r}|_{kr<<1} = \frac{k^2 r}{2} \tag{4.55}$$

$$\frac{\partial J_1(kr)}{\partial r}|_{kr<<1} = \frac{k}{2} \tag{4.56}$$

Therefore $\underline{\underline{T}}_e and \underline{\underline{\mathrm{T}}}$`h in equations (4.51) and (4.52) can be expressed as:

$$\underline{\underline{T}}_e = \begin{bmatrix} 1 & \Delta_1 & 0 \\ 1 & \Delta_2 cos(\phi_0) & \Delta_2 sin(\phi_0) \\ 1 & \Delta_0 cos(\phi_0 + \phi_1) & \Delta_0 sin(\phi_0 + \phi_1) \end{bmatrix} \tag{4.57}$$

$$\underline{\underline{T}}_h = \begin{bmatrix} -k^2\Delta_1^2/2 & \Delta_1 & 0 \\ -k^2\Delta_2^2/2 & \Delta_2 cos(\phi_0) & \Delta_2 sin(\phi_0) \\ -k^2\Delta_0^2/2 & \Delta_0 cos(\phi_0 + \phi_1) & \Delta_0 sin(\phi_0 + \phi_1) \end{bmatrix} \tag{4.58}$$

The expressions for E_z and H_ϕ indicates an admittance relationship between them in the matrix form:

$$j\omega\mu_o\Delta^D \begin{bmatrix} H_{\theta 1} \\ H_{\theta 2} \\ H_{\theta 0} \end{bmatrix} = \underline{\underline{T}}_h \underline{\underline{T}}_e^- 1 \begin{bmatrix} E_{z1} \\ E_{z2} \\ E_{z0} \end{bmatrix} \tag{4.59}$$

A detailed expression of equation (4.59) can be derived by substituting the inversion of equation (4.57) and (4.58) [4.2,4.3]:

$$\begin{bmatrix} H_{\theta 1} \\ H_{\theta 2} \\ H_{\theta 0} \end{bmatrix} = \frac{j\omega\varepsilon_o}{2} \frac{\begin{bmatrix} \Delta_2\Delta_0\Delta_1 s_1 & \Delta_0\Delta_1\Delta_1 s_2 & \Delta_2\Delta_1\Delta_1 s_0 \\ \Delta_2\Delta_0\Delta_2 s_1 & \Delta_0\Delta_1\Delta_2 s_2 & \Delta_2\Delta_1\Delta_2 s_0 \\ \Delta_2\Delta_0\Delta_0 s_1 & \Delta_0\Delta_1\Delta_0 s_2 & \Delta_2\Delta_1\Delta_0 s_0 \end{bmatrix}}{\Delta_2\Delta_0 s_1 + \Delta_1\Delta_0 s_2 + \Delta_2\Delta_1 s_0} \begin{bmatrix} E_{z1} \\ E_{z2} \\ E_{z0} \end{bmatrix} + \frac{1}{j\omega\mu_o} \frac{\begin{bmatrix} \Delta_0 s_2 + \Delta_2 s_0 & -\Delta_0 s_2 & -\Delta_2 s_0 \\ -\Delta_0 s_1 & \Delta_0 s_1 + \Delta_1 s_0 & -\Delta_1 s_0 \\ -\Delta_2 s_1 & -\Delta_1 s_2 & \Delta_1 s_2 + \Delta_2 s_1 \end{bmatrix}}{\Delta_2\Delta_0 s_1 + \Delta_1\Delta_0 s_2 + \Delta_2\Delta_1 s_0} \begin{bmatrix} E_{z1} \\ E_{z2} \\ E_{z0} \end{bmatrix} \tag{4.60}$$

Where s_i is short for $sin(\phi_i)$. The port voltages are related to the electric field while the currents are related to the magnetic field scaled by as yet arbitrary factor αs_i for each port:

$$\begin{bmatrix} E_{z1} \\ E_{z2} \\ E_{z0} \end{bmatrix} = \begin{bmatrix} V_1 \\ V_2 \\ V_0 \end{bmatrix} \qquad \begin{bmatrix} \alpha s_1 & 0 & 0 \\ 0 & \alpha s_2 & 0 \\ 0 & 0 & \alpha s_0 \end{bmatrix} \begin{bmatrix} H_{\theta_1} \\ H_{\theta_2} \\ H_{\theta_0} \end{bmatrix} = \begin{bmatrix} I_1 \\ I_2 \\ I_0 \end{bmatrix} \tag{4.61}$$

Therefore the admittance relationship between voltages and currents can be directly obtained:

$$\underline{I} = \frac{j\omega\varepsilon_o\alpha}{2}\frac{\begin{bmatrix}\Delta_2\Delta_0\Delta_1 s_1 s_1 & \Delta_0\Delta_1\Delta_1 s_2 s_1 & \Delta_2\Delta_1\Delta_1 s_0 s_1\\ \Delta_2\Delta_0\Delta_2 s_1 s_2 & \Delta_0\Delta_1\Delta_2 s_2 s_2 & \Delta_2\Delta_1\Delta_2 s_0 s_2\\ \Delta_2\Delta_0\Delta_0 s_1 s_0 & \Delta_0\Delta_1\Delta_0 s_2 s_0 & \Delta_2\Delta_1\Delta_0 s_0 s_0\end{bmatrix}}{\Delta_2\Delta_0 s_1 + \Delta_1\Delta_0 s_2 + \Delta_2\Delta_1 s_0}\underline{V} + \frac{\alpha}{j\omega\mu_o}\frac{\begin{bmatrix}\Delta_0 s_2 s_1 + \Delta_2 s_0 s_1 & -\Delta_0 s_2 s_1 & -\Delta_2 s_0 s_1\\ -\Delta_0 s_1 s_2 & \Delta_0 s_2 s_1 + \Delta_1 s_0 s_2 & -\Delta_1 s_0 s_2\\ -\Delta_2 s_1 s_2 & -\Delta_1 s_2 s_0 & \Delta_1 s_2 s_0 + \Delta_2 s_1 s_0\end{bmatrix}}{\Delta_2\Delta_0 s_1 + \Delta_1\Delta_0 s_2 + \Delta_2\Delta_1 s_0}\underline{V} \tag{4.62}$$

It can be inspected that the first term in (4.62) contributes to the capacitive part of the admittance and the second to the inductive part. By assuming low frequency the first matrix in equation (4.62) can be simplified to a diagonal matrix form:

$$\begin{bmatrix}\Delta_1 s_1 & 0 & 0\\ 0 & \Delta_2 s_2 & 0\\ 0 & 0 & \Delta_0 s_0\end{bmatrix} \tag{4.63}$$

Consequently both capacitive and inductive terms of the admittance are reciprocal hence the electrical circuit is able to generate. Fig. 4.12 shows the equivalent circuit of a UTLM shut node model relating the port voltages and currents as well as its TLM model. The inductive stubs provide complete link-line impedance needed for the circuit while the open-circuit capacitive stubs ensure the synchronization of pulse propagation in the whole mesh space. The inductor and capacitor values for each port are obtained from:

$$L_i = \frac{\mu_o\Delta_i}{\alpha s_i} \tag{4.64}$$

$$C_i = \frac{\alpha\varepsilon_o s_i\Delta_i}{2} \tag{4.65}$$

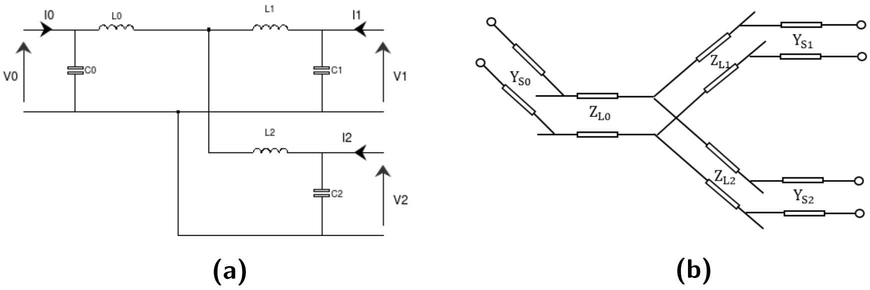

Figure 4.12 | (a)The equivalent circuit of a 2D UTLM mesh and (b) transmission line circuit

The transmission line component values in (4.64) and (4.65) has not yet been explicitly defined, due to the arbitrary choice of the node centre. Although the voltages and currents at the port between two nodes are already continuous due to its nature and the continuity of the voltages implies the continuity of the electric fields from (4.61), the continuity of the currents does not guarantee that the magnetic field to be continuous automatically due to the undefined scalar factor αs_i.

This can be achieved by choosing appropriate value of α and the node centre. In this case the node centre is chosen as the circumcentre of the triangle. From triangle characteristics the edge length l_i opposite the angle ϕ_i can be obtained by $l_i = 2R\ sin_{\phi_i}$ where R is the circumradius. Therefore the value of α can be chosen as $2R$ for each node so that $\alpha s_i = l_i$ hence $I_i = l_i H_i$. As a result the continuity of the currents between adjacent nodes that share the same side l_i ensures the continuity of the magnetic fields.

The admittance of the link line and the stub line in Fig. 4.12 (b) are obtained in time domain by:

$$Y_{link_i} = \frac{l_a \Delta t}{2\mu\Delta_i} \tag{4.66}$$

$$Y_{stub_i} = \frac{\varepsilon l_i \Delta_i}{\Delta_t} - \frac{l_i \Delta_t}{2\mu\Delta_i} \tag{4.67}$$

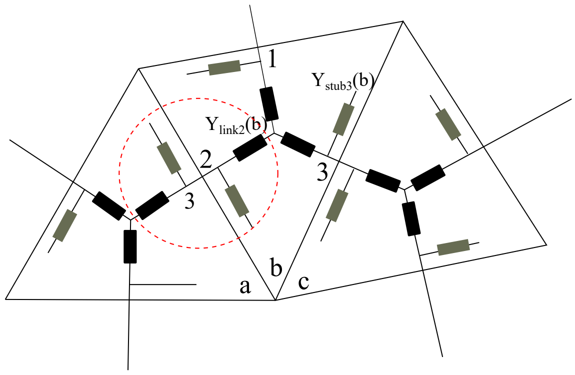

Figure 4.13 | 2-D UTLM network of 3 nodes

where Δ_t refers to the time step and is constrained by the minimum link length in the mesh.

Fig. 4.13 shows the network of three 2-D UTLM nodes connected together. The reflected voltages at time step k of node b are calculated separately for the link line and the stub line:

$$ {}_kV^r_{link_n} = {}_kV_b - {}_kV^i_{link_n} \tag{4.68}$$

$$ {}_kV^r_{stub_n} = {}_kV^i_{stub_n} \tag{4.69}$$

where

$$ {}_kV_b = \frac{2\sum_{n=1}^{3} {}_kV^i_{link_n} Y_{link_n}}{\sum_{n=1}^{3} Y_{link_n}} $$

The total voltage at the connection between node a port 3 and node b port 2 is:

$$ {}_kV_{a,b} = \frac{2\left[{}_kV^r_{link_3}(a)Y_{link_3}(a) + {}_kV^r_{stub_3}(a)Y_{stub_3}(a) + {}_kV^r_{link_2}(b)Y_{link_2}(b) + {}_kV^r_{stub_2}(b)Y_{stub_2}(b)\right]}{Y_{link_3}(a) + Y_{stub_3}(a) + Y_{link_2}(b) + Y_{stub_2}(b)} \tag{4.70}$$

Therefore the incident voltages for the next time steps are:

$$ {}_{k+1}V^i_{link_3}(a) = {}_kV_{a,b} - {}_kV^r_{link_2}(b) \tag{4.71}$$

$$ {}_{k+1}V^i_{stub_3}(a) = {}_kV_{a,b} - {}_kV^r_{stub_2}(b) \tag{4.72}$$

4.6 Three-Dimensional UTLM

This section extends the theory of two-dimenstional UTLM to three dimensions. Tetrahedral meshes are used to discretise the simulation space. Fig. 4.14 shows an arbitrary tetrahedral mesh as a UTLM node with four port notation. The distance from the node centre to the ith port surface is denoted as Δ_i and the unit directional vector is denoted as $\hat{n}$. The node centre is defined as the circumcentre of a tetrahedral mesh, and the reason will be described subsequently.

The basic algorithm of this approach is to map the impedance relationship of sampled tangential electric and magnetic fields at the ports to an analogous voltage and current relationship in a passive electrical circuit model. This analogue only holds when the impedance relationship is reciprocal and the continuity of electric and magnetic field at the ports between adjacent nodes is guaranteed.

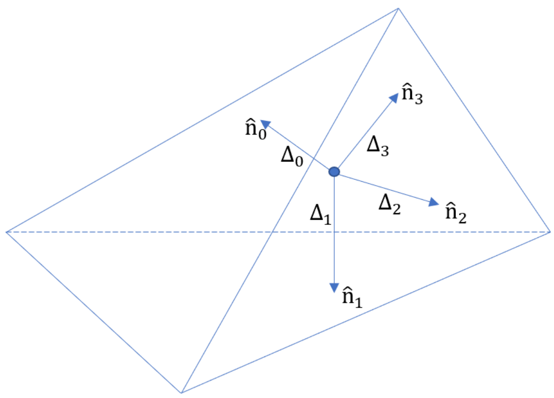

Figure 4.14 | Arbitrary four-port UTLM node

In order to develop such relationship, the local field solutions in the form of spherical harmonics centred upon the node is used to express the tangential electric and magnetic fields at ith port:

$$\boldsymbol{E}_i = (\boldsymbol{I} - \hat{\boldsymbol{n}}_i\hat{\boldsymbol{n}}_i) \cdot \sum_n \boldsymbol{e}_n X_n \tag{4.73}$$

$$\hat{\boldsymbol{n}}_i \times \boldsymbol{H}_i = (\boldsymbol{I} - \hat{\boldsymbol{n}}_i\hat{\boldsymbol{n}}_i) \cdot \sum_n \boldsymbol{h}_n X_n \tag{4.74}$$

where $\boldsymbol{e}_n$ and $\boldsymbol{h}_n$ are the nth term in the spherical expansions [4.4]. $\boldsymbol{I}$ is the identity dyadic and hence $\boldsymbol{I}-\hat{\boldsymbol{n}}_i\hat{\boldsymbol{n}}_i$ enforces tangential field components at the ith port.

In practical, the spherical harmonics in expression $\boldsymbol{e}_n$ and $\boldsymbol{h}_n$ can be truncated to eight independent terms that correspond to eight field components at four ports of the node and keep sufficient accuracy [4.4]. The three sets of first-order transverse magnetic (TM) fields with superscript (e) and transverse electric (TE) fields with superscript (h) at port i $(\Delta_i\hat{\boldsymbol{n}}_i)$ are expressed by:

$$\boldsymbol{e}_{mi}^{(e)} = 2\boldsymbol{u}_m \tag{4.75}$$

$$\boldsymbol{h}_{mi}^{(e)} = jY_0 k\Delta_i\boldsymbol{u}_m \tag{4.76}$$

$$\boldsymbol{e}_{mi}^{(h)} = -k\Delta_i\hat{\boldsymbol{n}}_i \times \boldsymbol{u}_m \tag{4.77}$$

$$\boldsymbol{h}_{mi}^{(h)} = 2jY_0\hat{\boldsymbol{n}}_i \times \boldsymbol{u}_m \tag{4.78}$$

where $\boldsymbol{u}_m$ being mth term independent vectors, k being the wave number at the specific frequency and Y_0 being the admittance.

The other two terms, chosen as a superposition of second-order expansion terms, with superscript (q) at ports i are expressed by:

$$\boldsymbol{e}_{mi}^{(q)} = -k^2\Delta_i^2\left(\hat{\boldsymbol{n}}_i \cdot \boldsymbol{u}_m\right)\hat{\boldsymbol{n}}_i \times \boldsymbol{u}_m \tag{4.79}$$

$$\boldsymbol{h}_{mi}^{(q)} = 2jY_0 k\Delta_i\left(\hat{\boldsymbol{n}}_i \cdot \boldsymbol{u}_m\right)\hat{\boldsymbol{n}}_i \times \boldsymbol{u}_m \tag{4.80}$$

These expressions above are sufficiently accurate if sets of $\boldsymbol{e}_m$ and $\boldsymbol{h}_n$ are orthogonal, as expressed below:

$$\begin{aligned}\left\langle \boldsymbol{e}_m^{(e)}, \boldsymbol{h}_n^h \right\rangle &= 4jY_0 \sum_{i=0}^{3} S_i \boldsymbol{u}_m \cdot (\boldsymbol{I} - \hat{\boldsymbol{n}}_i \hat{\boldsymbol{n}}_i) \cdot \hat{\boldsymbol{n}}_i \times \boldsymbol{u}_n \\ &= 4jY_0 \boldsymbol{u}_n \times \boldsymbol{u}_m \cdot \sum_{i=0}^{3} S_i \hat{\boldsymbol{n}}_i \\ &= 0\end{aligned} \tag{4.81}$$

$$\begin{aligned}\left\langle \boldsymbol{e}_m^{(e)}, \boldsymbol{h}_n^e \right\rangle &= 2jY_0 k \sum_{i=0}^{3} S_i \Delta_i \boldsymbol{u}_m \cdot (\boldsymbol{I} - \hat{\boldsymbol{n}}_i \hat{\boldsymbol{n}}_i) \cdot \boldsymbol{u}_n \\ &= 2jY_0 k \lambda_n \delta_{mn}\end{aligned} \tag{4.82}$$

$$\begin{aligned}\left\langle \boldsymbol{e}_m^{(e)}, \boldsymbol{h}_n^q \right\rangle &= 4jY_0 \sum_{i=0}^{3} S_i \boldsymbol{u}_m \cdot (\boldsymbol{I} - \hat{\boldsymbol{n}}_i \hat{\boldsymbol{n}}_i) \cdot \Delta_j \left(\hat{\boldsymbol{n}}_i \cdot \boldsymbol{u}_n\right) \hat{\boldsymbol{n}}_i \times \boldsymbol{u}_n \\ &= 4jY_0 k \cdot \sum_{i=0}^{3} S_i \hat{\boldsymbol{n}}_i \Delta_i \boldsymbol{u}_n \cdot \hat{\boldsymbol{n}}_j \boldsymbol{u}_n \times \boldsymbol{u}_m \\ &= 0\end{aligned} \tag{4.83}$$

These are true as the node centre is chosen as the circumcentre of the tetrahedral mesh, which makes $\sum_{i=0}^{3} S_i \hat{\boldsymbol{n}}_i = 0$ when S_i is the area of ith port surface. In addition, the vector terms $\boldsymbol{u}_n$ is chosen as eigensolutions of

$$\sum_{i=0}^{3} S_i \Delta_i \cdot (\boldsymbol{I} - \hat{\boldsymbol{n}}_i \hat{\boldsymbol{n}}_i) \cdot \boldsymbol{u}_n = \lambda_n Z_0 \sum Y_i \left(\boldsymbol{I} - \hat{\boldsymbol{n}}_i \hat{\boldsymbol{n}}_i\right) \cdot \boldsymbol{u}_n \tag{4.84}$$

Combining equations (4.75 - 4.80) gives the reciprocal impedance relationship:

$$\begin{aligned}\boldsymbol{E}_i = \sum_{j=0}^{3} \Bigg(\frac{j\omega\mu\Delta_i}{2S_i} \delta_{ij} + \sum_{m=0}^{2} \left(\frac{2}{j\omega\varepsilon} - \frac{j\omega\mu\Delta_i^2}{2} \right) (\boldsymbol{I} - \hat{\boldsymbol{n}}_i \hat{\boldsymbol{n}}_i) \\ \cdot \boldsymbol{u}_m \lambda_m^{-1} \boldsymbol{u}_m \cdot (\boldsymbol{I} - \hat{\boldsymbol{n}}_j \hat{\boldsymbol{n}}_j) \Bigg) \cdot (S_j \hat{\boldsymbol{n}}_j \times \boldsymbol{H}_j)\end{aligned} \tag{4.85}$$

An equivalent relationship between voltage and current can therefore be derived:

$$\boldsymbol{V}_i \;=\; \sum_{j=0}^{3}\left(\frac{j\omega\mu\Delta_i}{2S_i}\delta_{ij} \;+\; \sum_{m=0}^{2}(\boldsymbol{I} \;-\; \hat{\boldsymbol{n}}_i\hat{\boldsymbol{n}}_i) \;\cdot\; \frac{2\boldsymbol{u}_m\boldsymbol{u}_m}{j\omega\varepsilon\lambda_m} \;\cdot\; (\boldsymbol{I} \;-\; \hat{\boldsymbol{n}}_j\hat{\boldsymbol{n}}_j)\right) \;\cdot\; \boldsymbol{I}_j \quad (4.86)$$

Equation (4.86) can be implemented into an equivalent circuit consisting of four ports as shown in Fig. 4.15. The incident electric and magnetic field at each port of a UTLM node is mimicked by the incident voltage (V_i) and current (I_i) at each port of the circuit. The inductor ($L_i = \frac{\mu\Delta_i}{2S_i}$) mimics the inductive response of fields and the shunt capacitor ($C_m = \frac{\varepsilon\lambda_m}{2}$) mimics the capacitive response of fields in the node respectively. The transformer in the circuit relates stub voltages to incident voltages on the link lines and is defined as:

$$\boldsymbol{V}_{im} = (\boldsymbol{I} - \hat{\boldsymbol{n}}_i\hat{\boldsymbol{n}}_i) \cdot \boldsymbol{u}_m V_m \quad (4.87)$$

$$\boldsymbol{I}_{im} = \boldsymbol{u}_m \cdot (\boldsymbol{I} - \hat{\boldsymbol{n}}_i\hat{\boldsymbol{n}}_i) \cdot \boldsymbol{I}_i \quad (4.88)$$

where m=0, 1, 2.

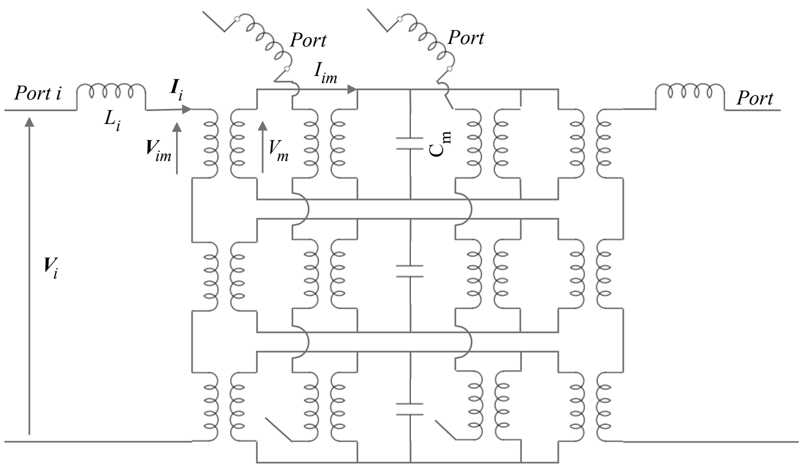

Figure 4.15 | Equivalent circuit for the 3-D UTLM node [4.4]

Equation (4.86) is rearranged to the form of incident and reflected voltages on the link lines:

$$\sum_{j=0}^{3}\left(\boldsymbol{\delta}_{ij} - j\omega L_j Y_j \delta_{ij} - \sum_{m=0}^{2} Y_j(\boldsymbol{I} - \hat{\boldsymbol{n}}_i\hat{\boldsymbol{n}}_i)\cdot\frac{\boldsymbol{u}_m\boldsymbol{u}_m}{j\omega C_m}\cdot(\boldsymbol{I} - \hat{\boldsymbol{n}}_j\hat{\boldsymbol{n}}_j)\right)\cdot V_j^i$$
$$= -\sum_{j=0}^{3}\left(\boldsymbol{\delta}_{ij} + j\omega L_j Y_j \delta_{ij} + \sum_{m=0}^{2} Y_j(\boldsymbol{I} - \hat{\boldsymbol{n}}_i\hat{\boldsymbol{n}}_i)\cdot\frac{\boldsymbol{u}_m\boldsymbol{u}_m}{j\omega C_m}\cdot(\boldsymbol{I} - \hat{\boldsymbol{n}}_j\hat{\boldsymbol{n}}_j)\right)\cdot V_j^r \quad (4.89)$$

This equation can be decoupled to two equations that related to the scattering for the inductive link line and capacitive stube respectively:

$$\{L\} \qquad (I - j\omega L_i Y_j)\boldsymbol{V}_j^i = -(I + j\omega L_j Y_j)\boldsymbol{V}_j^r \quad (4.90)$$

$$\{C\} \qquad \sum_{j=0}^{3}\left(\boldsymbol{\delta}_{ij} - \sum_{m=0}^{2} Y_j(\boldsymbol{I} - \hat{\boldsymbol{n}}_i\hat{\boldsymbol{n}}_i)\cdot\frac{\boldsymbol{u}_m\boldsymbol{u}_m}{j\omega C_m}\cdot(\boldsymbol{I} - \hat{\boldsymbol{n}}_j\hat{\boldsymbol{n}}_j)\right)\cdot V_j^i$$
$$= -\sum_{j=0}^{3}\left(\boldsymbol{\delta}_{ij} + \sum_{m=0}^{2} Y_j(\boldsymbol{I} - \hat{\boldsymbol{n}}_i\hat{\boldsymbol{n}}_i)\cdot\frac{\boldsymbol{u}_m\boldsymbol{u}_m}{j\omega C_m}\cdot(\boldsymbol{I} - \hat{\boldsymbol{n}}_j\hat{\boldsymbol{n}}_j)\right)\cdot V_j^r \quad (4.91)$$

Finally the scattering operation can be summarised for the ith port link line and mth stub:

$$\boldsymbol{V}_{il}^r = -\boldsymbol{V}_i^i + \sum_{m=0}^{2}(\boldsymbol{I} - \hat{\boldsymbol{n}}_i\hat{\boldsymbol{n}}_i)\cdot\boldsymbol{u}_m(V_m^r + V_m^i) \quad (4.92)$$

$$V_{ms}^r = (1 + R_m)V_m^i - R_m V_{ms}^i \quad (4.93)$$

where:

$$V_m^i = Z_0\sum_{j=0}^{3}\boldsymbol{u}_m\cdot(\boldsymbol{I} - \hat{\boldsymbol{n}}_i\hat{\boldsymbol{n}}_i)\cdot Y_j\boldsymbol{V}_{\boldsymbol{j}}^{\boldsymbol{i}} \quad (4.94)$$

$$V_m^r = R_m V_m^i + (1 - R_m)V_{ms}^i \quad (4.95)$$

$$\frac{1 - R_m}{1 + R_m} = \frac{2Z_0C_m - \Delta_t}{\Delta_t} \quad (4.96)$$

The choice of the time step Δ_t must not exceed the minimum time delay in the capacitive stub (Z_0C_m).

4.7 Conclusion

This chapter presents the basic theory of the Transmission Line Modelling (TLM) method and its implementation in conventional structured meshes and newly developed unstructred meshes. The governing of wave propagation in electromagnetic problems is mimicked by inductive and capavitive responses of voltage and currents in transmission line networks. The field experiences scattering process in the node and connecting process between neighbouring nodes to ensure field continuity. This is easily done in structured TLM by circuit analysis at each node as each port has same impedance. In unstructured TLM specific impedance relationship between electric and magnetic fields for each port of the node is established based on node dimensions to ensure continuous field propagation at each port. Finally the UTLM method will be applied to numerous wiring models in the subsequent chapters to evaluate its capability and accuracy.

References

[4.1] C. Christopoulos, *The Transmission-Line Modelling method:TLM* (Wiley-IEEE Press, 1995).

[4.2] C. Christopoulos, *The Transmission-Line Modeling (TLM) Method in Electromagnetics* (Morgan & Claypool, 2006).

[4.3] P. Sewell, J. G. Wykes, T. M. Benson, C. Christopoulos, D. W. P. Thomas, and A. Vukovic, "Transmission-line modeling using unstructured triangular meshes," (2004).

[4.4] P. Sewell, T. M. Benson, C. Christopoulos, D. W. P. Thomas, A. Vukovic, and J. G. Wykes, "Transmission-line modeling (TLM) based upon unstructured tetrahedral meshes," IEEE Transactions on Microwave Theory and Techniques **53**, 1919–1928 (2005).

[4.5] S. Akhtarzed and P. John, "Solution of Maxwell's equations in three space dimensions and time by the t.l.m. method of numerical analysis," (1975).

[4.6] S.-W. Cheng, T. K. Dey, and J. Shewchuk, *Delaunay Mesh Generation* (Taylor & Francis, 2012), 1st ed.

5

Canonical problems simulation

This chapter uses the UTLM method to model wave propagation and coupling along single wires, a T-junction model and a crossed-junction model. The accuracy of the direct meshing is achieved by introducing mesh refinement around the wire. Different meshing parameters and geometry descriptions are investigated in order to obtain result convergence and computational efficiency.

***

5.1 Introduction

This chapter investigates some canonical wire problems using the Unstructured Transmission Line Modelling (UTLM) method introduced in chapter (4). A canonical single wire model is first tested in two different excitation ways. One is to expose the wire to a plane-wave excitation; the resonant frequency of the induced current is investigated using different mesh strategies and geometrical descriptions in order to investigate the influence of simulation parameters on convergence. The influence of different radii is then investigated based upon simulation parameters obtained. The other set-up is to impose a modal excitation at the end of the wire and to investigate wave propagation along the wire section by means of S-parameters.

In terms of the meshing strategies used in this chapter tetrahedral meshes of good quality, which is controlled by the parameter quality factor (Q) in the meshing stage, but coarse sizes are first generated and then refined by cubic or tetrahedral meshes of size $\lambda/10n$ where n increases from 1 until convergence and λ corresponds to the wavelength of interest. Then a local mesh refinement technique is employed around the wire, in order to eliminate the impact of dramatic mesh change in the near field region. The local mesh refinement is controlled by a cylindrical region that surrounds the wire with a target volume in the region; this will explained more in subsequent sections. Once these parameters are decided, the number of segments that describes the cross section of the wire itself is investigated.

This chapter also explores the ability of the UTLM method to build and model canonical junction models. The first junction studied is a T-junction model that consists of three conductors with the third conductor extruded from a single-wire model. The second junction studied is formed by extruding another conductor at the other side of the wire hence forming a crossed-junction model. The behaviour of these junctions is investigated by evaluating the wave propagation through the section using the meshing parameters and geometrical descriptions suggested by the single wire model.

5.2 Single Wire Model excited by a Plane Wave

This section focuses on investigating a short single wire model illuminated by a plane wave. Different meshing methods are first explored in order to evaluate the influence on convergence and efficiency. The geometrical description, specifically the number of segments that discretises the wire cross section, is then investigated. Finally the single wire model is investigated with different wire radii.

5.2.1 Problem definition

The geometry used for the simulation of the single wire is built as follows. A straight wire is placed in free space as shown in Fig.5.1. The wire has a length $l = 0.5$ m, with radius a normalised to the wavelength λ at 300 MHz. The shape of the wire is constructed as an M-sided polygonal tube. A larger value of M gives a better description of the circular cross section of the wire. The distance of the computational space boundary to the wire is defined as D.

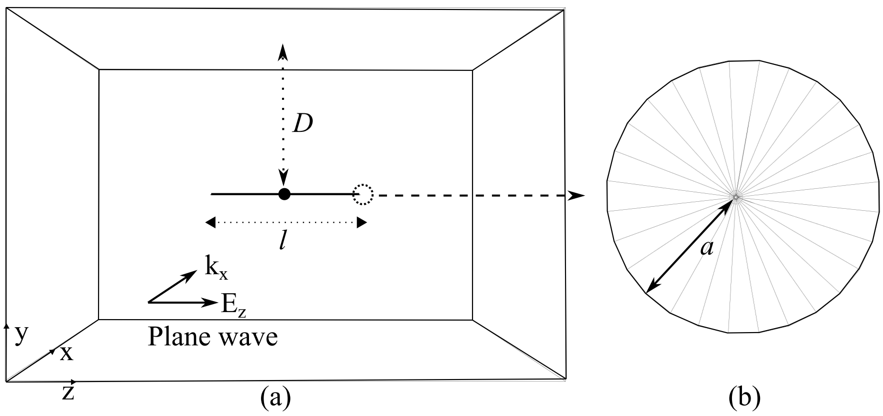

Figure 5.1 | Single wire model set-up a) in the computational space and b) the representation of the cross-section as an M-sided polygon

A plane wave with a frequency bandwidth 100 MHz to 500 MHz is activated at the broad side of the wire with the field polarisation in the direction of $+z$, as shown in the inset to Fig.5.1. Both ends of the wire are open-circuited; therefore the current evaluated, as an integration of magnetic fields surrounding wire surface, is evaluated at the middle of the wire where the peak value is obtained.

5.2.2 Global mesh evaluation

A convergence test with mesh size is first performed for a wire with length $l = 0.5m$ and radius $r = 1mm$. The wire cross section is constructed using a 30-segmented polygon to provide visibly smooth circular configuration. The length corresponds to an analytic first resonant frequency at 300MHz of a half wave dipole antenna. The wire is placed in an empty space whose boundary is placed 0.5m away from the wire in all dimensions in order to provide an adequate simulation space.

The model is first coarsely meshed with good quality (quality of tetrahedral cells and triangular surfaces set less than or equal to 2 in the UTLM mesher) tetrahedral elements as shown in Fig. 5.2. It can be seen that without any size constraints in the

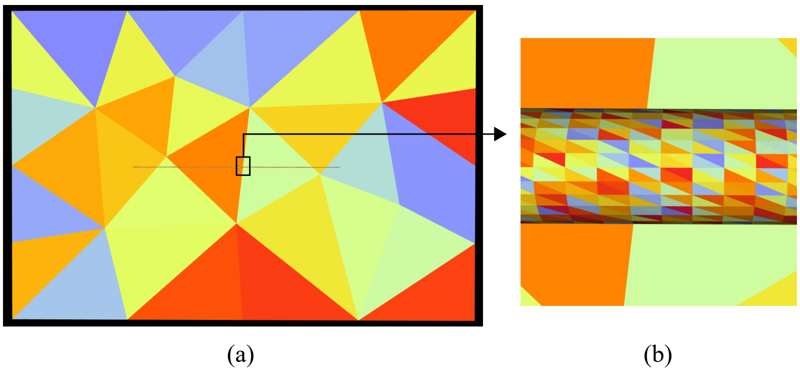

Figure 5.2 | Single wire model mesh plot with a) Coarsely sized tetrahedral mesh plot of the single-wire model with well shaped elements and b)mesh details of the wire surface

free space, meshes in the free space and around the wire are on two different scales. The mesh statistics show that the volume of the majority of the meshes in the empty space is larger than $10^{-3}m^3$. In contrast, the region near the wire model is meshed with tetrahedra whose volume is below $10^{-8}m^3$ in order to describe accurately the wire cross-section.

Fig. 5.3 shows the simulation result for the coarsely sized mesh model. It illustrates the general behaviour of the induced current at the middle section of the wire up

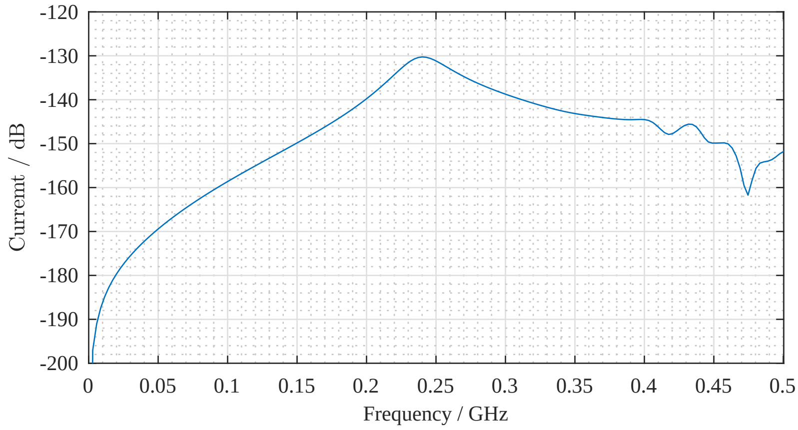

Figure 5.3 | Frequency response of the normalised current on the single-wire model with coarse mesh

to 400MHz and the resonant frequency at 240MHz. However it also shows unstable behaviour after 400 MHz and the resonant frequency is far away from the expected 300 MHz. This may be explained by two aspects. Firstly the mesh in the empty space is too large to accurately capture the frequency response at higher frequencies. Secondly there is a dramatic difference in mesh sizes between the free space and the region around the wire.

The meshing method above is now modified by inserting in the free space uniform cubic cells with a mesh size λ/N, where N is a multiple of 10. Fig.5.4a shows the meshed model with cubic meshes of size $\lambda/10$, which is usually the rule-of-thumb choice for accurate TLM simulation, inserted in the free space and Fig.5.4b shows details around the wire surface. Compared to Fig.5.2, it can be seen that the free space region is refined with uniform cubic meshes of the demanded size while the centre region remains unaffected. One advantage of this approach is to ensure that the size of each mesh in the whole problem satisfies the maximum mesh size guidance of one tenth minimum wavelength of interest for the transmission line modelling (TLM) method [5.2,5.3].

Fig.5.5 shows the frequency response of the wire for different values of N, i.e. for different discretisation lengths as a fraction of λ applied in the empty space. A

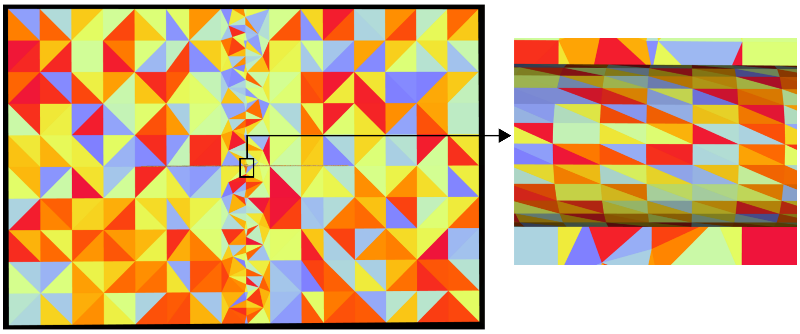

Figure 5.4 | Single wire model mesh plot with a) cubic cells of size $\lambda/10$ inserted in the background and b)mesh details on the wire surface

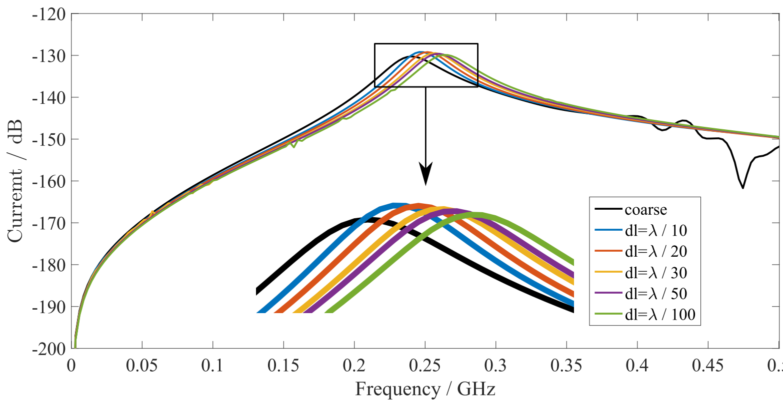

Figure 5.5 | Frequency response of the induced current on the single wire model with different mesh sizes

more stable higher frequency response is observed once the finer sized cubic meshes are inserted in the free space region. The figure also shows the improvement of the result as the resonant frequency shifts with decreasing mesh sizes from $\lambda/10$ to $\lambda/100$. The frequency at resonance as a function of the fraction number N, as plotted in Fig.5.6, indicates numerical convergence as N is increased. The result does not not converge to the expected 300 MHz due to two reasons. First, the open-circuit set-up causes unavoidable edge effects at the end of the wire and these result in a resonant frequency shift. Secondly, with the minimum mesh size used, $\lambda/100$, corresponding to a 0.01 m length of the cubic cell at 300 MHz, there are still big differences of meshes sizes between the free space region and around the wire.

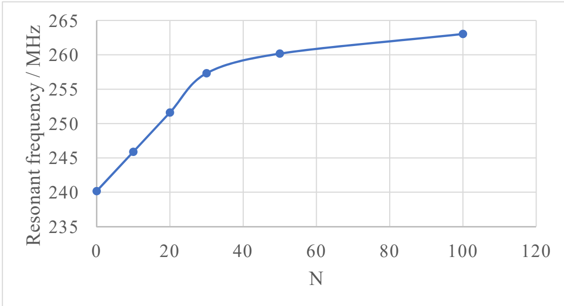

Figure 5.6 | Resonant frequency of the single wire model as a function of fraction number N of the meshing size

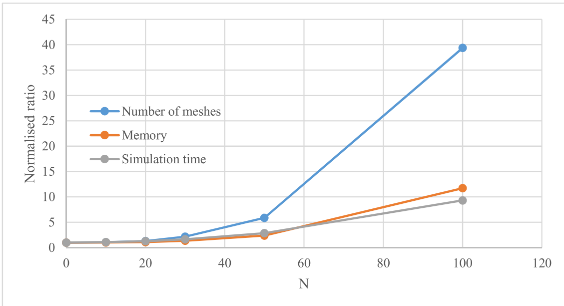

Figure 5.7 | Computational expense of the single wire model as a function of fraction number N of the meshing size

It is however difficult to further refine the meshes in the whole problem if the simulation efficiency is taken into consideration. Fig.5.7 plots the total number of meshes, the memory occupied and the total simulation time taken for a two-million-step simulation versus value of N that corresponds to $\lambda/10N$ mesh sizes; all plots are normalised with respect to the coarse mesh case. It is impressive that the $\lambda/10$ refined mesh shows approximately similar amount of meshes, memory occupation and time cost to the coarse mesh case with significant simulation accuracy improvement. These computational resource factors increase gradually for the first three cases but the rate of increase with N soon gets faster for $N > 50$. The number of meshes curve sees most significant increase and its ratio reaches 40 for a $\lambda/100$ mesh. Both the memory occupation and time cost are found to be around 10 times bigger at $N = 100$. These computational requirements would be greater if larger simulation space were applied because the number of global meshes increases as the volume of the computational space increases. It is usually the case to use large simulation spaces when modelling practical large electrical systems such as air-planes and cars. It is therefore suggested to apply a mesh size $\lambda/20$ or $\lambda/30$ as they are fine enough to capture the first order accuracy while keeping simulation efficiency.

5.2.3 Localised mesh refinement evaluation

It is noticed from simulations above that a significant difference in mesh sizes between the wire region and the free space may affect the result convergence due to the dispersion error. Although refining the whole model is impractical because of the huge computational cost, the 3D-UTLM is able to provide an alternative, which is to refine only the desired region with specific volume constraints as described in (signpost). This region acts as a buffer area that refines meshes in the region and smooths the huge different in sizes between meshes around the wire surface and in the free space. In order to apply this method to a single-wire model, a cylindrical region centred on the wire centre with an expanding radius R is defined as shown in Fig. A minimum volume size v is applied in the region, with meshes near the centre more refined and near the boundary less refined.

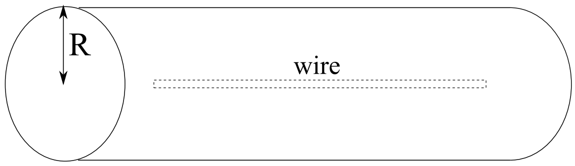

Figure 5.8 | Localised mesh refinement region defined as a cylinder centred on the wire wire centre

Fig.5.9 shows the cross-sectional view of the meshed model for decreasing volume target from a) a normal mesh of size $\lambda/20$ without localised refinement to b) $v = 10^{-7}m^3$, c) $v = 10^{-}-8m^3$ and d) $v = 10^{-9}m^3$ in the region $R = 0.02$ m while keeping the mesh size outside the region $\lambda/20$. These figures indicate a good structured cubic mesh of relatively large size in the outer space in yellow and small unstructured elements in the inner space in blue. Comparing Fig.5.9 a) and b), there is little difference visible between a non-local refined model with $\lambda/20$ mesh and a local refined mesh model with volume constraints $v = 10^{-7}m^3$. There is improvement

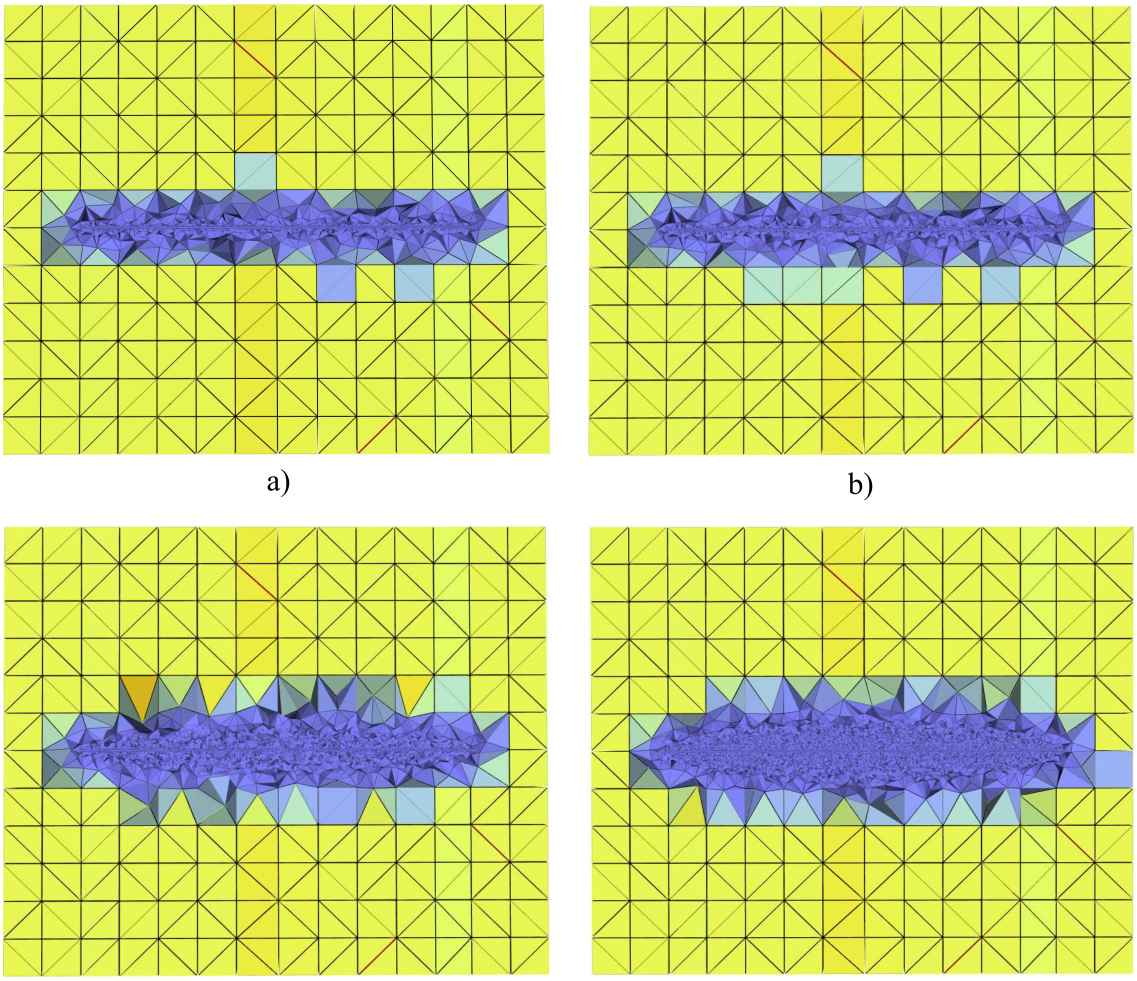

a) b) c) d)

Figure 5.9 | Mesh cross-sectional plot for a) normal mesh of size $\lambda/20$; b)localised mesh refinement in $R = 0.02$ m, $v = 10^{-7}$ m^3; c) $R = 0.02$ m, $v = 10^{-8}$ m^3; d) $R = 0.02$ m, $v = 10^{-9}$ m^3

found when a finer volume size restriction is used as shown in Fig.5.9 c) and d). As the inner region gets descretised more finely it shows more a more even mesh size distribution and smoother connection to the outer region. This can be observed more clearly from the mesh statistics chart shown in Fig.5.10. It illustrates a significant increase in the number of meshes with a volume between $4.55 \times 10^{-10}m^3$ and $1.22 \times 10^{-8}m^3$, especially for the model in Fig.5.9 d) with $v = 10^{-9}m^3$.

The simulation result shown in Fig.5.11 indicates the resonance shift with decreasing

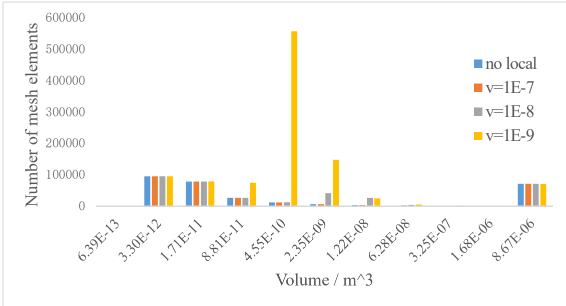

Figure 5.10 | Mesh stats for different volume constraints in Fig.5.9

volume constraints in the local refinement region. For the first two cases with $v = 10^{-6}m^3$ and $v = 10^{-7}m^3$, the frequency response shows indistinguishable difference from the the case without local mesh refinement. The frequency at resonance is shown increased from about 250 MHz for non-local model to 260 MHz for $v = 10^{-8}m^3$ and 270 MHz for $v = 10^{-9}m^3$, in a region of size $R = 0.02$ m. The normalised computational expenses with respect to different v is also shown in Fig.5.12, which illustrates comparable results to the mesh statistics and simulation results. It seems that although with $10^{-9}m^3$ minimum volume constraints higher resonant frequency is obtained, dramatic increase of computational resources is required compared to the case $v = 10^{-8}m^3$. This leads to further investigations that expands the radius of the local refinement region while maintaining the minimum volume size as $v = 10^{-8}m^3$.

Fig.5.13 shows the cross-sectional plots of the meshed model with increasing refinement region radius R from 0.02m to 0.05m, keeping outer region meshed by cubic cells of size $\lambda/20$ and the volume target inside the region $10^{-8}\ m^3$. Comparing to the noticeable boundary that differentiates large crude meshes in the yellow region and fine meshes in the blue region in Fig.5.13 a) and b), Fig.5.13 c) and d) are seen to improve the dramatic connection boundary. It is also noted that in Fig.5.13 c) and d) who have a bigger blue region than Fig.5.13 a) and b), meshes grow slower hence more small sized tetrahedral meshes are generated. This observation is supported by the mesh statistics shown in Fig.5.14, where the number of meshes whose volume

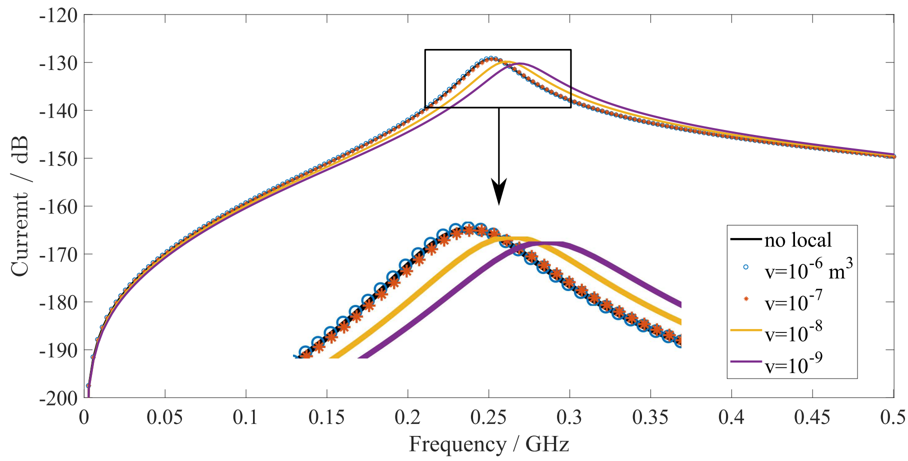

Figure 5.11 | Frequency response of the induced current on the single-wire model for different volume constraints in the refinement region R=0.02 m

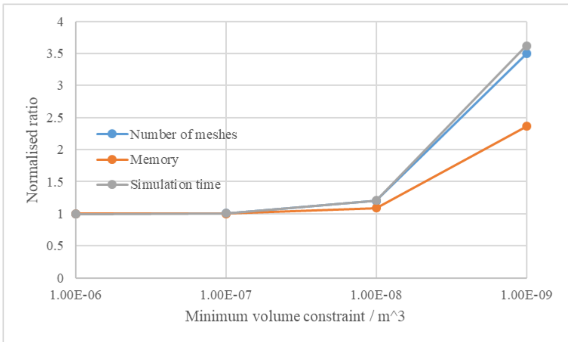

Figure 5.12 | Computational data for different volume constraints in mesh refinement region R=0.02 m,normalised to the case without local mesh refinement

is in the range $2.35 \times 10^{-9}m^3$ to $6.28 \times 10^{-8}m^3$ is observed to increase as the region expands. The simulated frequency response for expanding local refinement region is shown in Fig.5.15, compared to the case without refinement. The resonant frequency is observed shifting from 260 MHz for $R = 0.02$ m to 270 MHz for $R = 0.05$ m and quickly convergences as the region expands.

Fig.5.16 shows the computational requirements as a function of refinement region R, normalised with respect to the case without localised mesh refinement. The three factors, memory occupation, number of meshes and simulation time cost are observed increasing accumulatively as the refinement region expands. Compared

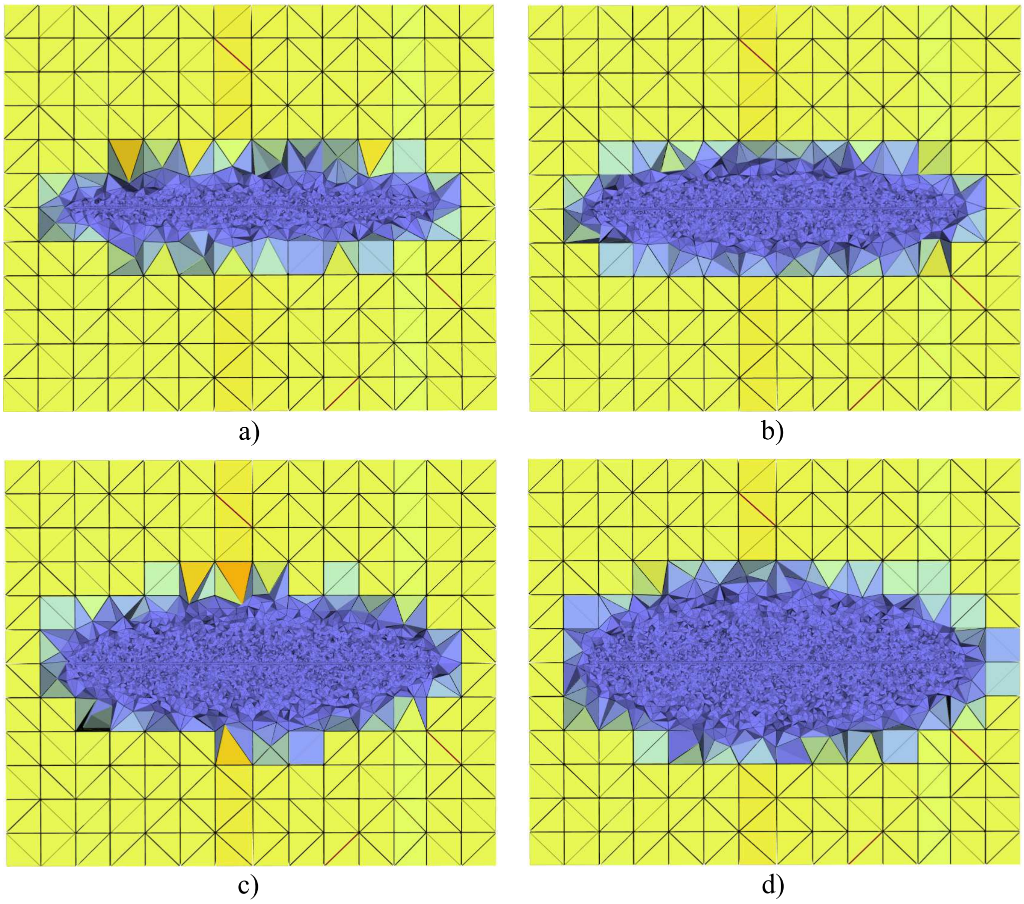

Figure 5.13 | Mesh cross-section view for different local refinement regions with volume constraints $v = 10^{-9}m^3$

to the previous meshing method that applies local mesh refinement in the region $R = 0.02$ m and minimum volume constraints $v = 10^{-9}m^3$, using $R = 0.05$ m and $v = 10^{-8}m^3$ achieves same result of 270 MHz while requiring lower computational expenses, typically 28% less time consumption and memory occupation. It is therefore more efficient to adopt the latter as the meshing strategy.

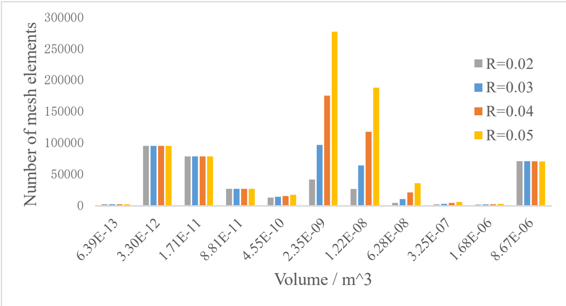

Figure 5.14 | Mesh stats for different different local refinement regions in Fig.5.13

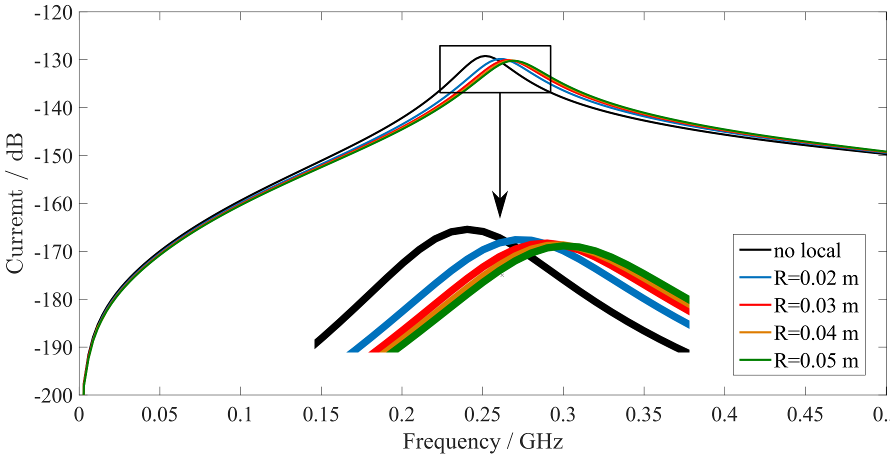

Figure 5.15 | Frequency response of the induced current on the single-wire model with increasing region size for local mesh refinement

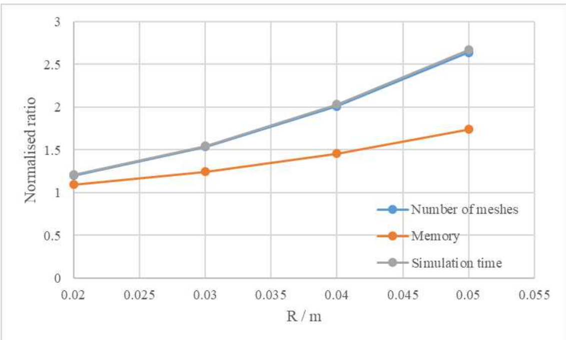

Figure 5.16 | Computational data for different mesh refinement regions, normalised to the case without local mesh refinement

5.2.4 Geometrical description of the wire

In addition to the proper meshing strategies, it is also desired to explore the effect of geometry description on both the frequency response and computational requirements. Specially in this model, the description of the single-wire model is principally controlled by the number of segments that discretises the cross-section of the wire. Increasing the number of segments delivers a polygon that more closely represents the circular cross-section of the practical wire. However increasing the number of segments produces small edges and this requires meshing of small features. Consequently a larger number of small meshes is produced . Fig.5.17 shows the cross-section view of a discretised wire that has 6, 10, 20 and 30 segments respectively. It

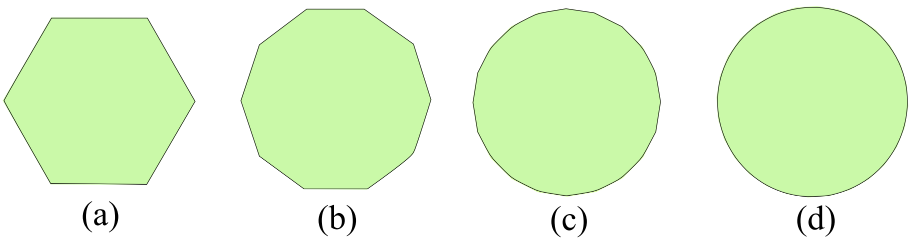

Figure 5.17 | Cross section of the wire geometry with a) 6 segments, b) 10 segments, c) 20 segments and d) 30 segments.

is observed that using 20 and 30 segments to describe the wire cross-section is able to generate polygons that are visibly better representing of the circular cross-section of the wire than 6 or 10 segments. In contrast, obvious edges are found to define the cross-section when using 6 or 10 segments as shown in Fig.5.17 (a) and (b).

The simulated result presented in Fig.5.18 shows fast convergence with the number of segments used to define the wire cross-sections. Although there is a minor magnitude drop, from the 6-segmented model to the 30-segmented model at the resonance, as shown in Fig.5.18, the effect on the resonant frequency is seen to very small. The computational expense with respect to the number of segments shown in Fig. 5.19 shows that 6 - 10 segments generate almost 20% less meshes, cost 35% to 40 % less memory and take 10% less simulation time compared to the 30-segmented model. As a result, reducing the number of segments of the wire cross-section helps reduce geometrical complexity while maintaining sufficient accuracy. It is therefore recommended to use 6 or 10 segments to describe the wire cross-section in the geometry construction.

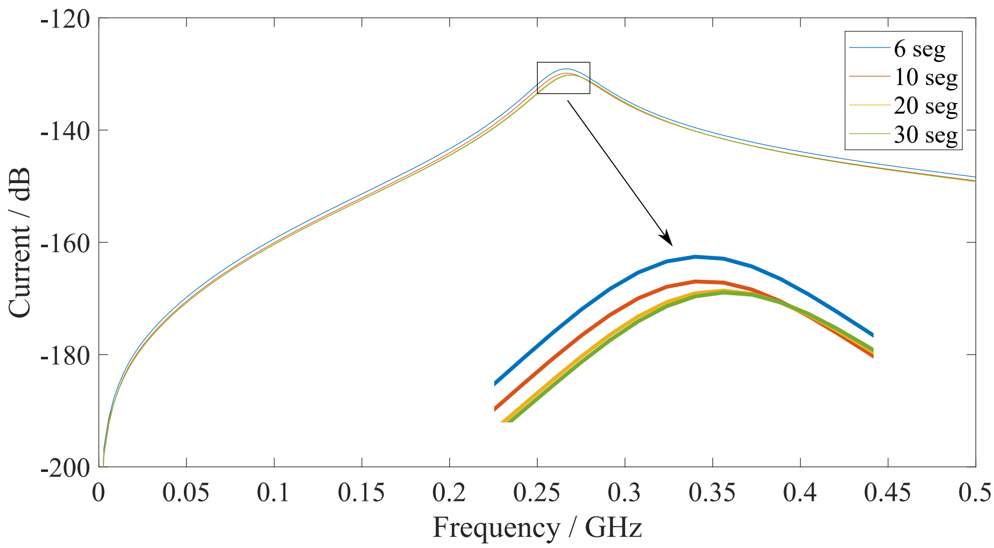

Figure 5.18 | Frequency response of the induced current on the single-wire model for different numbers of segments

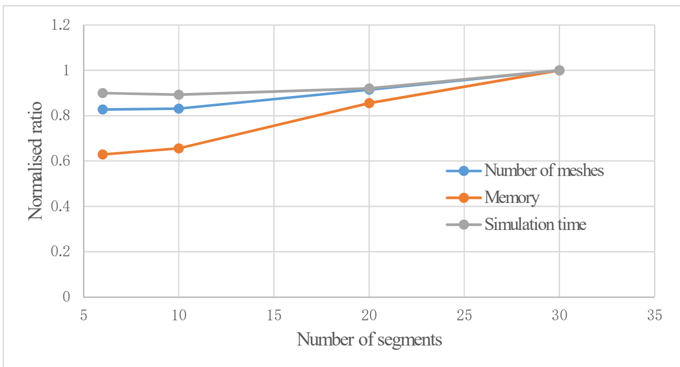

Figure 5.19 | Computational data for different number of segments, normalised to the 30-segmented model

5.2.5 Resonance for different wire radii

After exploring necessary parameters, it is desired to investigate the effect of radius on the resonant frequencies of the single wire model exposed to the plane-wire excitation. Previously, different meshing strategies and geometrical description are explored on a wire of radius $r = 1$ mm, or 0.001λ at 300 MHz. This section evaluates wire models of radius 0.5mm, 2mm, 4mm, 6mm, 8mm and 10mm, which correspond to 0.0005λ, 0.002λ, 0.004λ, 0.006λ, 0.008λ and 0.01λ respectively. Based on the guidelines found in the previous subsections, these wires are meshed using a global mesh size $\lambda/20$ and local mesh refinement in the region 0.05m around the wire with volume target $v = 10^{-8}m^3$. These wires are constructed using 30 segments to discretise the cross-section.

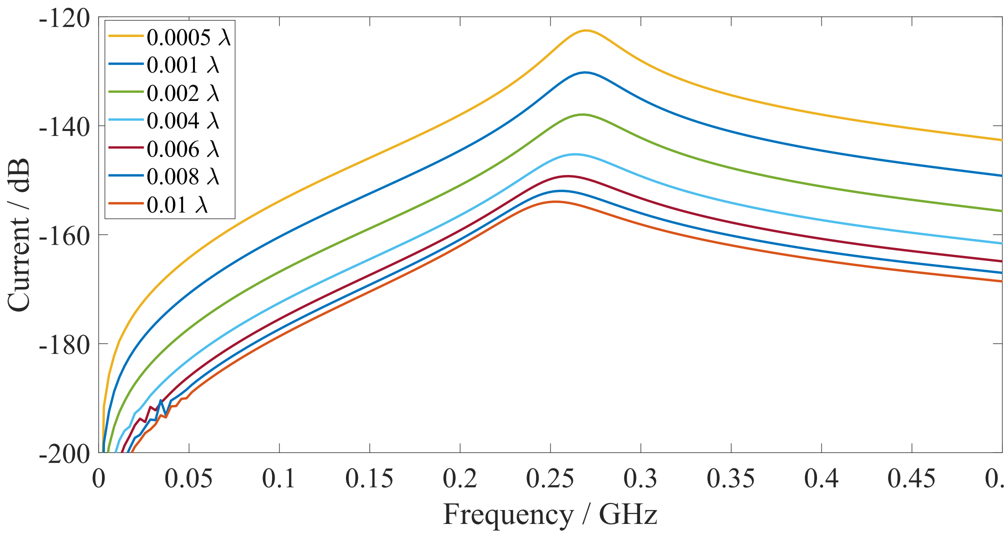

Figure 5.20 | Frequency response of the induced current on the single-wire model with varying wire radii

The frequency response obtained for the different radii is shown in Fig.5.20 and the corresponding resonant frequency as a function of the wire radius is shown in Fig.5.21. It is observed in Fig.5.20 that the magnitude of the induced current declines as the radius increases. The declining rate is found faster for radius below $0.004\ \lambda$ than for radius above. Fig.5.21 illustrates a monotonically decreasing trend of the resonant frequency. The rate of decrease is very small once the radius is less

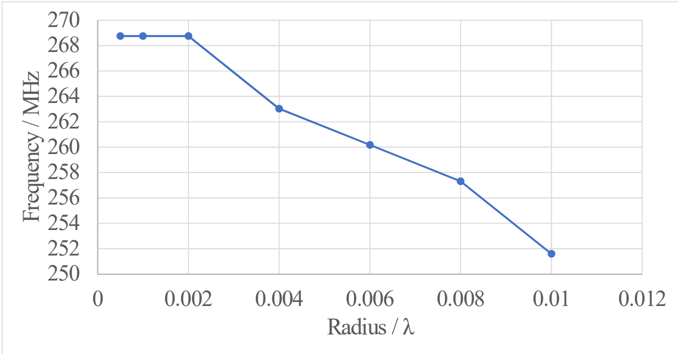

Figure 5.21 | Resonant frequency as a function of radius of wire, normalised to wavelength

than 0.002 λ. When the wire radius increases, the edge effects are seen to shift the resonant frequency at the ends of the wire.

5.2.6 Section summary

This section performs the general procedure of the UTLM simulation on a single-wire model of length 0.5m under a plane wave excitation. Different meshing strategies were investigated in order to find sufficient simulation parameters. It is found that using a background mesh of size $\lambda/20$ combining localised mesh refinement strategy in the region 0.05m around the wire with minimum volume restraints of $10^{-8}m^3$ presents convergent results of the resonant frequency at 270MHz with efficient computational cost. It needs to be recognised that the resonant frequency of the wire cannot reach the expected half wave resonant resonant frequency of 300 MHz, due to the open-circuit treatment at both ends and the method of the excitation. Different numbers of segments of the wire cross-section are shown to have minor effect on the resonance behaviour but less segments show decreasing computational costs compared to large number of segments. Further simulations show the decreasing of resonant frequencies and current magnitudes when the wire radius increases.

5.3 Evaluation of a Single Wire Model and Junctions with Modal Excitation

The previous section investigates the general behaviour of single wire models to a plane-wave excitation and obtains some generic simulating parameters for further simulations. It is also desired to see the behaviour of the wire model as a transmission line section to propagate waves. In this case the wire is excited from one end and the observation is made in terms of S-parameters. In addition, the capability of the UTLM method to model complex structures such as junctions is evaluated. Similar to the section 5.2, the convergence of S_{11} and S_{21} parameters on a single wire model is investigated, exploring various meshing strategies and geometrical descriptions. Then the way making the junction model is described and simulations are performed to investigate the effect of the junction on the wave propagation.

5.3.1 Problem description

In the first model, a single wire model is built similar to the previous section. The wire has a length of 0.3m, radius of 1mm and is placed 0.1m above a U-shape ground plane, as shown in Fig. 5.22 Each end of the wire is connected to a coaxial probe in order to support a Transverse Electromagnetic (TEM) mode wave. The coaxial probes have an outer radius of 3mm, a length of 5mm and a relative dielectric

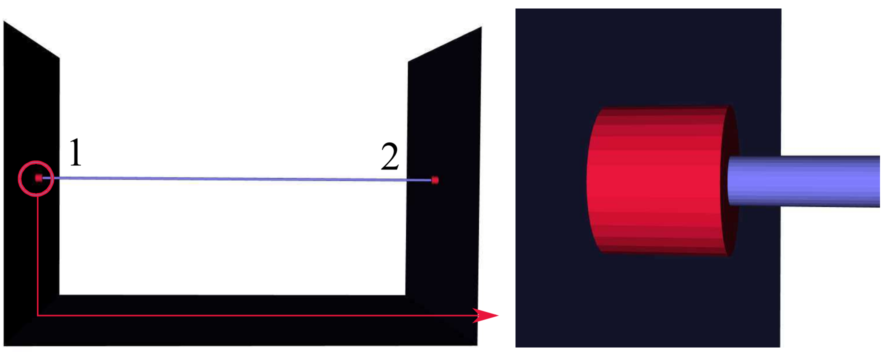

Figure 5.22 | Geometry of a single wire model above the ground plane, with coaxial probe details on the right

constant $\varepsilon_r = 1$ that corresponds to air as the dielectric layer. These two coaxial probes are then connected the side boards of the U-shape ground plane as shown on the right of Fig. 5.22 The wire is excited from port 1 by a TEM mode wave solved at 400MHz with a bandwidth from 100MHz to 500MHz The S_{11} and S_{21} parameters are observed from port 1 and port 2 respectively.

5.3.2 Global mesh evaluation

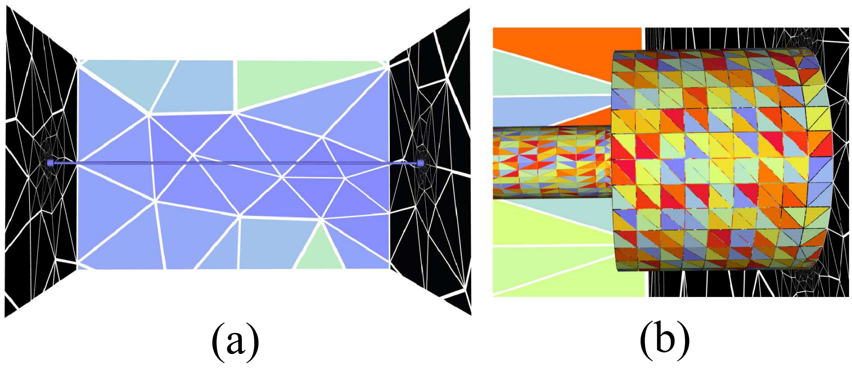

Figure 5.23 | Coarsely sized tetrahedral mesh of the single wire model with b) meshes around the wire surface

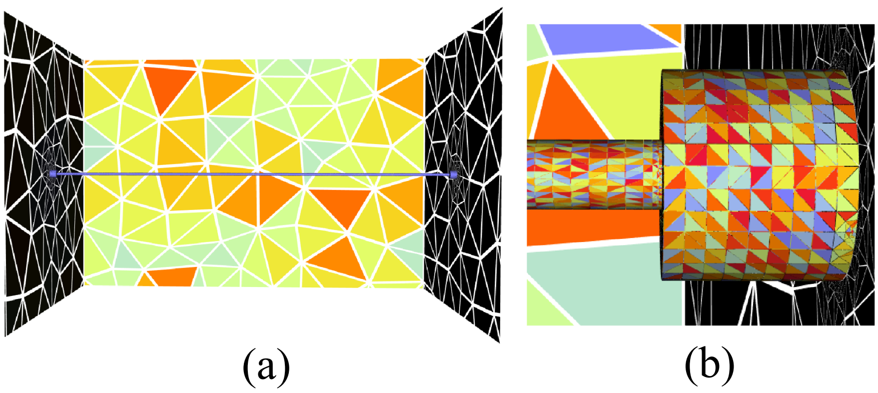

Figure 5.24 | Volume refined tetrahedral mesh of the single wire model with b) meshes around the wire surface

The simulation is first performed on the single wire model with varying mesh sizes in the computational space. Similar to section 5.2, the model is first coarsely meshed with good quality (Q = 2) tetrahedral cells. That means that the cell shape of meshes is restricted by a quality factor less than 2, but there is no mesh size constraints in the computational space. Fig.5.23 (a) and (b) shows meshes in the background and

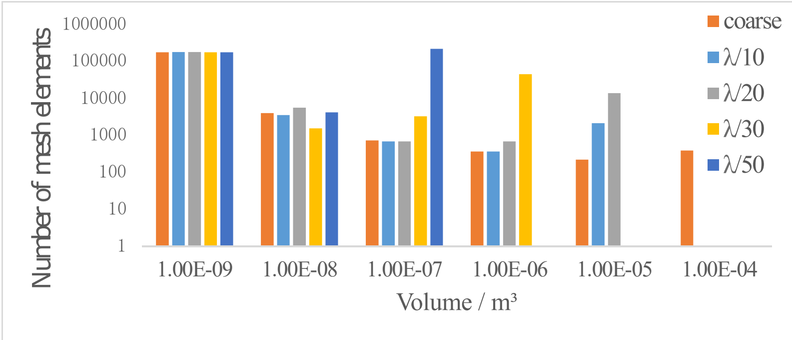

Figure 5.25 | Number of meshes in log scale as a function of cell volume in m^3 for decreasing meshing command with respect to wavelength

around the wire surface respectively. It can be seen that while both regions near the wire surface and in the background meshed with good quality tetrahedral elements, meshes around the wire surface see a much finer size.

In comparison to Fig.5.23, Fig.5.24 plots the model meshed with a maximum volume 1.56×10^{-5} m^3 that corresponds to a cubic cell size $\lambda/20$ (2.5 cm) , where λ corresponds to the maximum frequency of interest. Meshes in the background are found refined with demanded mesh size, although they are still in very large scale compared to meshes around the wire surface. In contrast, meshes near the wire surface are in very similar scale to the coarsely sized mesh model, as they are already in very fine size.

This can be demonstrated using the mesh statistics chart shown in Fig.5.25 for different mesh refinement targets in terms of volume constraints that correspond to cubic cells of the size $\lambda/10$ (5 cm), $\lambda/20$ (2.5 cm), $\lambda/30$ (1.667 cm) and $\lambda/50$ (1 cm) respectively. Most meshes near the wire surface are below 10^{-5} m^3. It can be seen that meshes in the simulation space with coarsely meshed method are found larger than 10^{-5} m^3 and therefore replaced by smaller sized grades.

The simulation results of S_{11} and S_{21} for various meshing constraints are plot in Fig. 5.26 and Fig. 5.27 respectively, illustrating the general behaviour of wave through a single wire model above a ground plane. Due to the impedance mismatching between the coaxial probe and the wire section, the wave is only able to propagate at the resonance. From the simulation result, the coarsely sized mesh model is able to plot the general shape of the wave behaviour for both S_{11} and S_{21}, however it sees the limit resolving accuracies at higher frequencies due to its large mesh cells in the free space. On the other hand,as the mesh size is reduced from $\lambda/10$ to $\lambda/50$, the frequency at the resonance is found shifting from around 450 MHz to around 475 MHz. There is no deterministic pattern to describe the magnitude change of S_{11} at the resonance with respect to different meshes, however they are all below -20 dB.

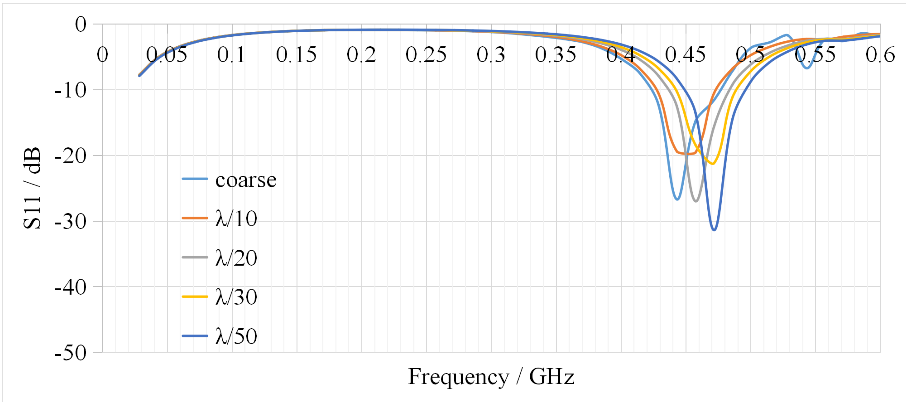

Figure 5.26 | Comparison of S_{11} for a coarsely sized mesh (runtime: 18586 s, memory: 551 MB), $\lambda/10$ (runtime: 5.21 h, memory: 556 MB), $\lambda/20$ (runtime: 5.54 h, memory: 556 MB), $\lambda/30$ (runtime: 6.49 h, memory: 621 MB), $\lambda/50$ (runtime: 11.28 h, memory: 787 MB)

The computational requirements are shown in the caption for Fig.5.26, which shows rapid increase of simulation time between $\lambda/30$ and $\lambda/50$. In order to get expected convergence of resonant frequency around 500 MHz, it can be predicted that further mesh refinement is required in the simulation space. This requires dramatic increase of computational resources according to the trend. As for the plane wave excitation case described in section (5.2), this calls for a change of meshing strategy that keeps outer region relatively crudely meshed and refines only a specific region around the wire.

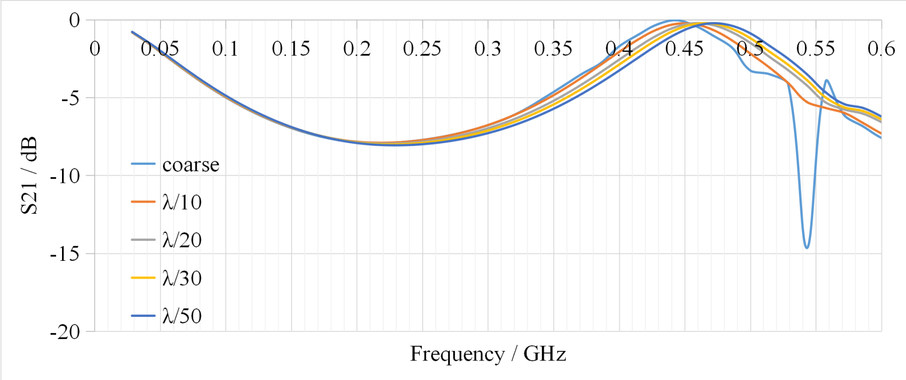

Figure 5.27 | Comparison of S_{21} for a coarsely sized mesh, $\lambda/10$, $\lambda/20$, $\lambda/30$ and $\lambda/50$

5.3.3 Localised mesh refinement evaluation

This section focuses on investigation of S-parameters with the utilisation of local mesh refinement. Similar to section (5.2), the local refinement technique is controlled by the region radius R and minimum volume size v that grows gradually from inside outwards. It is noted from the previous section that the majority of meshes around the wire is below 10^{-9} m^3, therefore volume constraints of 10^{-9} m^3 is selected in increasing refinement regions $R = 0.01$ m, $R = 0.02$ m and $R = 0.03$ m respectively. Fig. 5.28 compares the meshed model without local mesh refinement

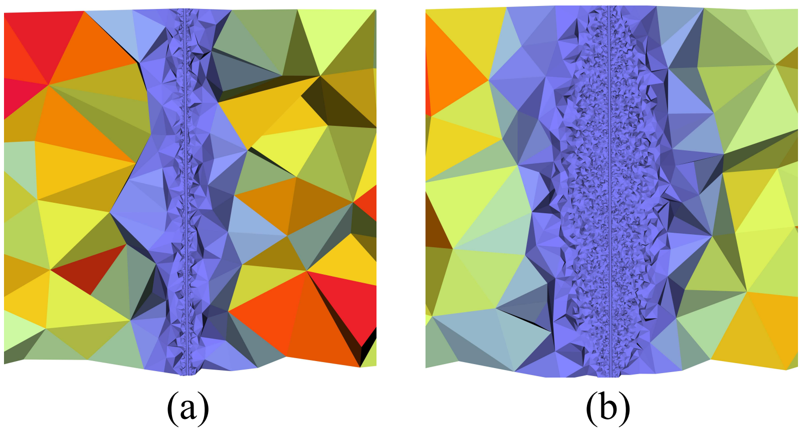

Figure 5.28 | Cross-sectional plot of meshed single wire model with a) no local mesh refinement, b) local mesh refinement of $R = 0.02$ m, $v = 10^{-9}$ m^3; both in global mesh that correspond to $\lambda/20$

and with volume constraint $v = 10^{-9}$ m^3 in the region $R = 0.02$ m respectively, in a background mesh $v = 1.56 \times 10^{-5}$ m^3 that corresponds to cubic cells of size $\lambda/20$

at 600 MHz. It clearly shows the expansion of fine meshes near the wire model, as well as a smoother connection between fine meshes inside and crude meshes outside for the case with local refinement.

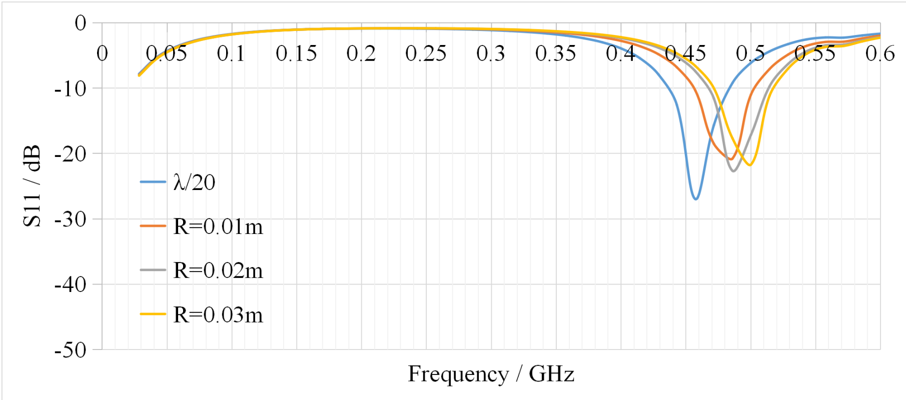

Figure 5.29 | Comparison of S_{11} for tetrahedral meshes of size $\lambda/20$ (runtime: 5.55 h, memory: 556 MB) and with local refinement of target volume 10^{-9} m^3 in the region $R = 0.01$ m (runtime: 8.24 h, memory: 670 MB), $R = 0.02$ (runtime: 14.94 h, memory: 1083 MB) and $R = 0.03$ m (runtime: 33.39 h, memory: 1797 MB)

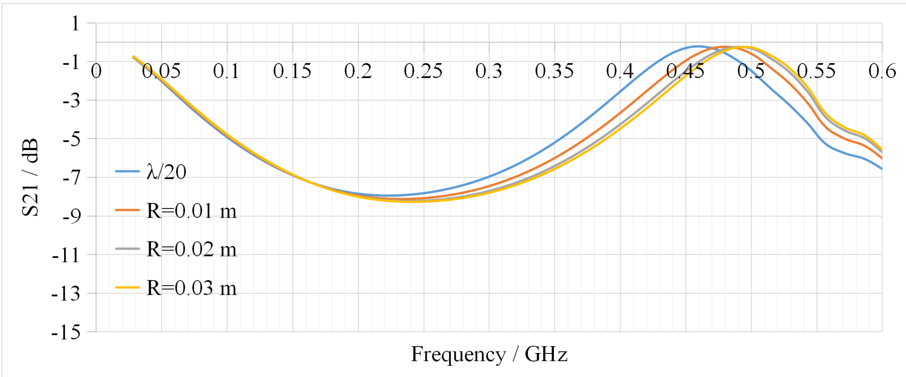

Figure 5.30 | Comparison of S_{21} for a coarsely sized mesh, $\lambda/10$, $\lambda/20$, $\lambda/30$ and $\lambda/50$

Figs. 5.29 and Fig. 5.30 shows the S_{11} and S_{21} for expanding local mesh refinement regions from 0.01 m to 0.03 m respectively, all with mesh volume constraint of 10^{-9} m^3 inside. The computational requirement are seen to the caption of Fig. 5.29. It can be seen that with local mesh refinement, both S_{11} and S_{21} gets apparent improvement and reach 500 MHz at resonance for R=0.03m. However it still needs to be noted that computational expenses increase dramatically, almost 6 times longer time taken for the R=0.03 m case compared to the non-local-refinement case.

5.3.4 Geometry description of the wire and probe

The effect of the description of the wire geometry, that is the number of segments that discretises the wire cross section in the model is now evaluated. Fig.5.31 shows the cross sections of the coaxial probe used in this simulation with 6, 10, 20 and 30 piece-wire linear segments respectively. All models are meshed using a tetrahedral mesh of maximum volume 1.56×10^{-6} m^3 that corresponds to a cubic cell of size $\lambda/20$ at 600 MHz. The number of segments that discretises the cross section is

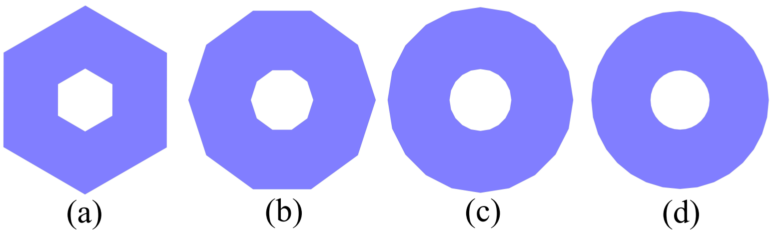

Figure 5.31 | Cross section of the coaxial probe with a) 6 segments, b) 10 segments, c) 20 segments and d) 30 segments

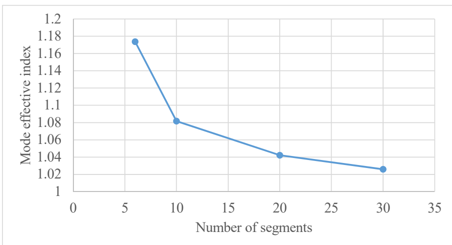

Figure 5.32 | Mode effective index of the coaxial probe as a function of number of segments used to describe in the model

first found affecting the sampled mode profiles that propagates in the cross section due to the change of the shape. (signpost to previous chapter for introducing the mode solving) Fig.5.32 shows the mode effect index (neff) that is solved to sample the transverse electromagnetic (TEM) mode wave propagating through the cross section. The value of $neff$ can be seen converging to 1 as the number of segments increases.

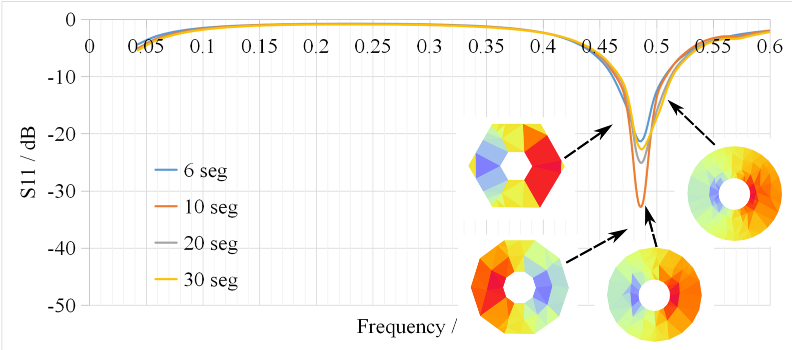

Figure 5.33 | Comparison of S_{11} for 6 segments runtime: 14.02 h, memory: 591 MB), 10 segments (runtime: 14.56 h, memory: 630 MB), 20 segments (runtime: 16.47 h, memory: 871 MB) and 30 segments (runtime: 18.48 h, memory: 1083 MB) in the cross section

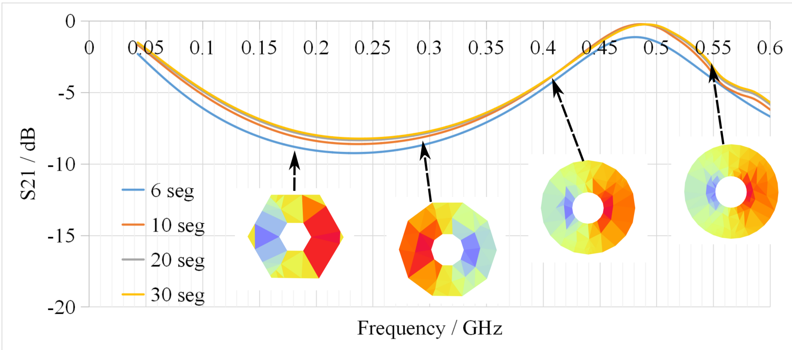

Figure 5.34 | Comparison of S_{21} for 6, 10, 20 and 30 segments of the cross section respectively

Fig.5.29 and 5.30 shows the S_{11} and S_{21} parameters with respect to different number of segments. The insets to both figures show the extracted mode profiles of the coaxial cable for each number of segments. It is found that the frequency of S_{11} at the resonance shows convergence for all cases. Although the magnitude of S_{11} at the resonance varies for different cases and there is about 15 dB drop between the 10-segment case and the 30-segment case, all of them are observed below 20 dB at the resonance hence are acceptable The S_{21} parameters are shown convergent above 10 segments for both frequency and magnitudes. Combining these observation and the computational expenses seen to the caption of Fig.5.29, It is suggested to use 10 segments to describe the coaxial probe as it provides both good accuracy and simulation efficiency.

5.3.5 T-junction model

The T-junction model is built by inserting a second wire on the middle of the first wire. There is however difficulties if direct merging of two wires is used when building the model. Fig. 5.35 shows the geometry output when one polygonal tube merged directly onto the limb of another polygonal tube. On the interface of two conductors, a sharp angle and curve edge are formed. This would increase meshing stress near the junction as very small meshes are required in order to discretise fine features. As a result, not only overall mesh amount increases, but also the time step needs to compromise to the size of the smallest tetrahedron. In order to overcome this, the

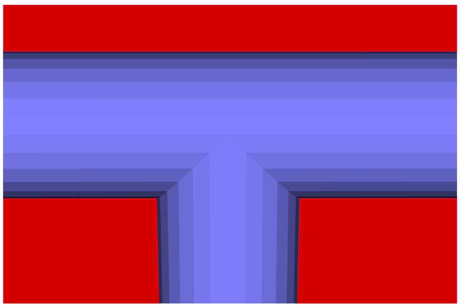

Figure 5.35 | Normal T-junction model with sharp angle and curve edges when two wires merged directly

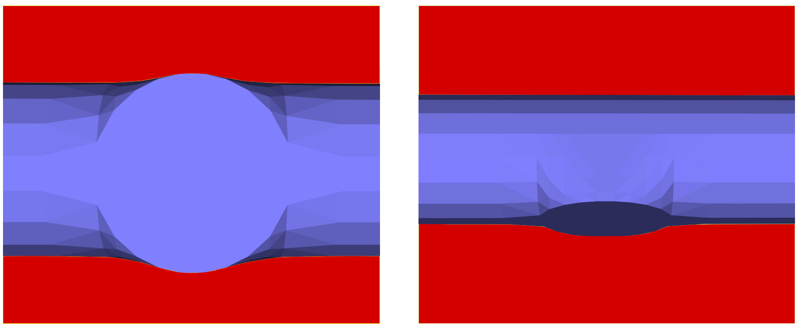

(a) (b)

Figure 5.36 | Stretched bottom face of the first wire for merging a second with a) bottom view, b) side view

cross-sections of the first wire, at the position where the second wire is merged, is modified to produce a flat circular bottom face toward the second wire as shown in Fig.5.36. The second wire is then extruded based upon the cross-section created from the first wire as shown in Fig.5.37. The end of the second wire is connected to the ground plane through another coaxial probe to enable consistent wire termination. In this simulation, the T-junction model is formed by two wires with the first wire

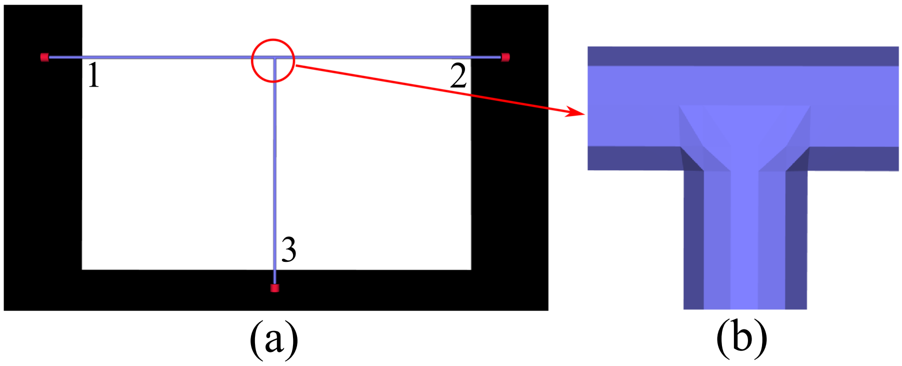

Figure 5.37 | Modified T-junction geometry with a) top view of the whole model, b) geometry details of the junction

of length 0.3m and the second wire of length 0.15m inserted to the middle of the first wire as shown in Fig.5.37. Both conductors are constructed by cross sections of 10 segments, which is demonstrated to provide adequate geometrical description by the previous subsection.

Based on guidelines obtained from the single wire model simulation, the model is meshed by a tetrahedral mesh of volume $1.5625 \times 10^{-5}m^3$ that corresponds to $\lambda/20$ at 600 MHz with localised mesh refinement in two regions centred each wire respectively, with a radius $R = 0.03m$ for each region and volume constraints $10^{-9}m^3$. Fig.5.38 shows the surface mesh of the T-junction model for both background and wire surface. It is highlighted that meshes at the junction area as shown in Fig.5.38 (b) are in similar scale to meshes around the wire section, therefore the approach used to construct the junction is acceptable. Fig.5.39a (a) shows more visually the mesh size distribution from the cross-sectional view of model, where a T-shape area is shown occupied by very fine meshes while remaining the out side region crudely meshed. This is supported by the mesh statistics shown in Fig.5.39a (b) which indicates a majority distribution of meshes in the volume range $3.26 \times 10^{-10}m^3$ to

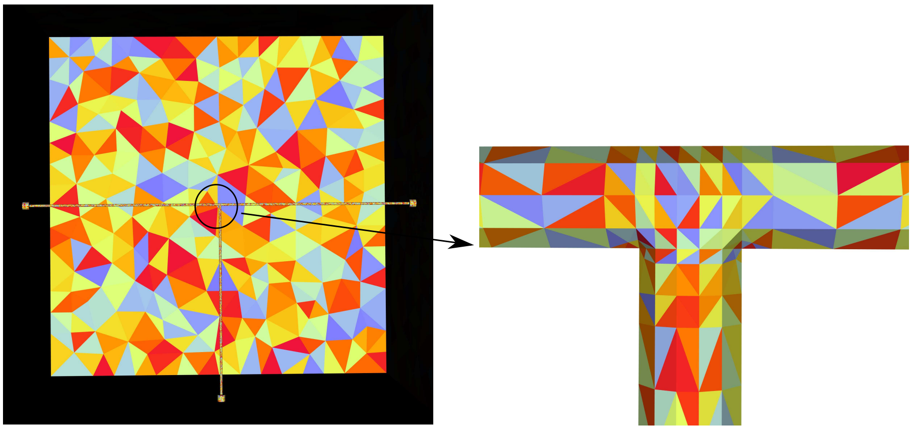

(a) (b)

Figure 5.38 | Mesh plot of the T-junction model with b) details around the junction for a $\lambda/20$ tetrahedral mesh and localised mesh refinement with $R = 0.03m$, $v = 10^{-9}m^3$

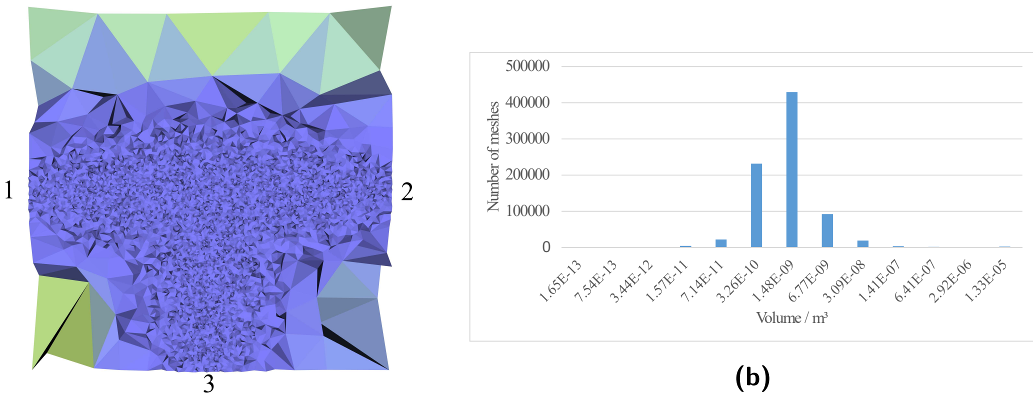

(a) (b)

Figure 5.39 | a) T-junction tetrahedral mesh plot in the cross-sectional plane with b) mesh size distribution as a function of cell volume

$6.77 \times 10^{-9}m^3$.

The model is excited from port 1 at the frequency of 400 MHz with a bandwidth from 100 MHz to 500 MHz. The S_{11}, S_{21} and S_{31} are extracted at three ports respectively, as labelled in Fig.5.37 (a). The simulated result in Fig5.40 shows the frequency response of wave propagation through the T-junction. Due to the presence of the junction, it is found that both resonant frequency and wave transmission are affected. First, two resonances for S_{11} S_{21} and S_{31} are found, one at about 520MHz and the other at about 550MHz. This can be explained by the cross coupling due

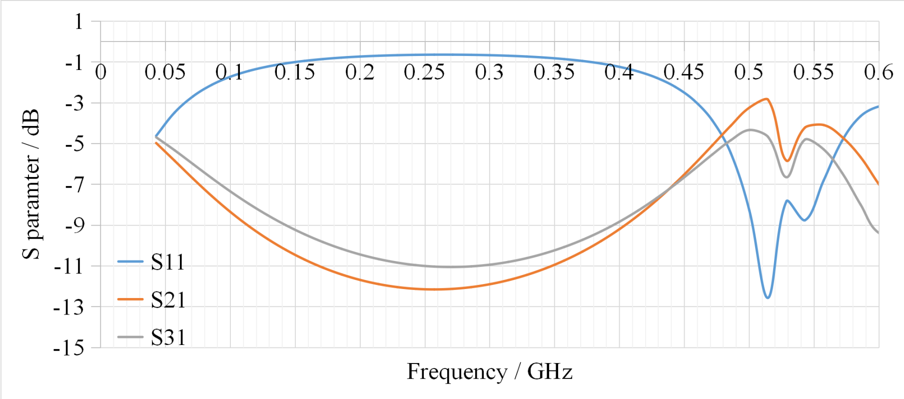

Figure 5.40 | S-parameters of the T-junction model

to the additional port presented in the middle of the first wire. Additionally, due to the unsymmetrical structure of the model with the first wire as the centre, a second resonance is presented. Secondly, both S_{21} and S_{31} show about 3dB to 5dB magnitude drop at the resonance. This is as expected due to the fact that the wave incident from port 1 split to two ports.

5.3.6 Cross-junction model evaluation

The construction of the crossed-junction model follows the same approach as the T-junction model, with another wire extruded on the other side of the main wire, as shown in Fig.5.41, with port numbers labelled in the figure. Each cable port is connected to a coaxial probe which then connects to the ground plane. The model has a length of 0.15m from each port to the junction, with radius 1mm for each limb. The cross-section of the wire is formed by a 10-segmented polygon, same as the T-junction model.

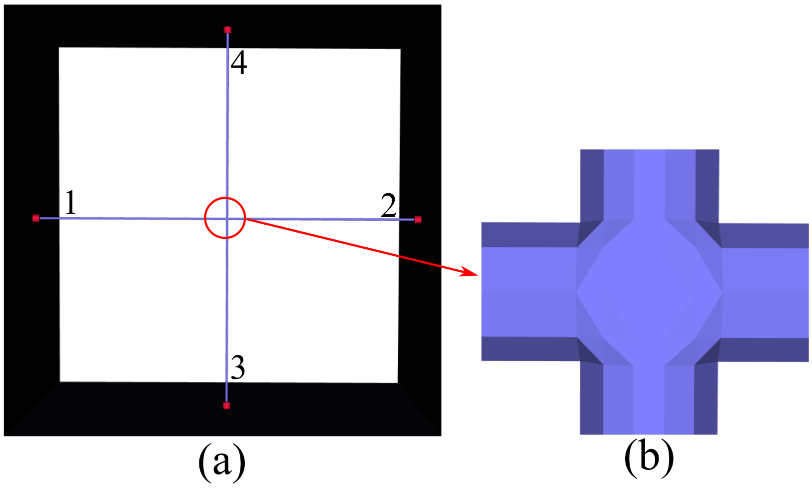

Figure 5.41 | Cross-junction model with a) top view of the whole model, b) geometry details of the junction

The meshing method adopted for the cross-junction model is a globally tetrahedral mesh of $\lambda/20$ at 600 MHz with a localised mesh refinement in a region radius $R = 0.03$ and target volume $v = 10^{-9}m^3$. Two refinement regions are used in order to cover four limbs.

The generated mesh output presented in Fig.5.42 show a relatively large size mesh in the background compared to meshes around the wire surface. This is supported by the mesh distribution in the cross-section plane of the model in Fig.5.43 (a) and the corresponding statistics as a function of cell volume. Due to the utilisa-

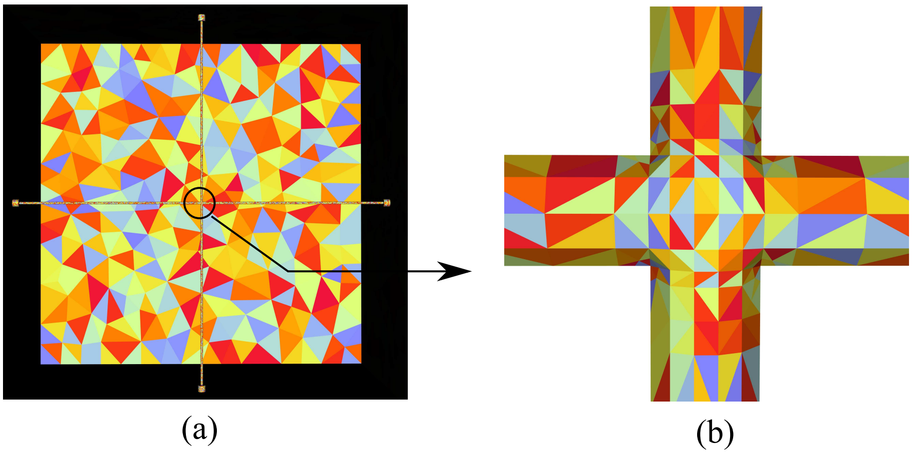

Figure 5.42 | Mesh plot of the cross-junction model with b) details around the junction for a $\lambda/20$ tetrahedral mesh and localised mesh refinement with $R = 0.03m$, $v = 10^{-9}m^3$

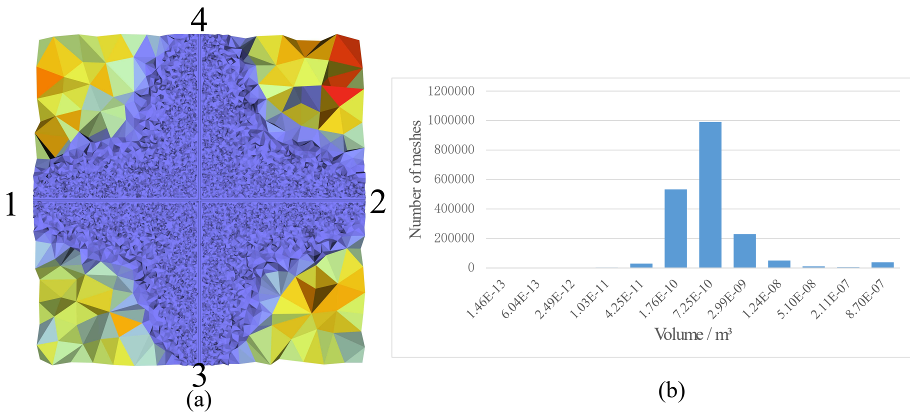

Figure 5.43 | a) Mesh plot of the cross-junction model in cross-sectional view and b) the volume distribution of mesh elements

tion of localised mesh refinement, a large number of meshes in the volume range $1.76 \times 10^{-10}m^3$ to $2.99 \times 10^{-9}m^3$ are generated and distributed around the junction limbs.

The simulated result in Fig.5.44 shows the wave transmission and reflection at four ports of the cross-junction. The effect of the junction is indicated by the frequency shift of the resonance from 500MHz for the single wire model to 580 MHz for the cross-junction model. Due to the symmetrical configuration of the model structure, only one resonance is found, compared to the T-junction model. The wave excited from port 1 is transmitted evenly to the other three ports. S-parameters close to

-6dB is observed at the resonance for all ports.

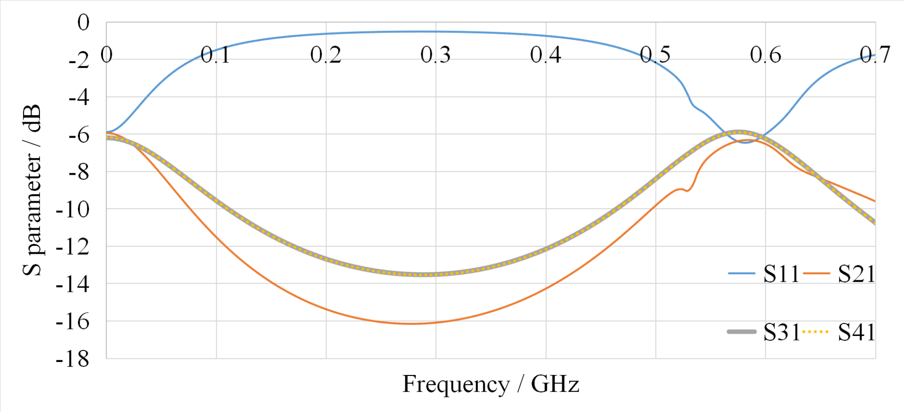

Figure 5.44 | S-parameters of the cross-junction model

5.4 Conclusion

This chapter has presented two simulation set-ups for canonical wiring problems and explored different meshing strategies and geometrical description. In the first section, a single wire model of length 0.5m is excited by a plane wave and the induced current is evaluated in the middle of the wire. The region around the wire is found finely meshed and the free space region is coarsely meshed. Decreasing meshing sizes in the free space increases resonant frequency from 240MHz for a coarse mesh to 263MHz for a $\lambda/100$ mesh. The rate of increase is found slowing down for mesh sizes less than $\lambda/50$. Due to the open-circuit termination of both ends of the wire, it is difficult for the model reaching a theoretical 300MHz at the resonance. The computational requirements however increases significantly for mesh sizes below $\lambda/50$ and is not desired. Faster frequency increase is observed when localised mesh refinement is applied around the wire region. It is found that refining mesh in the region $R = 0.02m$ with volume $v = 10^{-9}m^3$ and $R = 0.05m$ with volume $v = 10^{-8}m^3$ illustrates convergence of the resonant frequency at 270MHz but the latter shows 28% less time consumption and memory occupation. In terms of geometrical description, 6 and 10 segments of the wire cross section shows small effect on the resonant frequency compared to the 30 segments model but 10% less time consumption and 40% less memory cost. For different radii, both frequency and magnitude at the resonance drops as the radius increases. The resonant frequency shows slow decreasing rate for a radius less than 0.002λ and then decreases monotonically. The magnitude however reduces fast from 0.0005λ to 0.002λ and then slows down.

In the second section, the single wire model of length 0.3m is applied to modal excitation and observation. Similar findings are obtained for decreasing mesh sizes globally and locally. It is found that applying a global mesh size $\lambda/20$ and localised mesh refinement in the region $R = 0.02$ or $R = 0.03$ with volume target $v = 10^{-9}$, the resonant frequency reaches expected 500MHz for a 0.3m long wire. Decreasing number of segments of the cross section is found minor effect on the resonant frequency but reducing the computational expenses. The T-junction model and cross-junction model are also investigated based on obtained from the single wire model. The effect of the T-junction is found to shift the resonant frequency to 520MHz and 550MHz and split the wave from the excitation port to two ports. The cross-junction shifts the resonant frequency further to 580MHz and split the wave to three ports.

References

[5.1] C. A. Balanis, *Antenna Theory: Analysis and Design*, no. v. 1 in Antenna Theory: Analysis and Design (John Wiley & Sons, 2005).

[5.2] C. Christopoulos, *The Transmission-Line Modelling method:TLM* (Wiley-IEEE Press, 1995).

[5.3] C. Christopoulos, *The Transmission-Line Modeling (TLM) Method in Electromagnetics* (Morgan & Claypool, 2006).

6

Benchmarking problems simulation

This chapter presents a set of test cases to study the impact of coupling in cables due to external electromagnetic fields using the Unstructured Transmission Line modelling method (UTLM). Computational calculations of induced currents on wires are carried out for various cable bundle configurations with respect to simple structures. The analysis considers a set of test looms where the number of cores and spatial relationship are varied.

***

6.1 Introduction

Chapter (5) has presented the investigation of canonical single wire models and junctions. In this chapter, more complicated configurations of wire bundles based upon a relatively simple structure are investigated. The aim is to directly study the effect of external field coupling into wire bundles using UTLM method explicitly meshing the wire.

Similar to chapter (5), a single-core cable loom is first modelled in order to obtain sufficient meshing parameters. The core length in this chapter is extended and the cable loom is placed above a finite size metal board as the ground plane with metal bulkheads at two ends to terminate the wire. Such set-up has been widely used in literature due to its easy installation and feasibility [6.1–6.7]

The effect of spatial relationship between cores is then investigated on a two-core cable loom by varying spacings between two cores. The number of cores within the loom gradually increases in order to investigate the impact of such variation and resultant shielding effect. The analysis also considers the situation when cores separate along the route of the cable loom.

6.1.1 Plane wave excitation expression

The uniform plane wave excitation is applied in this chapter to model external coupling in cables of varying configurations. A general phasor form expression for the plane wavein the rectangular coordinate system can be written as [6.8]

$$\mathbf{E^{inc}} = E_0 \left[e_x \mathbf{n_x} + e_y \mathbf{n_y} + e_z \mathbf{n_z} \right] e^{-j\beta_x x} e^{-j\beta_y y} e^{-j\beta_y y} \tag{6.1}$$

where E_0 denotes the amplitude of the incident field, $e_x^2 + e_y^2 + e_z^2 = 1$ describes the electric field polarisation direction and $\beta = \omega\sqrt{\mu\varepsilon}$ defines the phase of the wave. A special case of plane wave excitation called broadside excitation is shown in Fig.

6.1. In this case

$$e_x = 0 \qquad \beta_x = \beta \tag{6.2}$$

$$e_y = 1 \qquad \beta_y = 0 \tag{6.3}$$

$$e_z = 0 \qquad \beta_z = 0 \tag{6.4}$$

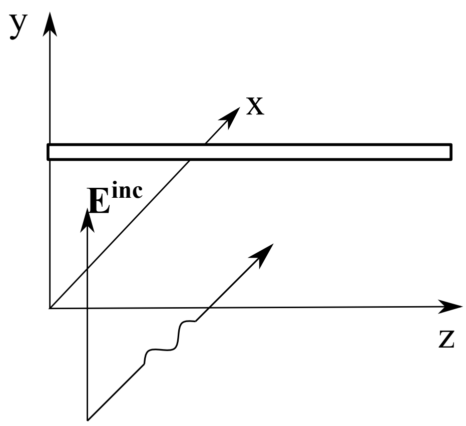

Figure 6.1 | Broadside plane wave excitation

6.2 One-core cable loom

This section presents simulations of a single-core cable loom above the ground plane. Sufficient simulation parameters, especially the meshing requirements are obtained for further simulations of more complicated cable models.

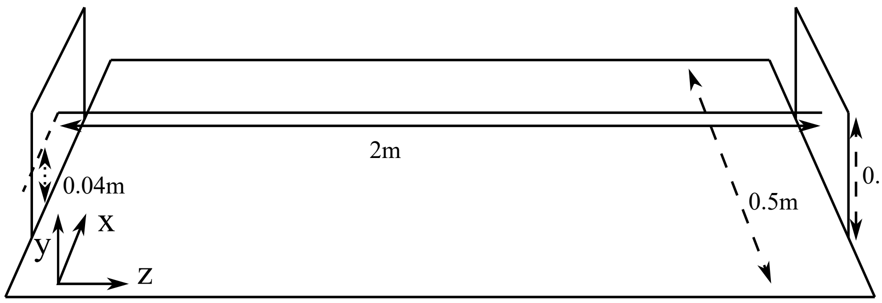

Figure 6.2 | Single wire model set-up in the computational space and

6.2.1 Problem description

Fig. 6.2 shows a one-core cable loom of length 2m and radius 1mm placed above a ground plane. The ends of the core are connected to a bulkhead that connects to the ground plane. The ground plane is 2m long and 0.5m wide and the bulkhead is 9cm high and 8cm wide. The cable is placed 4cm above the ground plane as shown in Fig. 6.2.

A plane wave electric field is excited from the broad side of the cable with its polarisation in the direction of $+y$ and propagating in the direction of $+x$ The induced current is observed at two ends of the cable by integrating surface magnetic fields around the core.

6.2.2 Meshing parameters evaluation - global mesh

Similar to chapter 5, the model is first investigated using global mesh discretisation. In this way a hybrid mesh is generated, with fine tetrahedral cells discretising the wire geometry and coarse Cartesian grids discretising the free space based on wavelength of interest. Due to the small radius of the wire compared to the wavelength of interest, very fine tetrahedral meshes are generated to discretise the wire surface, as shown in Fig. 6.3, whilst the free space region is discretised by 2.5 cm grids, which corresponds to $\lambda/20$ at 600 MHz.

The mesh statistics in Fig 6.4 shows clearly the variation of mesh sizes due to the presence of the wire. A significant number of meshes is shown in $10^{-6}m^3$ grade, which contributes to grids in the free space. Meanwhile, a large number of meshes is shown in $10^{-11}m^3$ and $10^{-10}m^3$ grades, which contribute to the discretisation of the wire surface and the region near the wire. There is also moderate number of meshes generated in middle grades as connection between fine and coarse meshes.

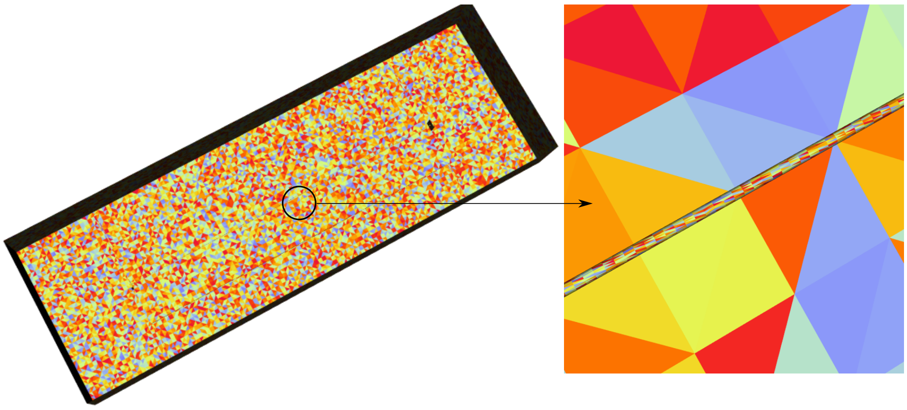

(a) (b)

Figure 6.3 | Mesh of one-core cable loom of cell size $\lambda/20$ with a) whole space, b) around wire surface

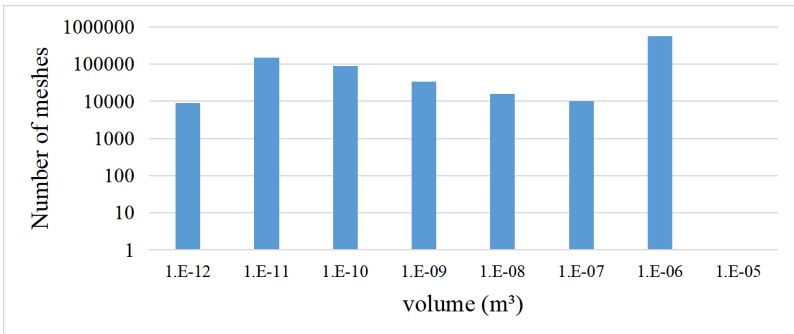

Figure 6.4 | Number of meshes in different mesh size range for $\lambda/20$ mesh

Descreasing global mesh size results in rapid increase of total mesh amount, especially in the coarse mesh grades as shown in Fig. 6.5. For a 1.67 cm mesh that corresponds to $\lambda/30$ and 1 cm mesh that corresponds to $\lambda/50$, significant increase of mesh amount is observed in $10^{-7}m^3$ grade. On the other hand, meshes below volume $10^{-9}m^3$ remain same amount level as the $\lambda/20$ mesh.

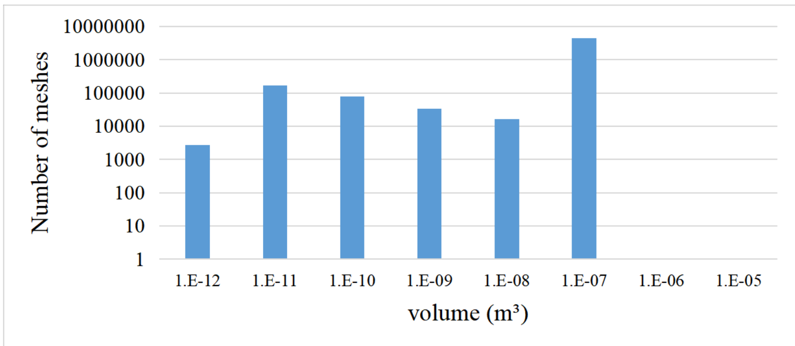

Figure 6.5 | Number of meshes in different mesh size range for $\lambda/30$ mesh

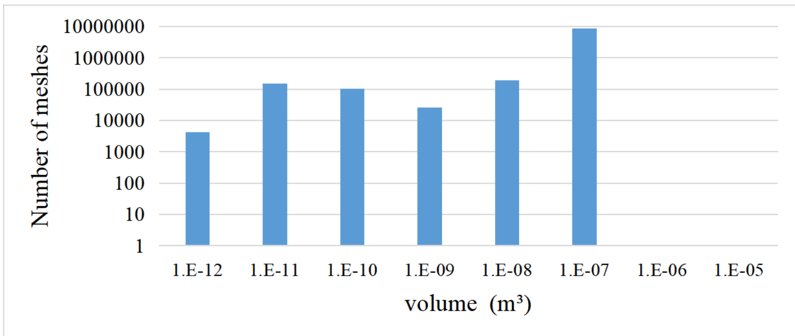

Figure 6.6 | Number of meshes in different mesh size range for $\lambda/50$ mesh

Figure 6.7 | Number of meshes as a function of cell volume for (a) $\lambda/30$ mesh, (b)$\lambda/50$ mesh

The simulation result of the induced current at the front end of the cable with varying mesh sizes is shown in Fig. 6.8. It is noted that all three cases show convergent result for the first resonance at 75 MHz, whose wavelength corresponds to double length of the cable. However at higher frequencies the resonances are not converging as the peak shifts with decreasing mesh size. Meanwhile, more simulation time and computation memory cost are required for a finer global mesh, as shown in table 6.1.

Table 6.1 | Computaional expenses for different global mesh sizes based on 4-core Xeon CPUs with 35 GB available RAM

	$\lambda/20$	$\lambda/30$	$\lambda/50$
Number of meshes	890549	4988650	9217750
Memory (MB)	2285	6135	10010
Simulation time (h)	29.20	70.88	99.48

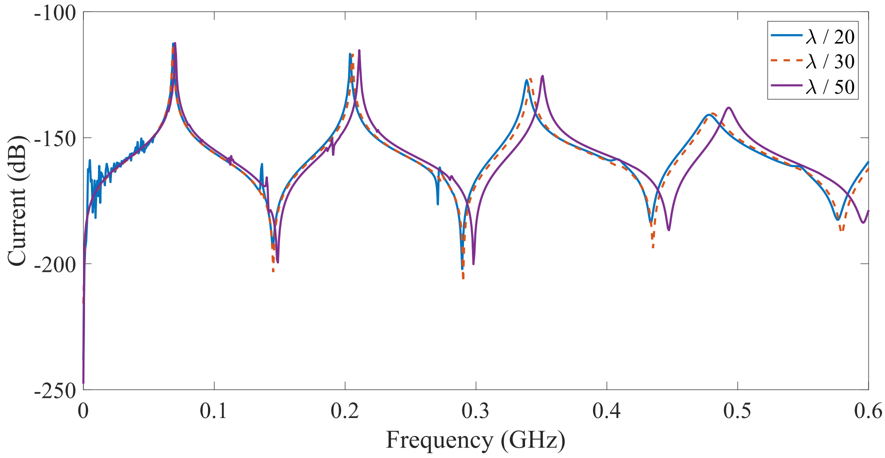

Figure 6.8 | Frequency response of the induced current at the front end of the cable with different global meshing sizes

One reason that causes the slow convergence of the result is the large difference of mesh sizes between cells in the free space region and near the wire region even $\lambda/50$ mesh is applied. Higher accuracy results would require further mesh refinment in order to achieve mesh uniformity. This is however limited by the resctricted computational resources as both simulation time and memory occupation rise rapidly. This brings up the strategy of using local mesh refinement in the subsequent section.

6.2.3 Meshing parameters evaluation - local mesh refinement

The local mesh refinement method is applied to the model in this section for two purposes. One is to reduce cell sizes in the near-field region around the wire. The other is to smooth connection between meshes in the near-field region and the free space region. As introduced in chapter 5, a cylindrical region with transverse radiu R and horizontal length l is introduced as shown in Fig. 6.9. In the refinement

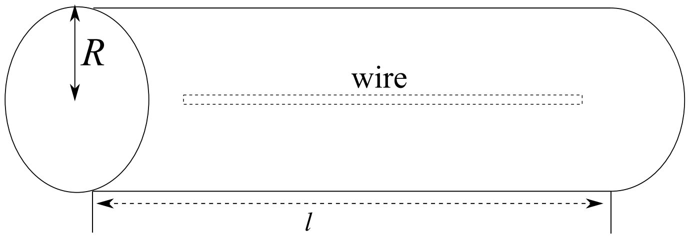

Figure 6.9 | Localised mesh refinement region definition

region, a minimum cell volume v is defined to restrict the cell size. The cell size grows gradually from centre outward and becomes similar to large cells outside the region. Table 6.2 lists four different ways of localised mesh refinement applied, with different region radii and cell volume limit. The background area is meshed by 2.5 cm cells, corresponding to $\lambda/20$ at 600 MHz. Based on the observation of mesh statistics in the above section, the refinement volume limit is set to be $10^{-8}m^3$ or $10^{-9}m^3$.

Table 6.2 | Localised mesh refinement parameters

	case 1	case 2	case 3	case 4
R (cm)	2	5	2	3
v (m^3)	10^{-8}	10^{-8}	10^{-9}	10^{-9}

An expansion of fine mesh area around the wire region is observed in the resultant cross-sectional view of the model in Fig. 6.10. Although Fig. 6.10 (b) and (d)

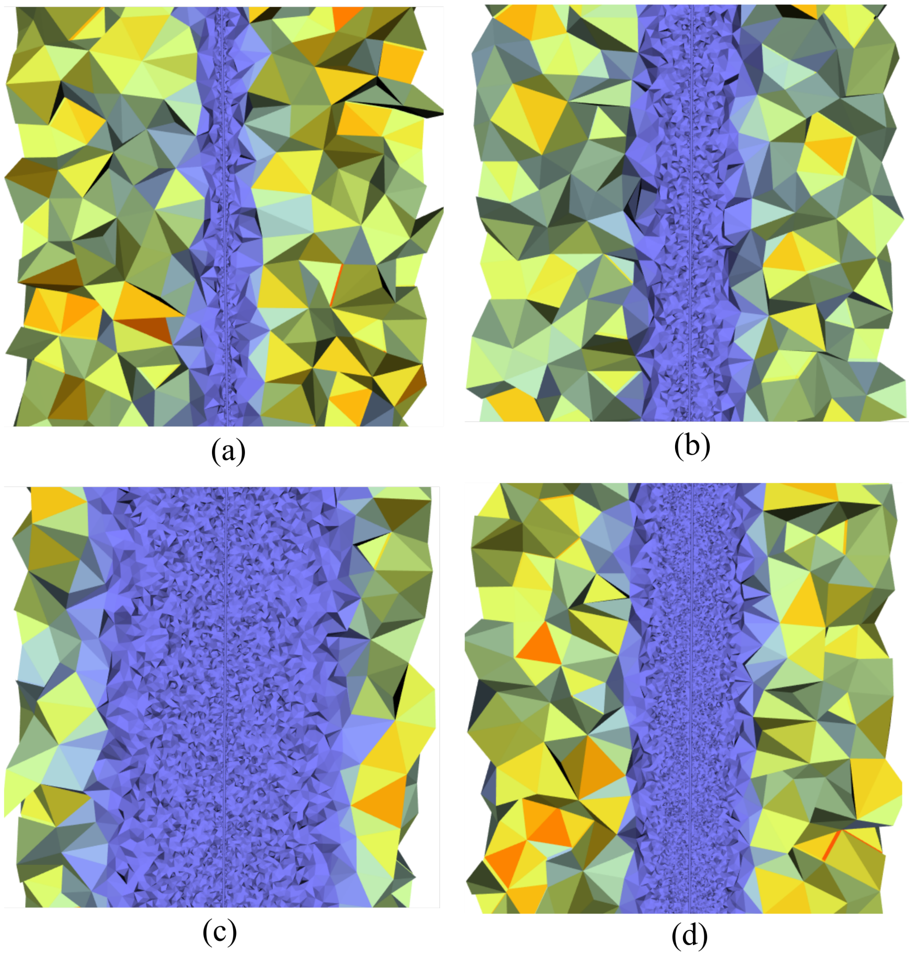

Figure 6.10 | Mesh cross-sectional view for a) without localised mesh refinement, b) case 1, c) case 2, d) case3

are set with same refinement radius, the latter shows a wider area of fine meshes due to its lower size limit. Fig. 6.10 (c) presents a larger buffer area and sees a smooth connection to the outside meshes. Fig. 6.11 reveals the change of mesh cell distribution with respect to their sizes. For the $10^{-8}m^3$ mesh, increasing amount of meshes in $10^{-9}m^3$ and $10^{-8}m^3$ grades is observed. When the volume limit is set to $10^{-9}m^3$, more meshes in $10^{-9}m^3$ and $10^{-10}m^3$ grades are generated.

The simulated current observation of cases listed in table 6.2 is shown in Fig. 6.12 and the corresponding computational expenses are listed in table 6.3. It indicates that by using local mesh refinement, a faster convergence of higher order resonances is obtained compared to cases without local mesh refinement shown in Fig.6.8. Ap-

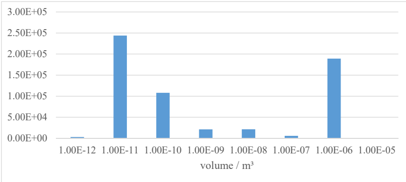

(a) No local refinement

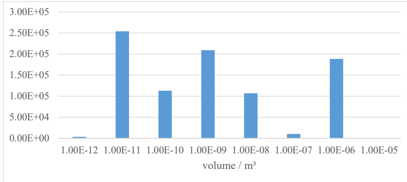

(b) case 1

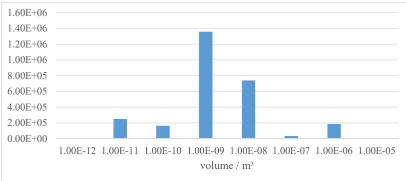

(c) case 2

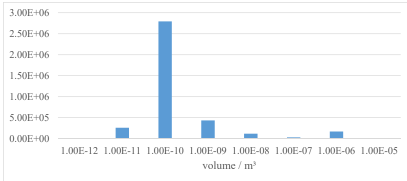

(d) case 3

Figure 6.11 | Mesh statistics as a function of cell volume for different localised mesh refinement parameters used compared to a) without localised mesh refinement

plying $10^{-8}m^3$ mesh refinement in the region 2 cm around the wire generates more convergent result with approximately half the simulation time and one third of the memory occupation compared to a $\lambda/50$ mesh applied in the previous section.

Further increasing the refinement region or applying finer volume limit would generate slightly better results but compromises much more for computational efficiency. Compare to the first mesh refinement case, it takes 2.23 times simulation time and 2.16 times memory usage for the same size limit applied in the region 5 cm around the wire. When a $10^{-9}m^3$ mesh limit is applied in the 2 cm region, 1.68 times more simulation time and 2.65 times more memory usage are required for the same test. Moreover, when $10^{-9}m^3$ mesh is applied in a 3 cm region around the wire, 5.6 times longer simulation and 6.3 times more memory are required compared to the first case. Therefore it is not efficient to apply more strict mesh refinement around the wire in order to achive complete convergence. However this technique is beneficial when applied to large electrical systems where wires are comparably thin.

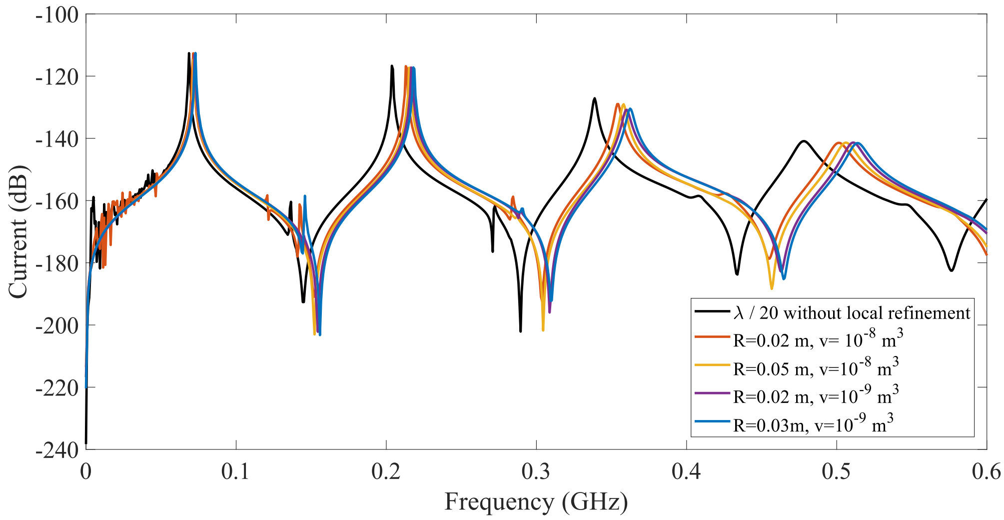

Figure 6.12 | Frequency response of the induced current at the front end of the cable with different local mesh refinement

Table 6.3 | Computaional expenses for different local mesh refinement parameters based on a 4-core Xeon 2.27 GHz CPU with 35 GB available RAM

R (cm)	2	5	2	3
v (m^3)	10^{-8}	10^{-8}	10^{-9}	10^{-9}
Number of meshes	885153	2730460	3810780	7989290
Memory (MB)	3036	6560	11079	22174
Simulation time (h)	49.25	109.92	132.14	324.68

6.3 One-core cable loom with wooden spacer

Previous section evaluates a one-core cable loom model above the ground plane and obtains sufficient meshing parameters for further simulations. However pratically, there is spacer presented to support the loom, such as a wooden board. The effect of the wooden board on the electromagnetic behaviour of the wire to the plane-wave excitation needs to be found out. Pratical wooden material has rather complicated electromagnetic properties due to its complicated composition. However for simplicity, in this thesis, the wood material is considered as a lossless dielectric medium with a real and constant dielectric constants.

Fig. 6.13 shows the geometry set-up of the same model in 6.2 with a wooden spacer placed beneath the loom. The spacer is 1.8 m long, 0.06 m wide and 0.02 m high. The wood material is set by a relative permittivity $\varepsilon_r = 4$ and relative permeability $\mu_r = 1$.

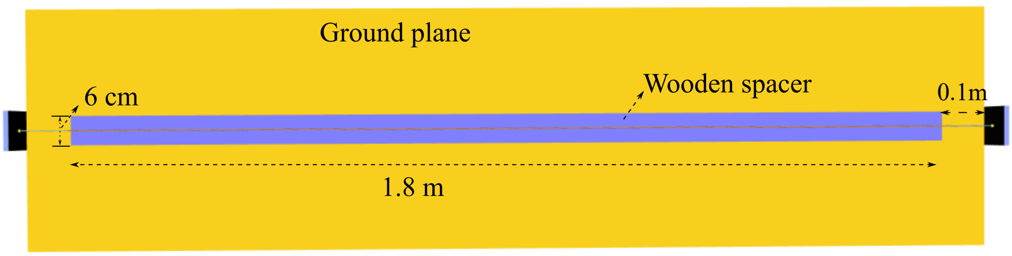

Figure 6.13 | One-core cable loom geometry above the ground plane with wooden spacer beneath the cable

The whole model is meshed by 2.5 cm grids, which correspond to $\lambda/20$ mesh at 600 MHz. Meanwhile local mesh refinement is applied in the region $R = 5$ cm around the wire with a cell volume limit $v = 10^{-8}m^3$. The meshed model is then investigated under the same plane wave excitation as the case without the wooden spacer.

Fig. 6.14 illustrates the effect of the wooden spacer on the currents induced on the wire. At the first resonance, the frequency of the model with wooden spacer is 4.2

MHz lower than the model without wooden spacer. And at higher order resonances, this difference of resonant frequencies between two models gets bigger. This holds true as the electric permittivity of the medium increases due to the wooden spacer beneath the wire, thereby reducing the wave velocity.

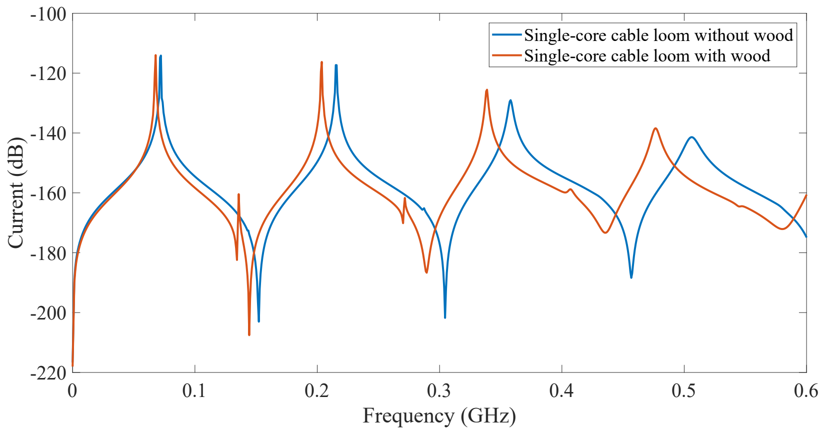

Figure 6.14 | Currents induced on the single-core wire loom with and without wooden spacer

6.4 Two-core cable loom

In this section, induced currents in two-core cable looms are modelled upon a plane wave excitation. This case evaluates the influence of separation distances between two wires on the coupling.

Fig. 6.15 shows the cross-sectional view of two-core cable looms with their cores placed $h = 4cm$ above the ground plane and core radius $r = 1mm$ respectively. The centre-to-centre spacing between two cores is denoted by s. Fig. 6.16 shows the constructed model geometry. The two cores are placed in parallel in the horizontal plane. Both ends of two cores are connected to the ground plane via bulkheads at each side and terminated by short circuit.

The meshing strategy used in the single core model is adopped here; that is $\lambda/20$ mesh size in the global space, with local mesh refinement of size $10^{-8}m^3$ applied in the 5 cm region centred on the middle point between two cores. Fig. 6.17 shows the meshed model and its cross-sectional view, which shows the growing mesh size from middle outwards. A plane wave with bandwidth of 1 MHz to 500 MHz is illuminated in the form of broadside excitation, with the electric field polarized in the $+x$ direction and propagating in the $-y$ direction. The induced current is observed at both ends of two wires.

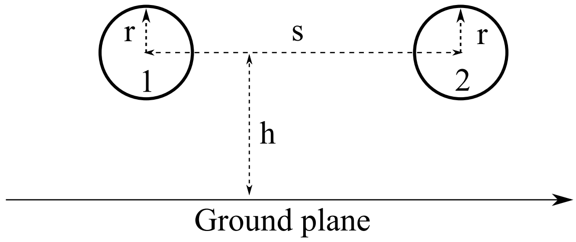

Figure 6.15 | The cross section of two core cable looms

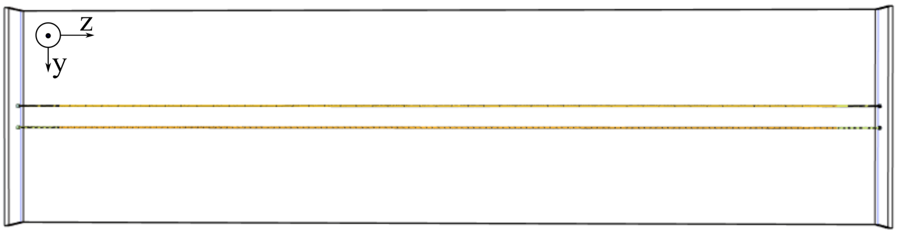

Figure 6.16 | Geometry of two core cable loom

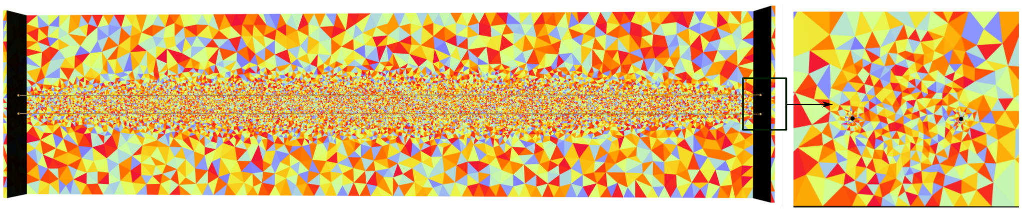

Figure 6.17 | Meshed two core cable loom model with global mesh size $\lambda/20$ and local mesh refinement $10^{-8}m^3$ in 5 cm region

In this section, a two-core cable loom model with their centre-to-centre spacing $s = 10r$ is first investigated. Fig. 6.18 shows the frequency response of induced currents in two wires and as a comparison, a single-core model that is placed in the middle position of two cores. The current induced in wire 1 is same as the current in wire 2 as the structure and positions of two wires are symmetric above the ground plane. It is observed that the resonant frequencies of currents induced in the two-core cable

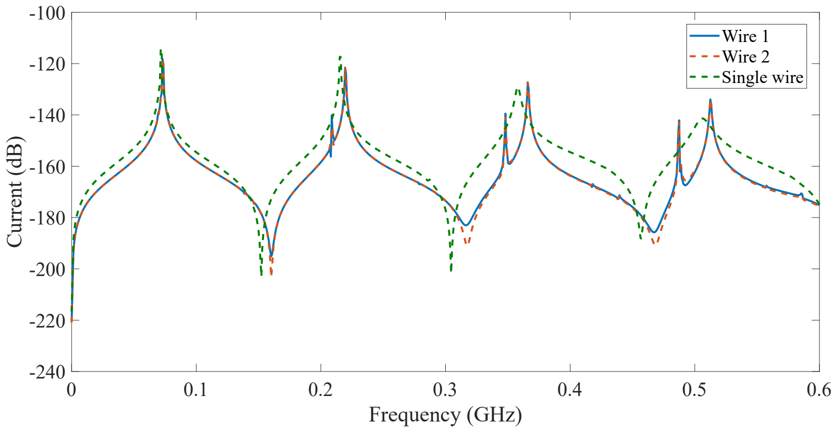

Figure 6.18 | Comparison of currents in two cores model with core spacing of 10r and the single core model

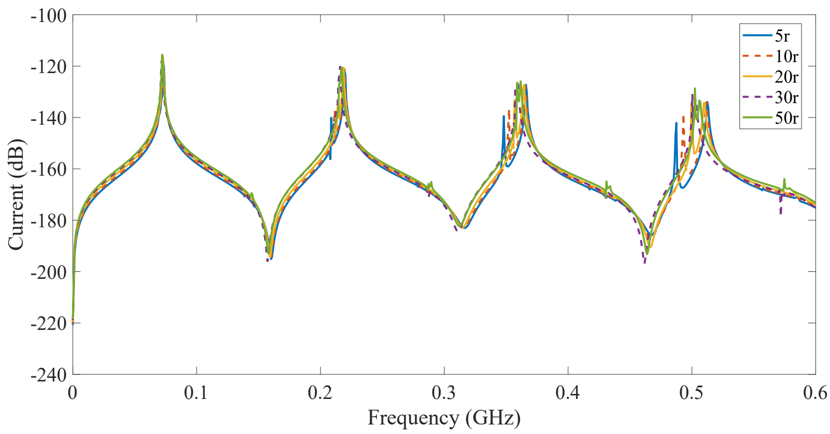

Figure 6.19 | Currents induced in two cores cable looms with core spacings as multiples of core radius

loom are split for the single core model at higher order resonances, and the degree of separation is seen growing as the frequency increases. This illustrates the occurance of cross coupling between two cores and its resultant secondary resonances. The secondary resonance is observed to locate at lower frequencies than the dominant resonance. The magnitude of currents at secondary resonances is smaller than the current at resonances due to the plane wave coupling, but it increases at higher order resonances. Besides, the magnitude of currents induced in two-core cable looms is slightly lower than current induced in the single-core model.

Fig. 6.19 compares currents s induced at the left end of wire 1 of two-core models with spacing between two cores increasing from $5r$ to $50r$. The result shows similar behaviour for the first resonance of all five models. Wider spacing between two cores shows narrower split of resonant frequencies but higher amplitude of currents at secondary resonances. This indicates the decreasing of coupling between two cores as the spacing between two cores increases. For models with $30r$ and $50r$ spacing between two cores, the coupling between two cores and its resultant resonances are negligible.

6.5 Y-shape two-core cable loom

This section models currents induced in Y-shape two-core cable looms upon plane wave excitations. As is common in practical electrical systems, wires and cable looms exhibite various routes along the platform to provide structure flexibility. A typical model is that one of the two parallel cables in the previous section separates in the middle along the route and forms a Y-shape junction. This case investigates the influence of the shape of the junction and changes of distances between two cores on the coupling of electromagnetic fields into each wire.

Fig. 6.20 shows the structure of a y-shape two-core model and its details at the junction. The axial length of the model is 2 m, with radius of both cores being r=1 mm. The spacings between two cores at two ends of the junction are denoted as s_1 and s_2 respectively. This case s_1 and s_2 are chosen $10r$ and $30r$ respectively. The transition length of the junction is denoted as d. Two cases of the connection length are modelled, one with $d = 6cm$ and the other with $d = 0cm$ which thereby forms a right angle separation.

The global space of the model is meshed by $\lambda/20$ cells where λ refers to the wave-length at 600 MHz. A cylindrical region of radius $R = 5$ cm that covers the whole model is defined for localised mesh refinement, with cell size limited by volume target

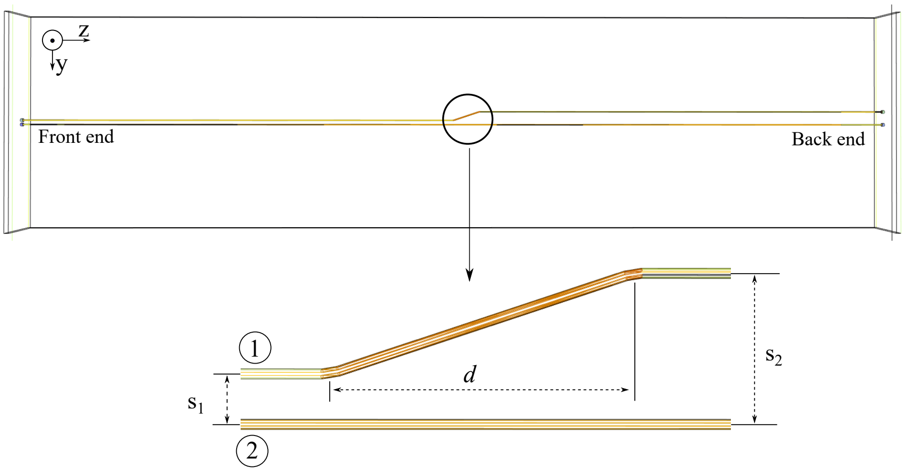

Figure 6.20 | Geometry of the Y-shape two core cable loom

$10^{-8}m^3$. Same plane wave excitation is applied into the model; that is with bandwidth 1 - 500 MHz, polarised in the direction $+x$ and propagating in the direction $-y$. Currents induced in four ends of the model is observed and plot.

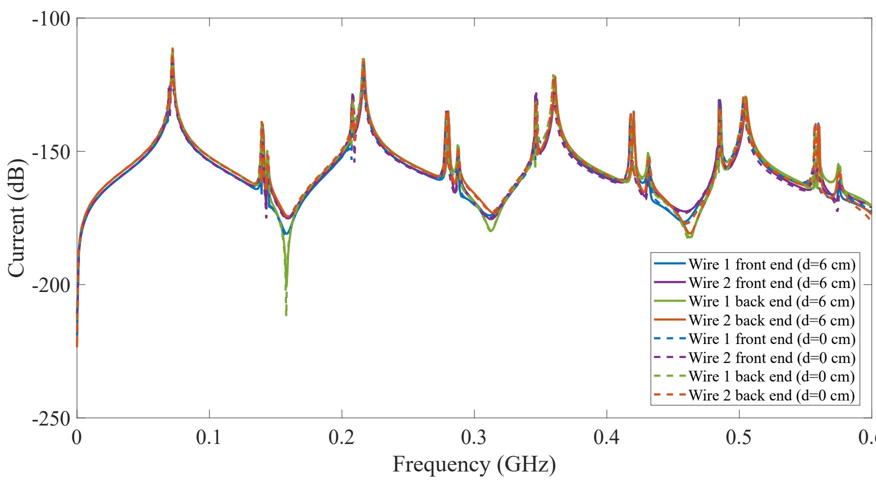

Figure 6.21 | Induced currents in four ends of Y-shape cable models of connection length d = 6 and 0 cm respectively

Fig. 6.21 shows currents induced in Y-shape cable models of two different connection lengths. Similar behaviour is observed for both models. It is therefore concluded that the change of transition length in the junction shows little influence on the induced current. Because the Y-shape cable model has $10r$ spacing before the junction and

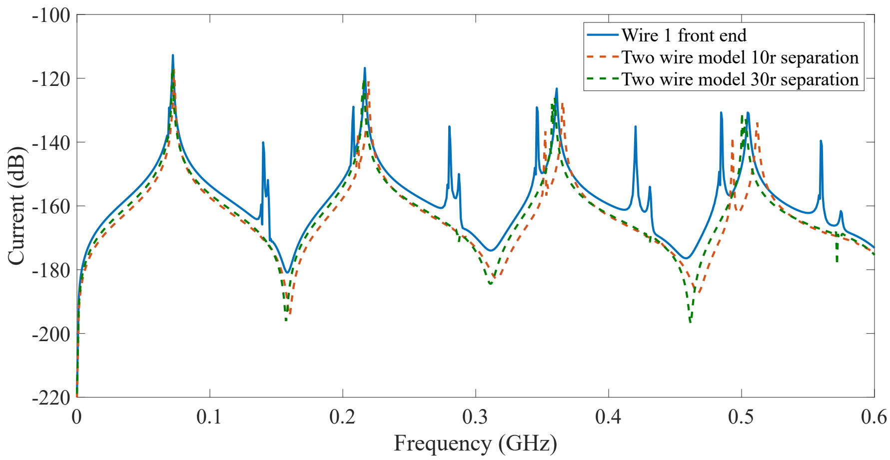

Figure 6.22 | Induced currents in the Y-shape two-core model compared to parallel cable model of 10r spacing and 30r spacing

$30r$ after, Fig. 6.22 compares the result of wire 1 with parallel two-core models with 10r and 30r spacings. Additional spikes at frequencies between original peaks are observed. This can be explained by the asymmetric strucutre of the model due to the change of spacing between two cores before and after the connection. Besides, the degree of split of resonant frequencies is shown similar to the parallel two-core model with $30r$ spacing.

6.6 Twisted-wire pair

In this section, induced currents in twisted-wire pair models are investigated upon a plane wave excitation. This case evaluates the effect of twisting on the coupling of external fields and between each other.

Fig. 6.23 shows the geometry of the twisted-wire pair model and details at the termination and near a complete twist. Similar to preceding cases, the front-to-back length of the model is 2 m and the radius of both cores is 1 mm. The centre-to-centre spacing between two cores is $1cm$. The twisting centre is $0.04m$ above the ground plane. The effect of twisting is evluated by exploring different number of twists in the model.

The model is meshed by $\lambda/20$ cells globally, and is further refined by $10^{-8}m^3$ volume target in the cylindrical region centred on the middle point between two cores with cross section radius $R = 5$cm. The incident field is a plane wave of frequency bandwidth 1- 500 MHz with field polarization in the $+x$ direction and propagating in the $-y$ direction. Induced currents are observed at both ends of two cores.

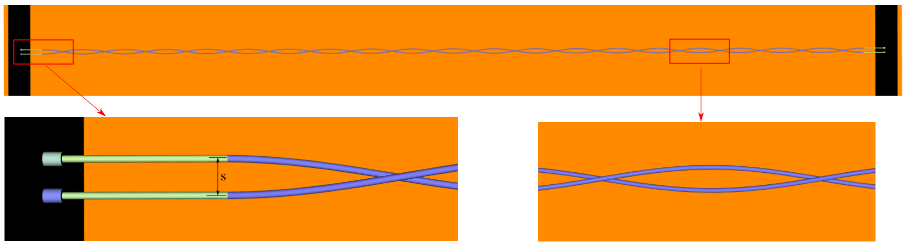

Figure 6.23 | Geometry of the twisted-wire pair model

Fig. 6.24 and 6.25 shows induced currents in twisted-wire pairs with 10 and 20 twists respectively. With increasing number of twists, it is obvious that the actual length of the wire increases, whilst the horizontal front-to-back length remains same. This explains the slight decreasing of resonant frequencies of the 20-twist model at higher order resonances compared to the 10-twist model and the non-twist model, as shown in Fig. 6.26. Additional spikes are observed between original resonances due to the variation of vertical height of cores due to twsiting.

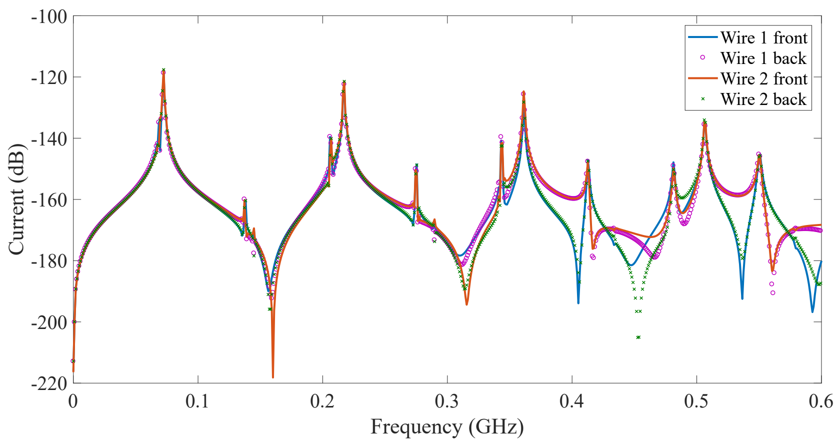

Figure 6.24 | Induced currents in twisted-wire pair model of 10 twists

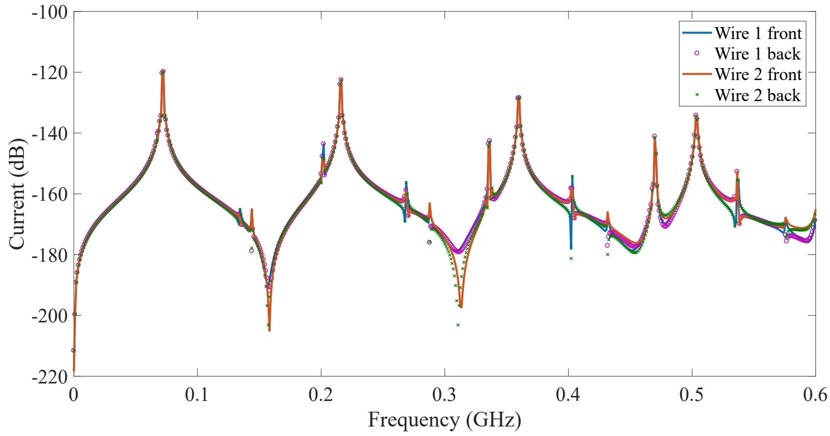

Figure 6.25 | Induced currents in twisted-wire pair model of 20 twists

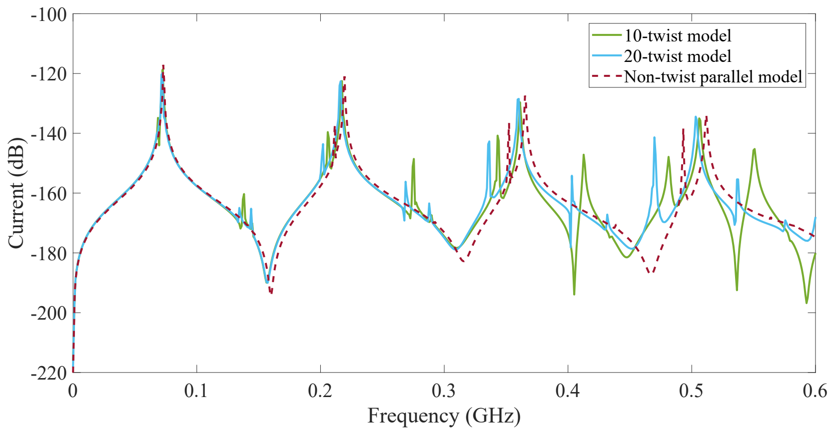

Figure 6.26 | Comparison of induced currents in twisted-wire pair models of different number of twists and parallel non-twist model

6.7 Four-wire separation

This section investigates the coupling of a four core cable loom to a plane wave excitation. This case explores the situation of a cable loom when close spaced cores separate apart along the route. The model geometry is shown in Fig. 6.27. The axial length of the cable loom is 2 m and the radius of four cores is 1 mm. The initial position of each core is shown in Fig. 6.28. Core 1 bends 5 cm in the $+y$ direction at 0.5 m point. Core 2 bends 2 cm in the $-y$ direction at 1 m point. Core 3 travels straightly along the route without any change. Core 4 bends 10 cm in the $-y$ direction at 1.5 m point.

Again, $\lambda/20$ mesh is applied in the global space and local mesh refinement of target volume $10^{-8}m^3$ is applied in regions that surrounding all cores. The tetrahedral mesh not only resolves issue when discretising fine wire features, but also shows good quality mesh when discretising the curve routes when the core route is deflected. The meshed model is simulated in a 4-core Sandy CPU platform with 35 GB available RAM.

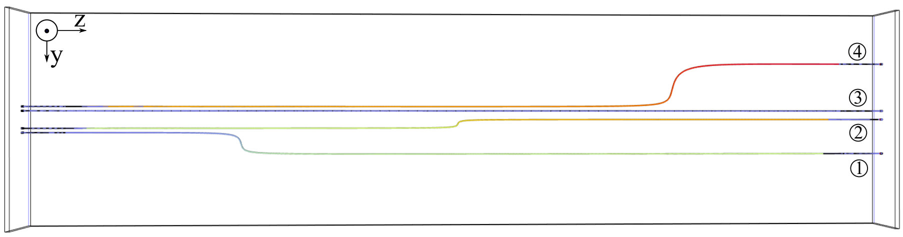

Figure 6.27 | Geometry of four cores cable loom

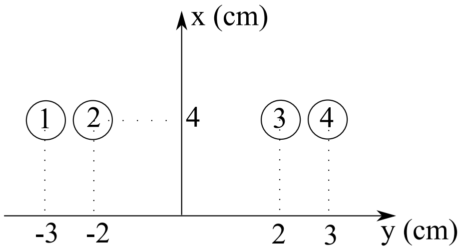

Figure 6.28 | Front cross section of the four cores cable loom

Fig. 6.29 shows the frequency response of induced currents in four wires of the loom respectively. The magnitude of currents in four cables are in generally similar level. Currents in back ends of cables show lower minima than current in front ends as a result of their wider separations. Increasing number of frequency splits are found at resonances due to additional mutual coupling between cores.

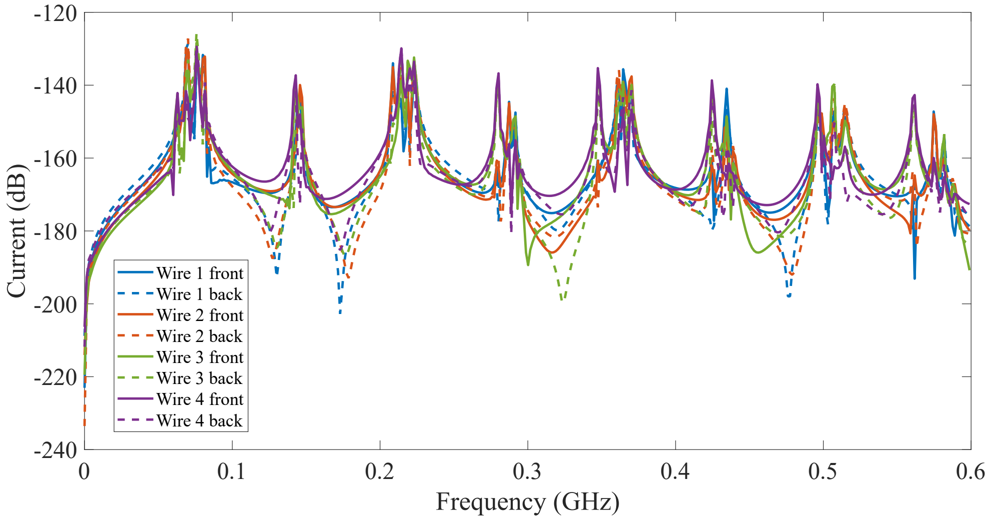

Figure 6.29 | Currents induced in two ends of four cables

6.8 Seven cores cable loom

In this section, the investigation of induced currents in seven cores cable looms upon plane wave excitations is presented. The cross section of seven cores in a cable loom is shown in Fig. 6.30. Six wires are placed evenly surrounding a seventh wire in the middle of the loom. The centre-to-centre spacing between neighbouring cores is denoted by s and the radius of cores is denoted by r.

The simulation set-up of the wire bundle is same as the one-core cable loom, as shown in Fig. 6.13, where both ends of cores connect to the ground plane via metal bulkheads and a wooden spacer is placed beneath the loom. The length of the cable loom is 2 m and the height of the loom centre above the ground plane is 4 cm. The wooden spacer placed to support the loom is 1.8 m long, 6 cm wide and 2 cm high with relative electric permittivity $\varepsilon_r = 4$.

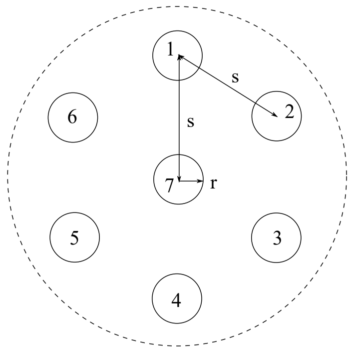

Figure 6.30 | Cross section of seven cores cable loom

Three sets of loom configurations are built and modelled in order to evaluate the effect of various core spacings within the loom and core radius on the electromagnetic coupling into cables. The model is meshed by $\lambda/20$ grids in the global space where λ correspond to the wavelength at 600 MHz. Meanwhile a cylindrical region centred on wire 7 with radius 5 cm is defined for localised mesh refinement with target cell volume $10^{-8}m^3$. A broadside plane wave of frequency band 1 - 500 MHz is illuminated with the field polarised in the $+x$ direction and propagating in the $-y$

direction.

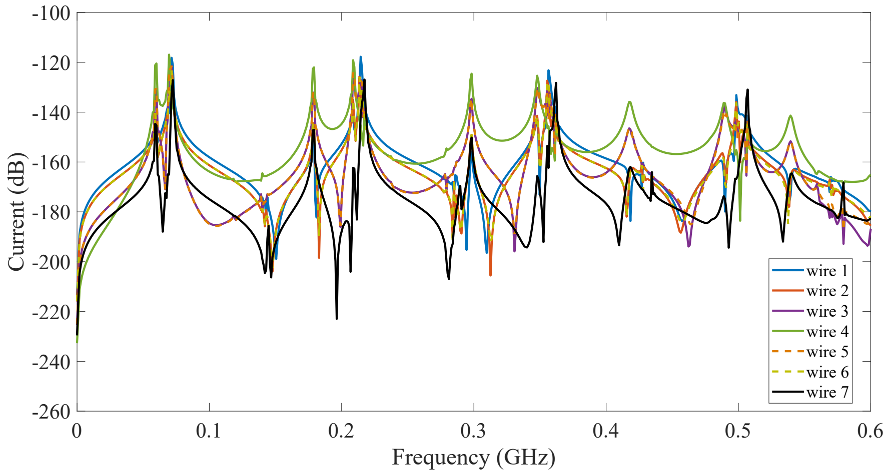

Figure 6.31 | Induced currents in the seven cores cable loom with core separation 1.5 cm and radius 1 mm

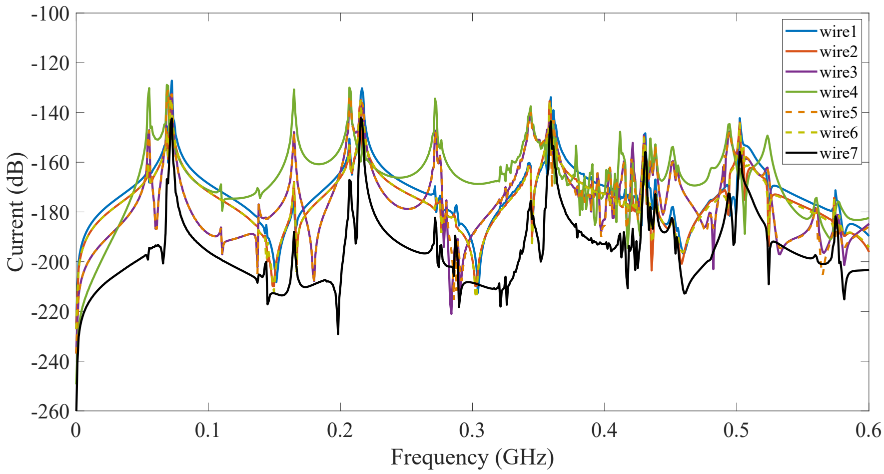

Figure 6.32 | Induced currents in the seven cores cable loom with core separation 1.5 cm and radius 3 mm

In the first model, the spacing between adjacent cores is set as $s = 1.5$ cm and the core radius is $r = 1$ mm. This presents a s/r ratio being 15. Currents induced at the end of cores are observed. Fig. 6.31 plots the frequency response of currents induced at the left end of seven cores respectively. The result shows resonances of incduced currents due to the plane wave coupling and coupling from other wires in the loom. The frequency at resonances due to cross coupling between neighbouring wires is shown slightly lower than that due to plane wave coupling and this difference

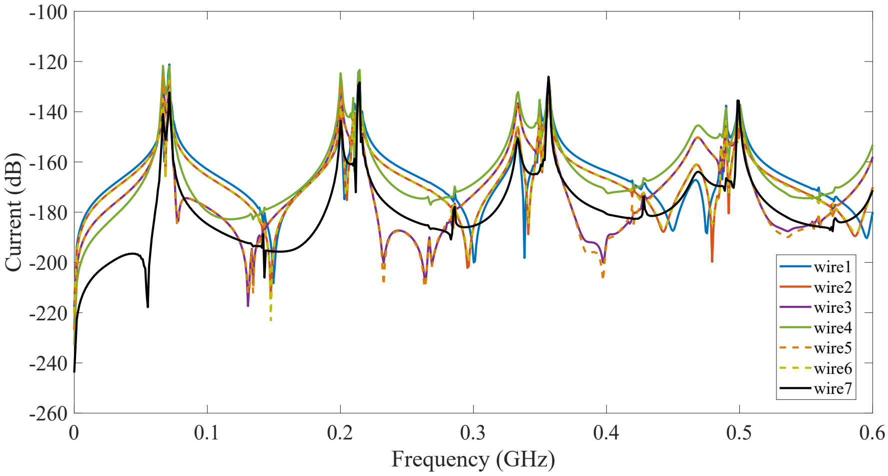

Figure 6.33 | Induced currents in the seven cores cable loom with core separation 0.5 cm and radius 1 mm

increases as frequency increases. It is also observed that the magnitude of currents in wire 1 and wire 4 due to the plane wave coupling are highest compared to other wires as they are less shielded toward the plane wave. Slight frequency shift at the resonance is observed due to their different heights.

The effect of height is more significant on currents due to cross coupling as wire 4 exhibits highest current than other wires. In contrast, current in wire 1 due to cross coupling is 20 dB lower than that in wire 4. Wire 2 has the same response as wire 6 and wire 3 has the same response as wire 5. Both these two cases show lower magnitudes of induced currents due to other wires than current induced in wire 4. The shieding effect is observed on wire 7 as it shows generally lower magnitude than other wires that surround it. The magnitude of the current in wire 7 due to plane wave coupling is 10 dB lower than the current in wire 1. However they show similar current level due to cross coupling between neighbouring wires.

In the second configuration, the spacing between cores remains $1.5cm$ while the radius of cores is set to 3 mm. This presents a s/r ratio being 5. Fig. 6.32 shows the induced currents at the left end of seven cores respectively. Similar behaviour is observed while wire 4 shows more distortion induced at higher frequencies. This is due to its conducting surface reaching closer to the wooden spacer. It can be seen that the effect of shielding from surrounding wires is more significant on currents induced in wire 7. The magnitude of the current in wire 7 due to plane wave coupling is shown 15 dB lower than the current induced in wire 1. Meanwhile, less currents is induced in wire 7 due to cross coupling from other wires than the first configuration.

In the last configuration, the radius of cores is kept the same as the first configuration while the distance between adjacent core centres is changed to 0.5 cm. This gives a s/r ratio being same as the second configuration. Fig. 6.33 shows the resultant currents in seven wires respectively. The magnitude of the current in wire 7 is about 10 dB lower than that in wire 1 for the plane wave coupling and 20 dB lower than that in wire 4 for the cross coupling. On the other hand, the difference of resonant frequencies between two types of coupling is reduced, due to their closer spacing. Compared to the second configuration which has the s/r ratio, the former shows less distortions due to the larger spacing between the wire bundle and the wooden spacer.

6.9 Single core wire bundle variational analysis

This section and following sections extend the length of wire bundle from 2 m to 8 m to explore more features at higher frequencies. The impact of the position of a single core within in the wire bundle on the plane wave coupling is investigated. The geometrical configuration of the model is similar to section 6.2, as shown in Fig. 6.34. The wire bunlde has a virtual radius of R=2 cm and is placed on the top of the wooden spacer that is 2 cm high. The radius of the core is 1 mm. Both ends of the bundle are connected to the metal bulkhead by short circuit termination. The position of the single core varies inside the wire bundle as shown in Fig. 6.35. Fig.

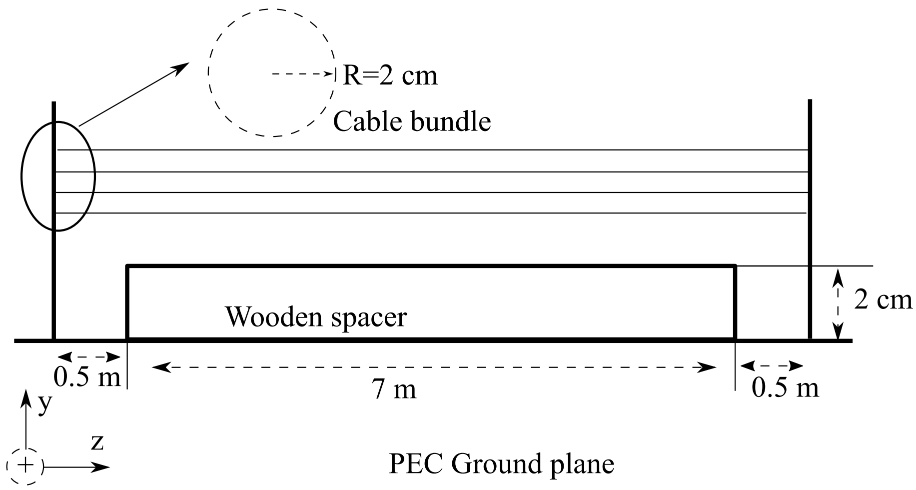

Figure 6.34 | Wire bundle geometrical set up above a ground plane

6.35 (a) is the wire bundle with its core at the centre of the bunle. Fig. 6.35 (b) places the core R/2 above the bundle centre. Fig. 6.35 (c) moves the core in bundle 2 R/2 right. Fig. 6.35 (d) moves the core in bundle 1 R/2 right. Fig. 6.35 (e) moves the core in bundle 4 R/2 down. Fig. 6.35 (f) moves the core in bundle 1 R/2 down.

The geometry is meshed by $10^{-5}m^3$ tetrahedral mesh that corresponds to $\lambda/30$ mesh at 400 MHz, which is sufficiently small for result convergence as stated in section 6.2. A broadside plane wave of frequency 1 - 400 MHz is excited with field polarisation in the $+y$ direction and propagating in the $-x$ direction.

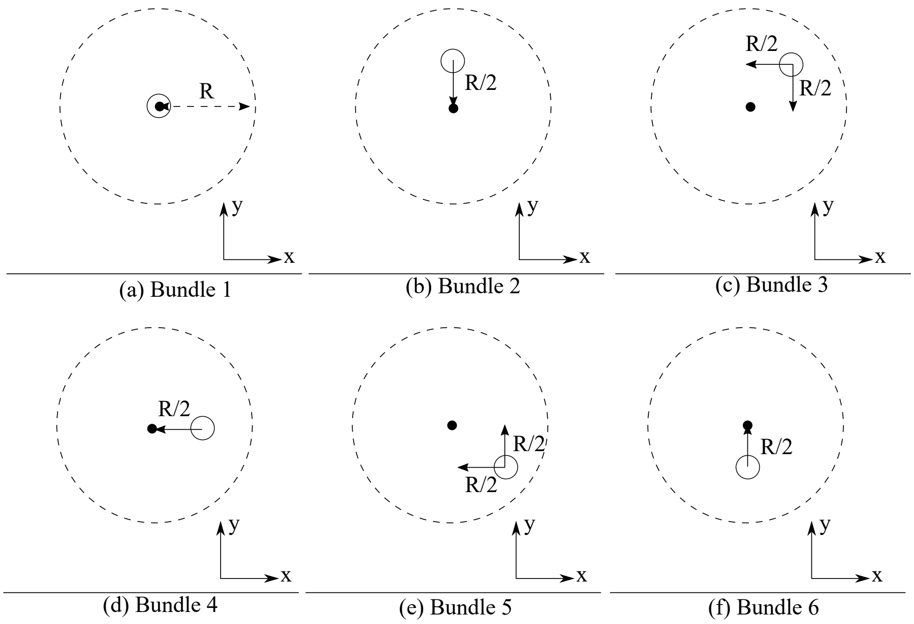

Figure 6.35 | Cross section of six single core wire bundle configurations

The currents induced in six wire bundles are shown in Fig. 6.36 respectively. It can be seen that the vertical position of the single core within the bundle affects the resonant frequencies of currents in the wire but the horizontal position has little effect. Bundle 5 and 6 show lowest resonant frequencies while bundle 2 and 3 show highest frequencies. A further investigation of bundle 2 and 6 without the wooden spacer in Fig. 6.37 explains the shift of reosonant frequencies of the induced current. It can be seen that when the wooden spacer is removed between the bundle and the ground plane hence presenting a homogeneous medium, the shift in resonant frequencies due to the vertical position is eliminated.

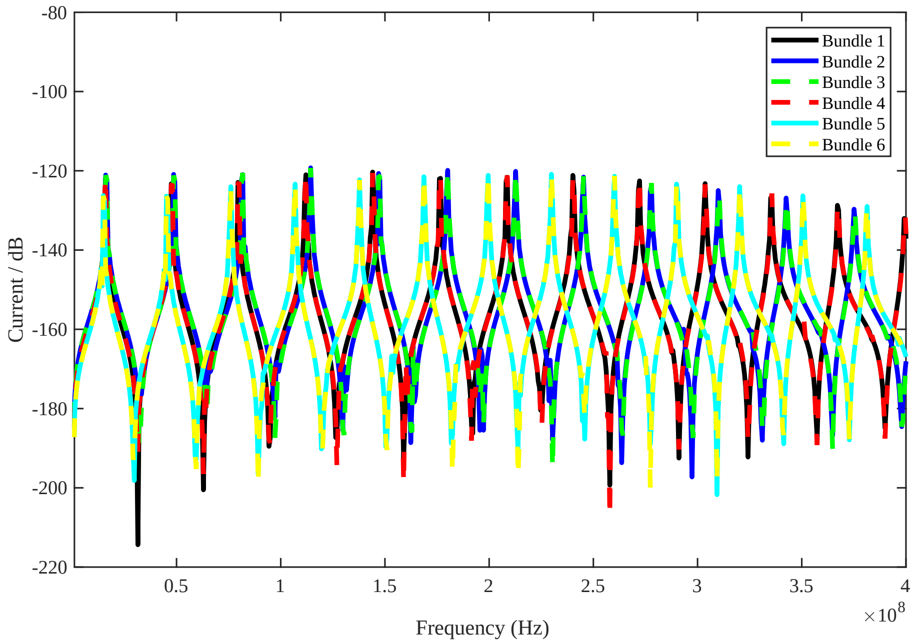

Figure 6.36 | Induced currents in the single core wire bundle of different position

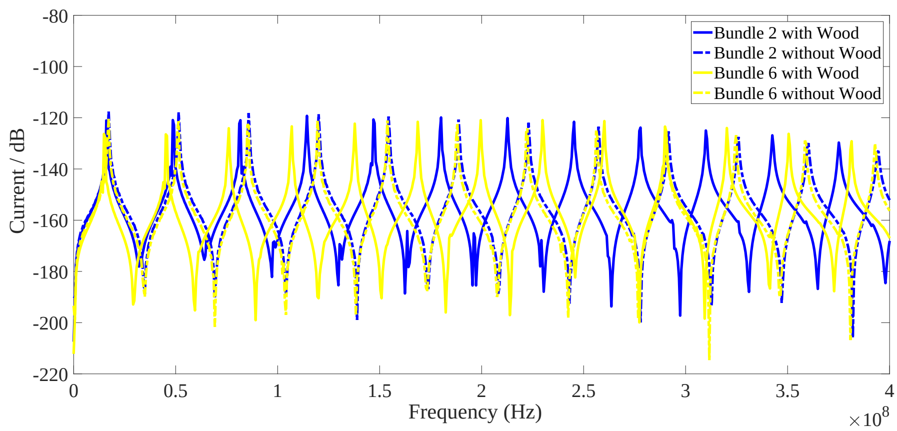

Figure 6.37 | Comparison of currents induced in bundle 2 and 6 with and without the wooden spacer

6.10 Three cores wire bundle variational analysis

This section presents the investigation of induced currents in three cores wire bundles upon plane wave excitations. Fig. 6.38 shows four different configurations of three wires within the bundle. In Fig. 6.38 (a) wire 1 is placed in the centre of the bundle, while wire 2 and wire 3 placed on the right top and right bottom of wire1 with a separation distance R = 1 cm from wire 1. Fig. 6.38 (b), (c) and (d) are cross sections of bundle 2, 3 and 4, formed by bundle 1 rotated by 45°, 90° and 135° respectively.

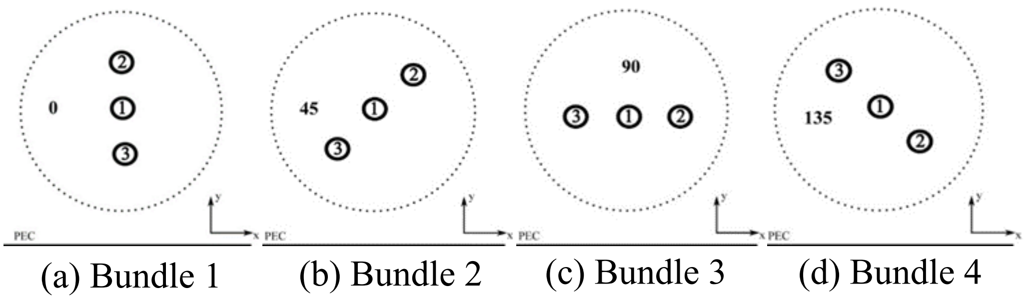

Figure 6.38 | The cross section of three cores wire bundles of diffenrent wire positions

The model is meshed and excited in the same way as section 6.9. The induced currents in all three wires in the bundle upon the plane wave excitation are evaluated. Fig. 6.39 shows currents induced at the left end of three wires respectively. It can be seen that three wires show similar behaviour of frequency response, but the magnitude of currents in the centre wire is relatively lower than the other two wires. The effect of shielding on the centre wire is more clearly demonstrated in Fig. 6.40, where the current induced in the centre wire of bundle 1 is compared to the single core wire bundle 1 in Fig. 6.35 (a). These two models are in the same position in the wire bundle but the second model is surrounded by two other wires. There are about 15 dB difference of the magnitude of currents at the resonance between the single core model and the three cores model. Meanwhile, due to the cross coupling between neighbouring wires, the resonant frequencies in the current of three core bundle 1 wire 1 are split.

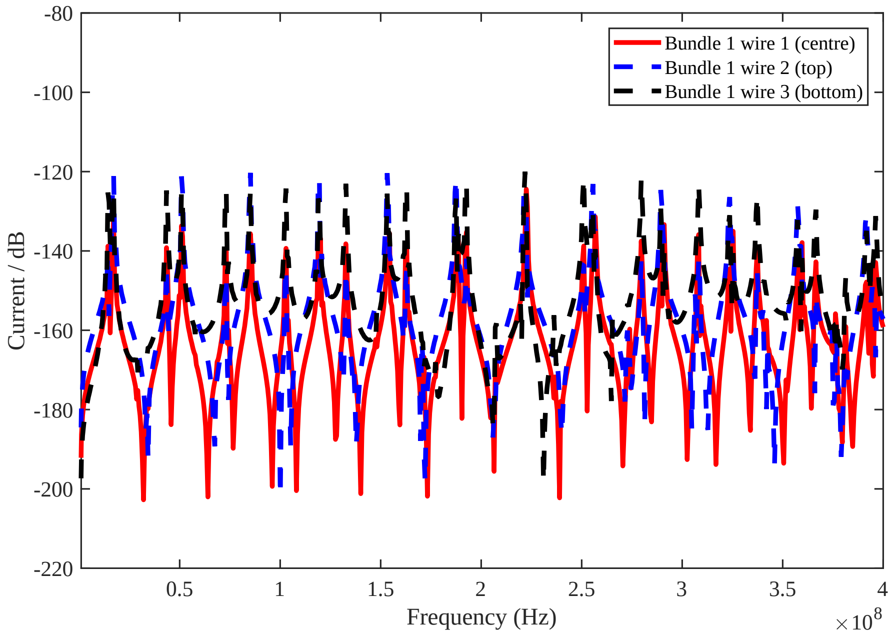

Figure 6.39 | Induced currents in the three cores wire bundle 1

In order to analysis generally the effect of positions of three cores on the wire coupling, it is more clear to calculate the maximum, average and minimum currents in the three cores wire bundle. Fig. 6.41 shows the maximum, average and minimum current of the three cores wire bundle 1 in Fig. 6.38 (a). Such results are then processed to bundle 2, 3 and 4 in Fig. 6.38 (b), (c) and (d) respectively. Fig. 6.42 shows the maximum current in four sets of three cores wire bundles. It can be seen that the position of cores affect the resonant frequencies of maximum currents in wire bundles. It is also noted that in bundle 3 as shown in Fig. 6.38 (c) where three wires in the bundle are placed at the same height, three is no split of resonant frequencies of maximum current in the bundle. Same behaviour is also obeserved in the plot for average and minimum current responses in Fig. 6.43 and 6.44. It is however noted that wire bundle 3 shows slightly higher magnitude of minimum currents in three cores wire bundles.

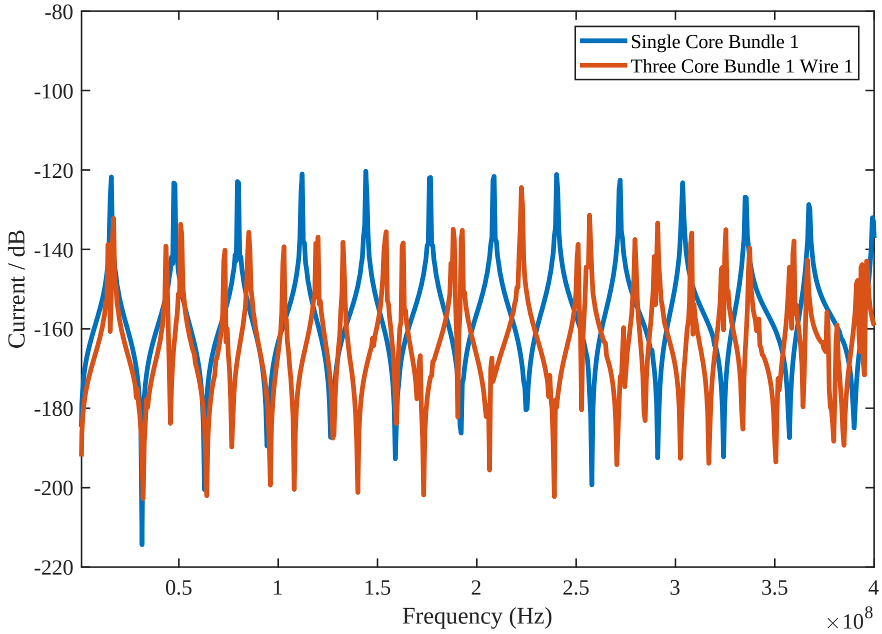

Figure 6.40 | Induced currents in the single core wire bundle 1 in Fig. 6.35 (a) and three core wire bundle 1 wire1 (centre)

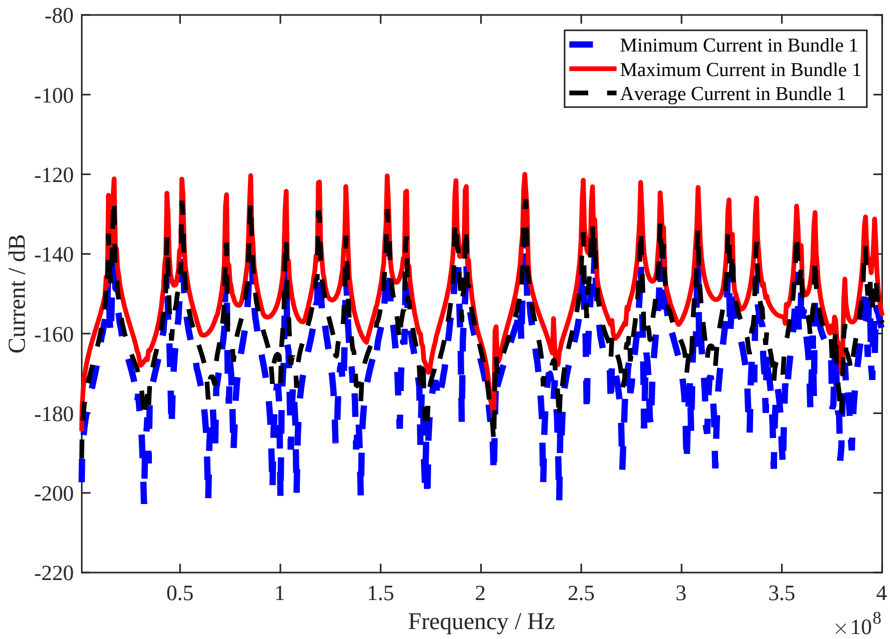

Figure 6.41 | Maximum, average and minimum currents at the left end of three cores wire bundle 1 as shown in Fig. 6.38 (a)

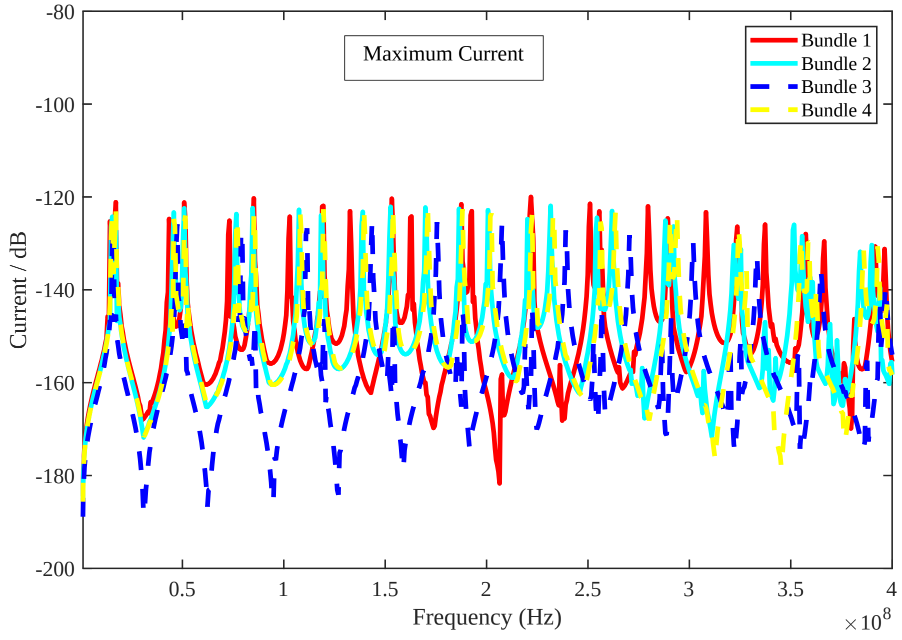

Figure 6.42 | Maximum currents at the left end of four sets of three cores wire bundles as shown in Fig. 6.38

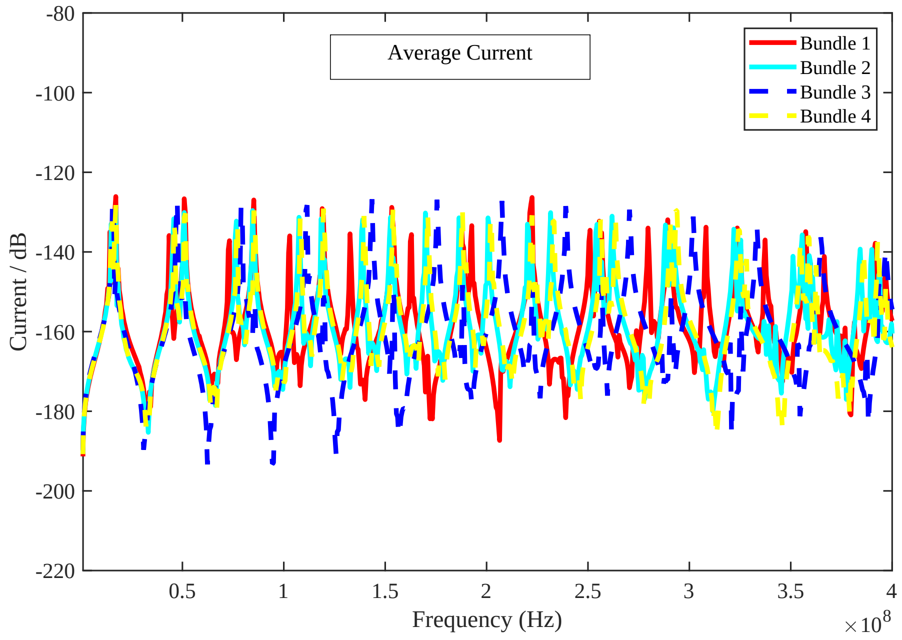

Figure 6.43 | Average currents at the left end of four sets of three cores wire bundles as shown in Fig. 6.38

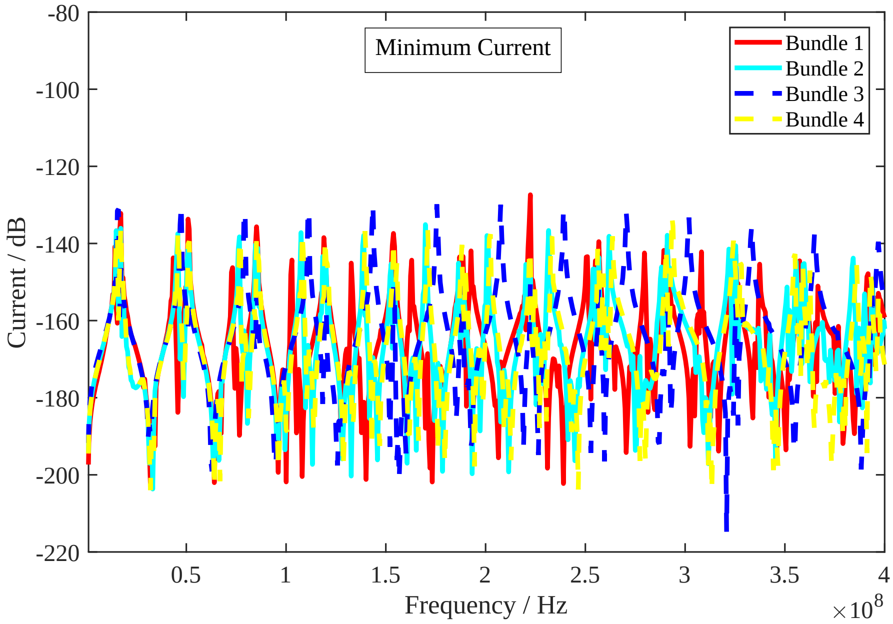

Figure 6.44 | Minumum currents at the left end of four sets of three cores wire bundles as shown in Fig. 6.38

6.11 Ten cores wire bundles variational analysis

The purpose of this section is to model and investigate currents induced in ten cores wire bundles upon plane wave excitations. It needs to be mentioned that when there are many cores in a wire bundle, it is more efficient to evaluate the maximum, average and minimum current induced in the bundle than evaluating currents in each single core.

Fig. 6.45 shows the cross section of ten sets of 10 core wire bundles to be evaluated. Wire bundle 1 in Fig. 6.45 (a) consist of 10 cores placed symmetrically in the bundle. Each core has radius 1 mm and adjacent cores are set equally spaced by 7 mm. Wire bundle 2, 3, 4 and 5 are then obtained by rotating bundle 1 by 45°, 90°, 135° and 180° respectively, as shown in Fig. 6.45 (b), (c), (d) and (e). Cores in Wire bundle 6 in Fig. 6.45 (f) are however placed more randomly. Table 6.4 lists the cross-sectional coordinates of all 10 cores in the bundle 6. Wire bundle 7, 8, 9 and 10 are then obtained by rotating bundle 6 by 45°, 90°, 135° and 180° respectively, as shown in Fig. 6.45 (g), (h), (i) and (j). Fig. 6.46, 6.47 and 6.48 show

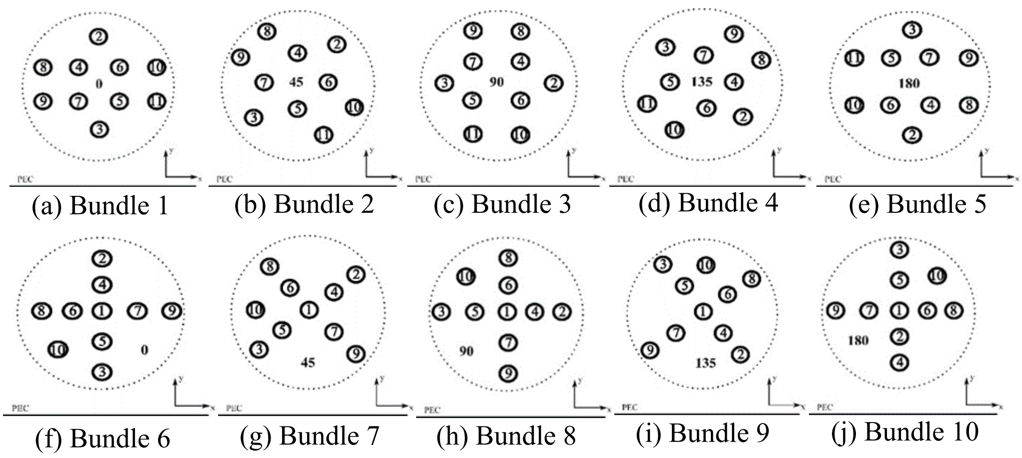

Figure 6.45 | The cross section of ten cores wire bundles of diffenrent wire positions

the maximum, average and minimum current induced at the left end of ten cores wire bundles respectively. It is observed that the resonant frequencies for maximum, average and minimum currents change with different wire positions in the bundle, especially at higher frequencies. Besides, there are approximately 10 dB differences between the magnitude of maximum and minimum currents.

Table 6.4 | Cross-sectional coordinate of 10 cores of wire bundle 6 in Fig. 6.45 (f)

Coordinates	Wire 1	Wire 2	Wire 3	Wire 4	Wire 5	Wire 6	Wire 7	Wire 8	Wire 9	Wire 10
X (cm)	0	0	0	0	0	-0.5	0.6	-1.0	1.2	-0.8
Y(cm)	0	1.0	-1.2	0.5	0.6	0	0	0	0	-0.8

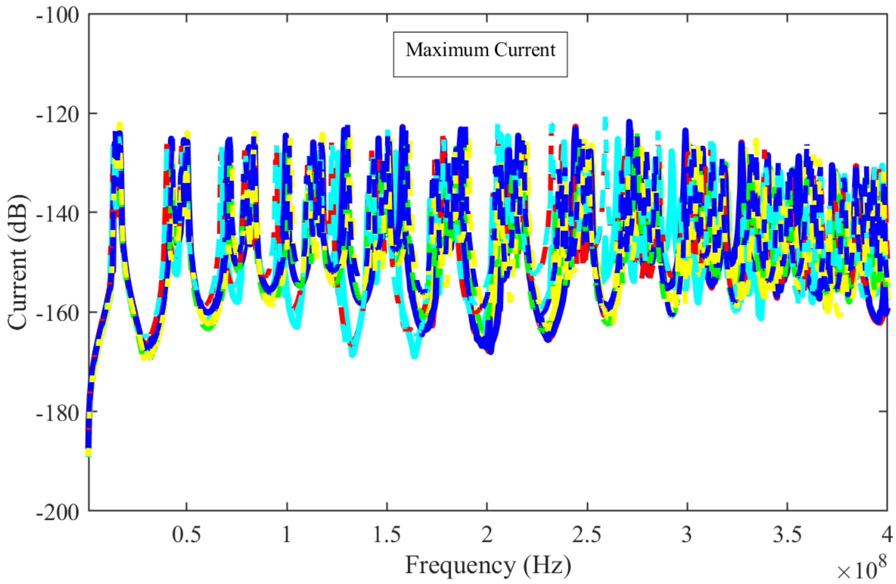

Figure 6.46 | Maximum currents in ten cores wire bundles for 10 sets of configurations

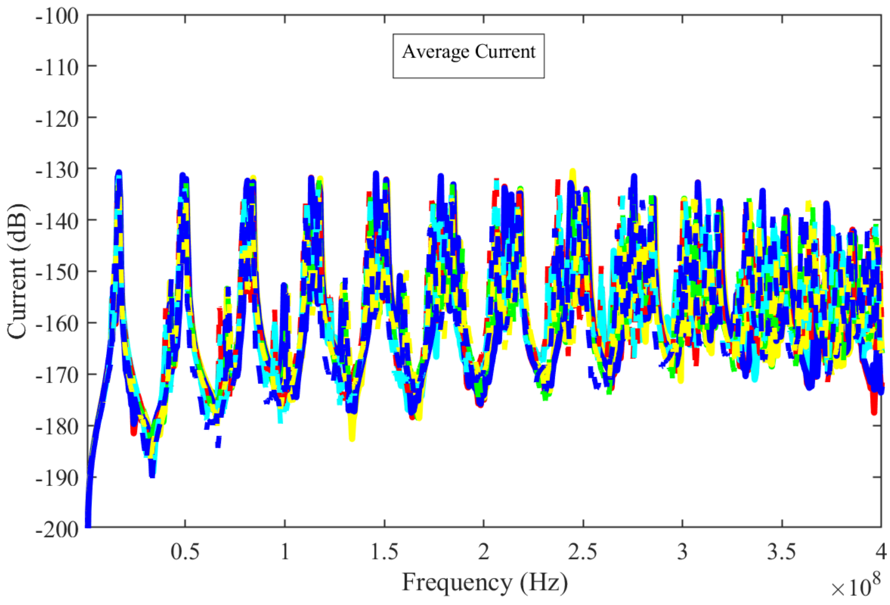

Figure 6.47 | Average currents in ten cores wire bundles for 10 sets of configurations

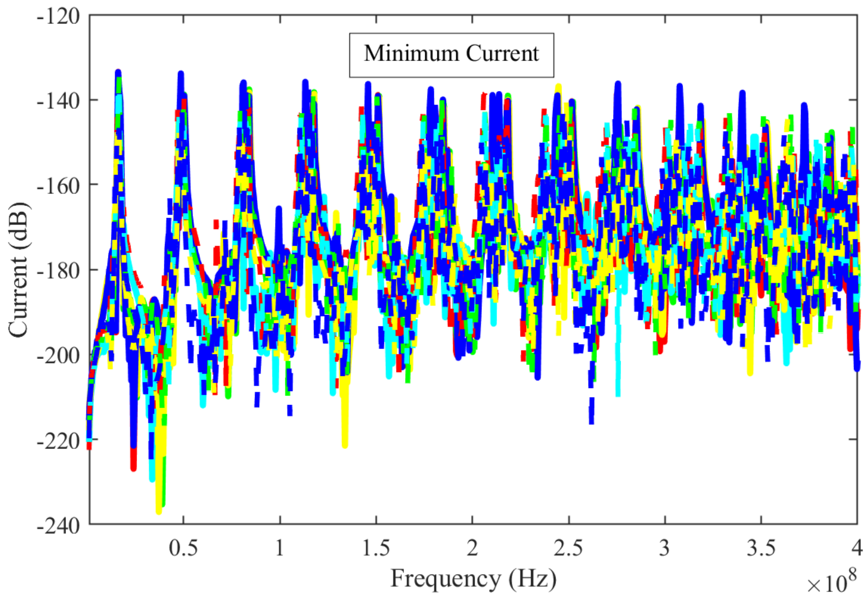

Figure 6.48 | Minimum currents in ten cores wire bundles for 10 sets of configurations

6.12 Conclusion

This chapter has presented simulations of wire bundles with different configurations upon plane wave excitations. Sufficient simulation results were obtained using localised mesh refinement whilst remaining outer region coarsely discretised. The effect of spatial variation of a single-core cable loom has shown to be small in a homogeneous environment, but shift resonant frequencies with a wooden spacer placed above the ground plane. The current induced in a two-core wire bundle has shown increased cross coupling between cores as the spatial distance between two cores decreased. The separation of wires along the route has shown to increase the number of resonances. The effect of shielding was shown in wires within multi-core wire bundles where the outer cores prevent the field coupling into inner cores. The variation of spatial relationship of cores within a multi-core cable loom has shown to affect the resonant frequency of maximum, average and minimum induced currents in the loom, especially in the higher frequency range.

References

[6.1] S. Tkatchenko, F. Rachidi, and M. Ianoz, "Electromagnetic field coupling to a line of finite length: theory and fast iterative solutions in frequency and time domains," IEEE Transactions on Electromagnetic Compatibility **37**, 509–518 (1995).

[6.2] A. G. Coupling, O. Emi, and T. Cables, "Coupling Of EMI To Cables : Theory And Models," pp. 1–44.

[6.3] G. Andrieu, L. KonÉ, F. Bocquet, B. DÉmoulin, and J. Parmantier, "Multiconductor Reduction Technique for Modeling Common-Mode Currents on Cable Bundles at High Frequency for Automotive Applications," IEEE Transactions on Electromagnetic Compatibility **50**, 175–184 (2008).

[6.4] J. Dai, F. Dai, and X. Zhao, "Output prediction about crosstalk coupling of representative multi-cable bundle on aircraft platform based on neural network," in "2009 3rd IEEE International Symposium on Microwave, Antenna, Propagation and EMC Technologies for Wireless Communications," (2009), pp. 381–384.

[6.5] X. Meng, P. Sewell, N. H.A. Rahman, A. Vukovic, and T. Benson, *Experimental benchmarking of Unstructured Transmission Line Modelling (UTLM) method in modelling twisted wires*, vol. 1 (2016).

[6.6] X. Meng, P. Sewell, A. Vukovic, Z. Zhang, T. M. Benson, C. Jones, S. Earl, R. Walton, and G. South, "Numerical simulation of electromagnetic coupling in explicitly meshed wiring looms and bundles," IET Science, Measurement & Technology **12**, 176–181 (2018).

[6.7] L. Paletta, J. P. Parmantier, F. Issac, P. Dumas, and J. C. Alliot, "Susceptibility analysis of wiring in a complex system combining a 3-D solver and a transmission-line network simulation," IEEE Transactions on Electromagnetic Compatibility **44**, 309–317 (2002).

[6.8] C. R. Paul, *Analysis of multiconductor transmission lines* (John Wiley & Sons, 2008).

7

Log-periodic Dipole Array (LPDA) Antenna

This chapter presents the modelling of Log periodic dipole array (LPDA) antenna using UTLM. Background theory and design prodcedure of LPDA is introduced. An example from textbook is built and simulated and the resultant radiation pattern is compared to the theory.

***

7.1 Introduction

In chapter (5) and (6) the Unstructured Transmission Line (UTLM) method was applied to various wiring models to investigate the electromagnetic behaviour of them to external field coupling. These canonical and benchmark problems established the application, self-convergence and accuracy of the UTLM method. A wide frequency coverage of incident electromagnetic fields is needed in modern electromagnetic susceptibility testing and verification. This requires a broadband antenna as the source of these fields. The log-periodic dipole array (LPDA) is a common broadband antenna that is constructed by a sequence of parallel linear dipoles to cover different frequency bands. Due to its low construction cost and linear polarization, it is preferred over other broadband antennas such as the spiral antenna and the TEM horn [7.1,7.2] In this chapter the UTLM method is used to simulate LPDA antennas to further demonstrate its practical application.

This chapter is outlined as follows. First the background theory of the LPDA antenna and a theoretical design procedure is introduced. This procedure is used to specify an example design with designated requirements on directivity and bandwidth, which is then modelled using the UTLM method. A detailed description of how to build and model this structure is then given. Numerical and analytical results are compared and the capability of the UTLM to provide far field data is described.

7.2 Background theory and Design of the LPDA

7.2.1 Theories of Log-periodic dipole array (LPDA) antenna

The basic structure of a log-periodic dipole array antenna is formed by a number of parallel dipole elements with the size of each element reduced progressively from back to the front. The maximum radiation is directed from largest element toward smallest element. Fig.7.1 shows a typical structure of a LPDA whose end points at either side form a straight line and join to a virtual apex. The half apex angle α is introduced to define the angle between the end point and the centre line. The element dimension notations L_n, R_n, D_n, d_n represent the dipole length, distance to the apex, diameter of the nth element and distance between adjacent elements respectively, starting from the largest one. One key feature of these parameters is that they share same scaling constant τ for adjacent elements [7.1–7.3]:

$$\frac{L_n}{L_{n+1}} = \frac{R_n}{R_{n+1}} = \frac{d_n}{d_{n+1}} = \frac{D_n}{D_{n+1}} = \frac{S_n}{S_{n+1}} = \frac{1}{\tau} \tag{7.1}$$

Another spacing constant σ is defined to relate the element length and the spacing

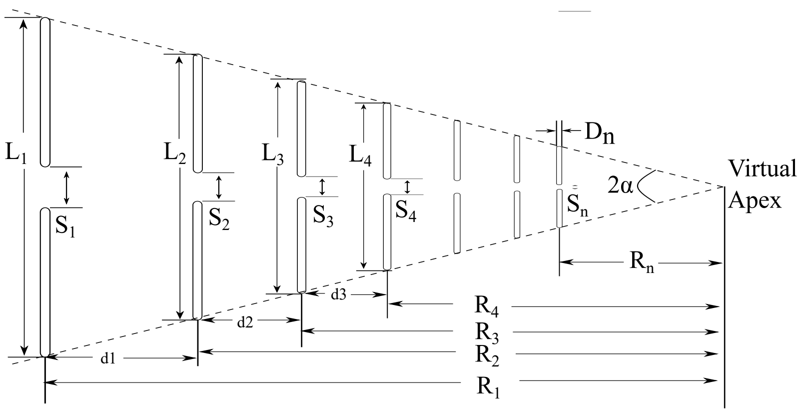

Figure 7.1 | LPDA structure and dimensions [7.1]

between adjacent elements:

$$\sigma = \frac{d_n}{2L_n} \tag{7.2}$$

Due to such structure, the LPDA is able to operate over a wide band frequency range; the lower cut-off frequency is determined by the electrical length of the longest element and the higher cut-off frequency determined by the shortest. These elements are mainly divided by three regions, which are the active region, loaded transmission line region and the reflective region respectively. For different operating frequencies, different regions along the array are activated. These regions are located at positions where element lengths are near or slightly smaller than half of the wavelength of operation. As the operation frequency increases, the active region passes from the back largest elements to the front smaller elements. In the loaded transmission line region, dipoles are shorter than a half-wave length at the operation frequency and act capacitively as directors [7.3]. The longer elements that locate behind the active region appear inductive and acts as reflectors.

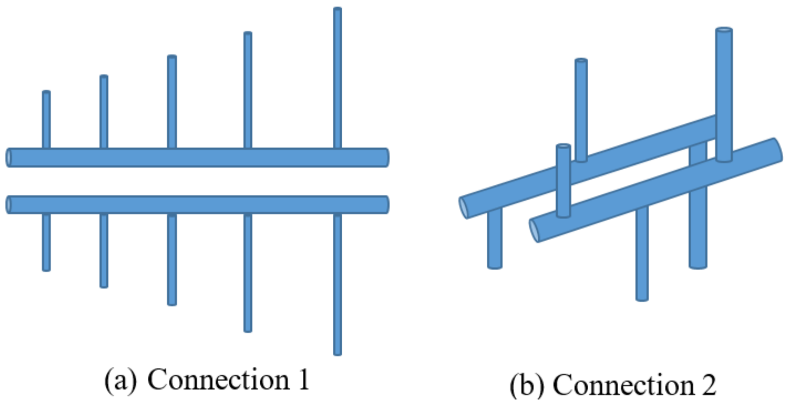

Figure 7.2 | Two dipole elements connection methods on the feeder line

All elements of an LPDA are connected and fed through the centre terminal of each element by a balanced and constant impedance feeder from the smallest dipole. An unsuccessful excitation method like would result in phase progression along the array, due to the same phase relationship between adjacent elements as shown in Fig. 7.2 (a), and unwanted beam toward the back of the array. In order to minimise this effect, it is suggested to alternately connect each element and therefore add a 180° phase to the neighbouring elements as shown in Fig. 7.2 (b).

7.2.2 LPDA design procedure

There are various methods developed to design LPDA antennas based upon certain specifications. In this chapter the method by [7.1] is adopted to calculate antenna configurations. First of all, the scaling factor τ and the relative spacing factor σ are obtained. This can be done by specifying desired directivity and finding approximated τ for optimised σ from Fig. 7.3

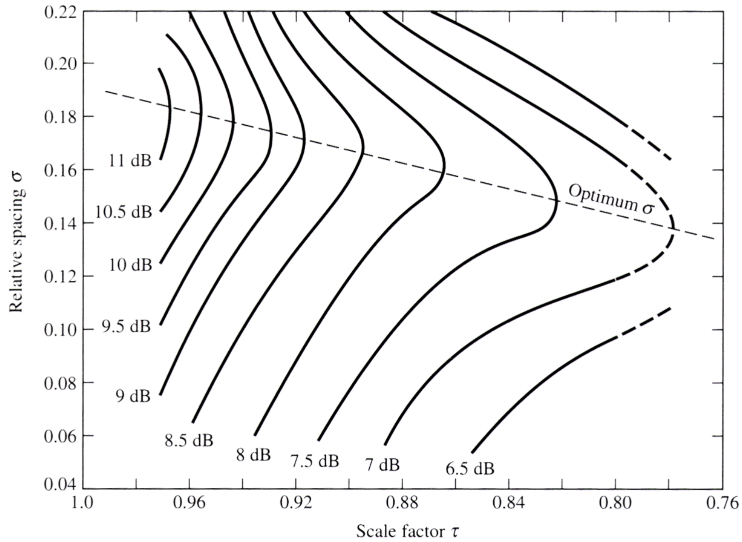

Figure 7.3 | Directivity versus scale factor τ and spacing factor σ [7.1]

The halr-apex angle α of the LPDA can then be obtained from:

$$\alpha = tan^{-1}\left[\frac{1-\tau}{4\sigma}\right] \tag{7.3}$$

The bandwidth of the active region B_{ar} is related to α and τ by

$$B_{ar} = 1.1 + 7.7(1-\tau)^2 \cot\alpha \tag{7.4}$$

This indicates a slightly larger bandwidth than the requirement in order to operate at lowest and highest desired frequencies. The distance between the longest and

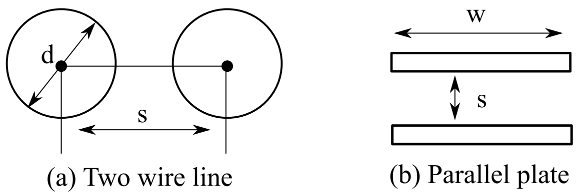

Figure 7.4 | Two types of feeder line for LPDA

shortest elements is calculated from:

$$L = \frac{\lambda_{max}}{4}(1 - \frac{1}{BB_{ar}}) \cot \alpha \tag{7.5}$$

where λ_{max} refers to the wavelength at lower cut-off frequency. Besides, the total number of elements is determined by the designed bandwidth and the scaling constant:

$$N = 1 + \frac{\ln(BB_{ar})}{\ln(1/\tau)} \tag{7.6}$$

The spacing s_n between the feeder lines is assumed constant along the array, as it shows negligible effect on results [7.1]. For a two-wire transmission line of diameter d, s refers to the centre-to-centre spacing between two lines as shown in Fig.7.4(a).

$$s = d \cosh\left(\frac{Z_0 \pi}{\eta}\right) \tag{7.7}$$

For a parallel plate line of width w, s refers to the separation distance between two plates as shown in Fig.7.4(b):

$$s = \frac{Z_0 w}{\eta} \tag{7.8}$$

In both equations Z_0 refers to the characteristic impedance of the feeder line, which is determined from the average characteristic impedance of dipole elements Z_a, the desired input impedance and a relateve mean spacing $\sigma' = \frac{\sigma}{\sqrt{\tau}}$.

7.3 Modelling example

This section models an example design of LPDA antenna presented in [7.1] in order to investigate the capability and performance of the UTLM method. The example provides sufficient design parameters and derives the detailed antenna dimensions to construct. The simulation focuses on finding far-field radiation patterns and VSWR for different frequencies.

7.3.1 Antenna design requirement

The detailed antenna design specifications are listed in table 7.1.

Higher Bandwidth Limit (MHz)	216
Lower Bandwidth Limit (MHz)	54
Directivity (dB)	8
Input Impedance (Ω)	50
Diameter of largest feeder line (cm)	1.9

Table 7.1 | LPDA Design requirements for example 11.1, Antenna theory [7.1]

Based on equations presented in section 7.2.2 and parameters provided in table 7.1, one is able to derive the spacing parameters and dimensions of the first elements. Subsequent elements are then obtained based on the scaling factor The designing and derivation steps are presented in [7.1], therefore are not detailed here. Table 7.2 lists values of design parameters and dimensions of the first element, with notations labeled in Fig. 7.1. Dimensions of subsequent elements are then obtained according to equation (7.1).

7.3.2 Geometry construction

The geometrical model is constructed as shown in Fig.7.5. The antenna is placed 6 m above the ground plane using a support post mounted at the centre of the feeder

half-apex angle (α)	12°
relative spacing factor (σ)	0.157
scaling factor (τ)	0.865
Number of elements (n)	14
$R_1 - R_n$ (m)	5.541
L_1 (m)	2.7759
D_1 (cm)	1.9
d_1 (m)	0.8786
s_1 (cm)	0.32

Table 7.2 | Geometry parameters for the LPDA

line. The feeder line is formed by a parallel-plate line of width 2cm and separation distance 0.32cm in order to provide the desired 60 Ω impedance. As stated in [7.1], the effect of separation distance between feeder lines is small on the performance of the antenna, therefore it is set to be constant in this work for the ease of model construction.

A coaxial cable that connects to the ground plane rises along the post and excites the antenna from the front end as shown in the insets of Fig.7.5 (b). The outer conductor of the coaxial cable connects to a hollow metal pad, which has a hole on the upper side, and the pad connects to the lower conductor of the feeder line while the inner goes through the hole and connects to the upper feeder line. In this way currents from the inner conductor of the coaxial cable goes to the upper feeder line and currents from the outer conductor goes to the lower feeder. The coaxial cable has an outer radius 5mm and inner radius 1mm with a relative dielectric permittivity $\varepsilon = 3.723$ in the middle in order to provide 50 Ω characteristic impedance for the coaxial cable according to equation:

$$Z_0 = (138/\sqrt{\varepsilon_r}) \times \log_{10}(R/r)$$

where R is the outer radius and r is the inner radius.

The dipole elements are connected alternately to the upper and lower feeder line to achieve 180° phase shift between adjacent elements as shown in the inset of Fig. 7.5. The dimensions of each element are obtained according to the first element and the scaling factor τ.

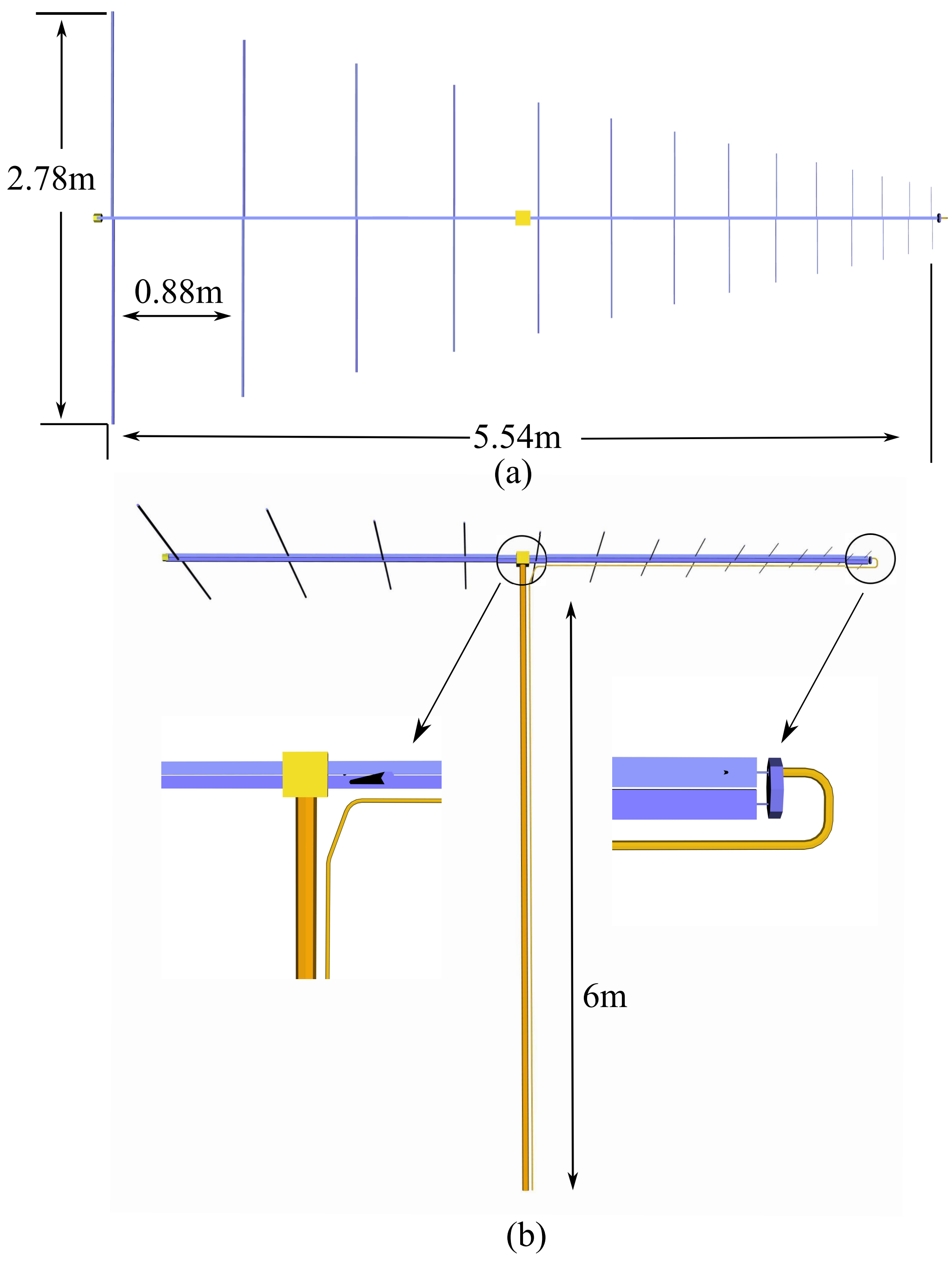

Figure 7.5 | Geometry structure and dimensions

7.3.3 Simulation

The convergence test of the constructed model with mesh size is firstly performed. The antenna is excited from the bottom side of the coaxial cable by a transverse eletromagnetic (TEM) mode wave at 60 MHz with a frequency range from 55 MHz to 65 MHz. The far field patterns are measured 1λ away from the antenna, with E-plane referring to the horizontal plane that contains dipole elements and the H-plane referring to the plane perpendicular to the E-plane.

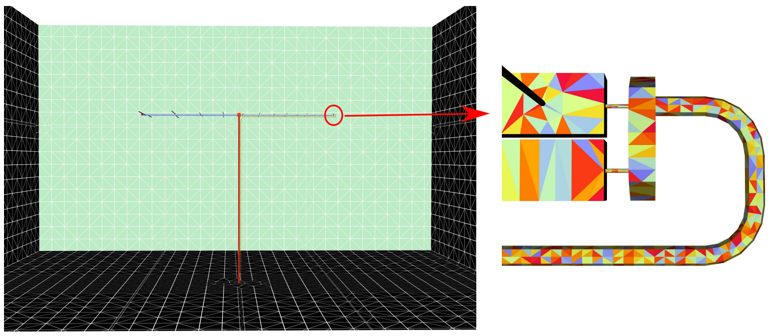

(a) (b)

Figure 7.6 | Mesh plot of the LPDA model of cell size 0.5m with a) the whole model and b) details around the front end

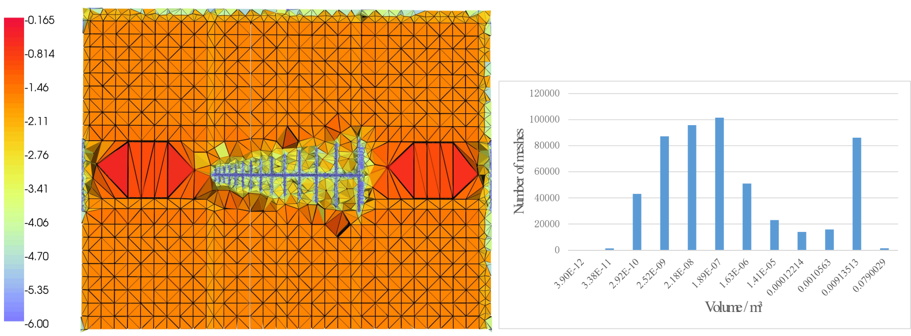

(a) (b)

Figure 7.7 | Mesh distribution of the model by mesh size $\lambda/10$ with a) cross-sectional view and b) number of meshes as a function of cell volume

The model is meshed with good quality tetrahedral cells (Q=5; y=5) of maximum cubic cell size 0.5m which corresponds to $\lambda/10$ at 60 MHz; where Q and y refer to quality factors of tetrahedral cells and triangular faces respectively. Fig.7.6 shows meshes of the whole model and around the antenna respectively. Due to the thin and circular features of antenna elements, fine sized tetrahedral elements are used around the antenna while crude meshes used in the free space region. The cross-sectional view of the meshed model in Fig.7.7 (a) and statistics chart in Fig. 7.7 (b) show clearly mesh distribution of different cell sizes. Fig. 7.7 shows that meshes of size below volume $10^{-6}m^3$ are generated around antenna elements and have larger amount than those generated in the free space.

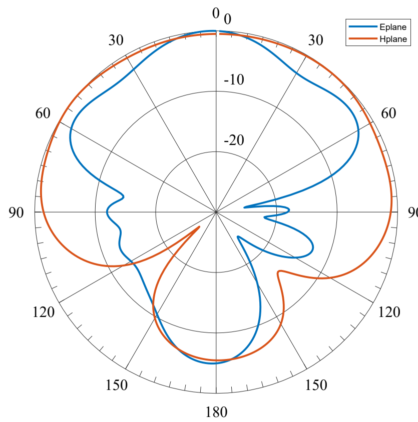

Figure 7.8 | Far fields at 60MHz for mesh size of $\lambda/10$

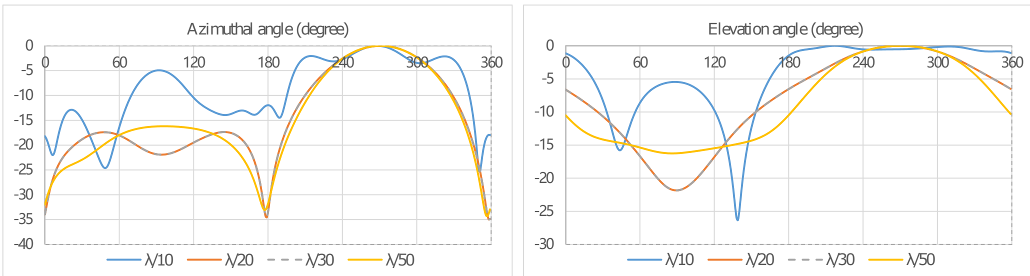

(a) E-plane

(b) H-plane

Figure 7.9 | Far field radiation for different mesh sizes

The far fields in the E-plane and H-plane for the $\lambda/10$ mesh observed one λ away from the front end are shown in Fig.7.8, It is observed that the far field radiation is not accurately resolved due to coarse sampling of the free space region. Smaller meshes are then used in the free space region and the main lobe of far fields converge for cell sizes below $\lambda/20$ as shown in Fig.7.10. $\lambda/50$ mesh shows approximately 5dB higher back lobe radiation than coarser meshes.

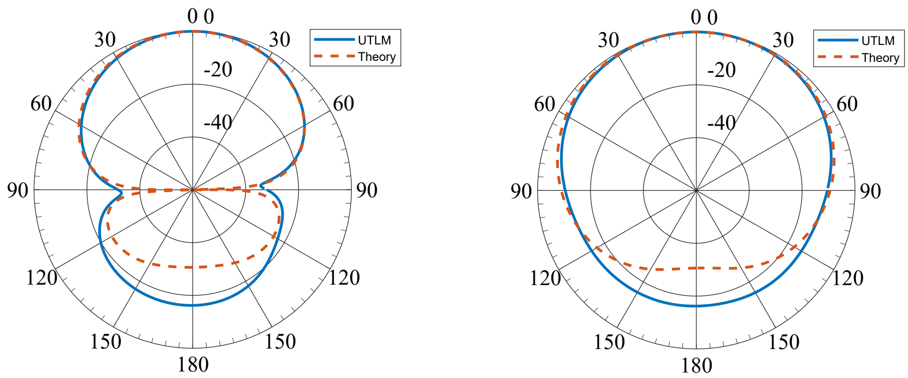

(a) E-plane 60 MHz

(b) H-plane 60 MHz

Figure 7.10 | Far field radiation pattern 60 MHz

The theoretical radiation pattern of the designed antenna based upon current distribution approximation is derived from [7.1] and compared to the results obtained from the UTLM simulation using $\lambda/50$ mesh, as shown in Fig. 7.10a. The simulated results in both E- and H-planes show good agreement with the theoretical pattern on the main radiation direction. The simulated result shows slightly higher back lobe radiation, but is in acceptable level.

The radiation pattern at different frequencies in the desired bandwidth are then simulated. In order to obtain accurate results, the model is discretised by $\lambda/30$ tetrahedral meshes with λ corresponding to the wavelength at 200 MHz. Fig. 7.11 shows observed far-field radiation patterns for frequencies 80 MHz, 120 MHz, 160 MHz and 200 MHz respectively, and compared with theoretical patterns obtained from [7.1]. For low frequencies like 60 MHz and 80 MHz, the simulated result show approximately 10 dB higher back lobe radiation levels. This is because at low frequencies, the active region is at the back of the antenna and is highly affected by the termination load. It is also found that with the operation frequency increasing, both simulation and analysis show more side lobes and back lobe levels in both E and H-plane. The UTLM simulation shows generally good agreement with benchmarking patterns at different frequencies.

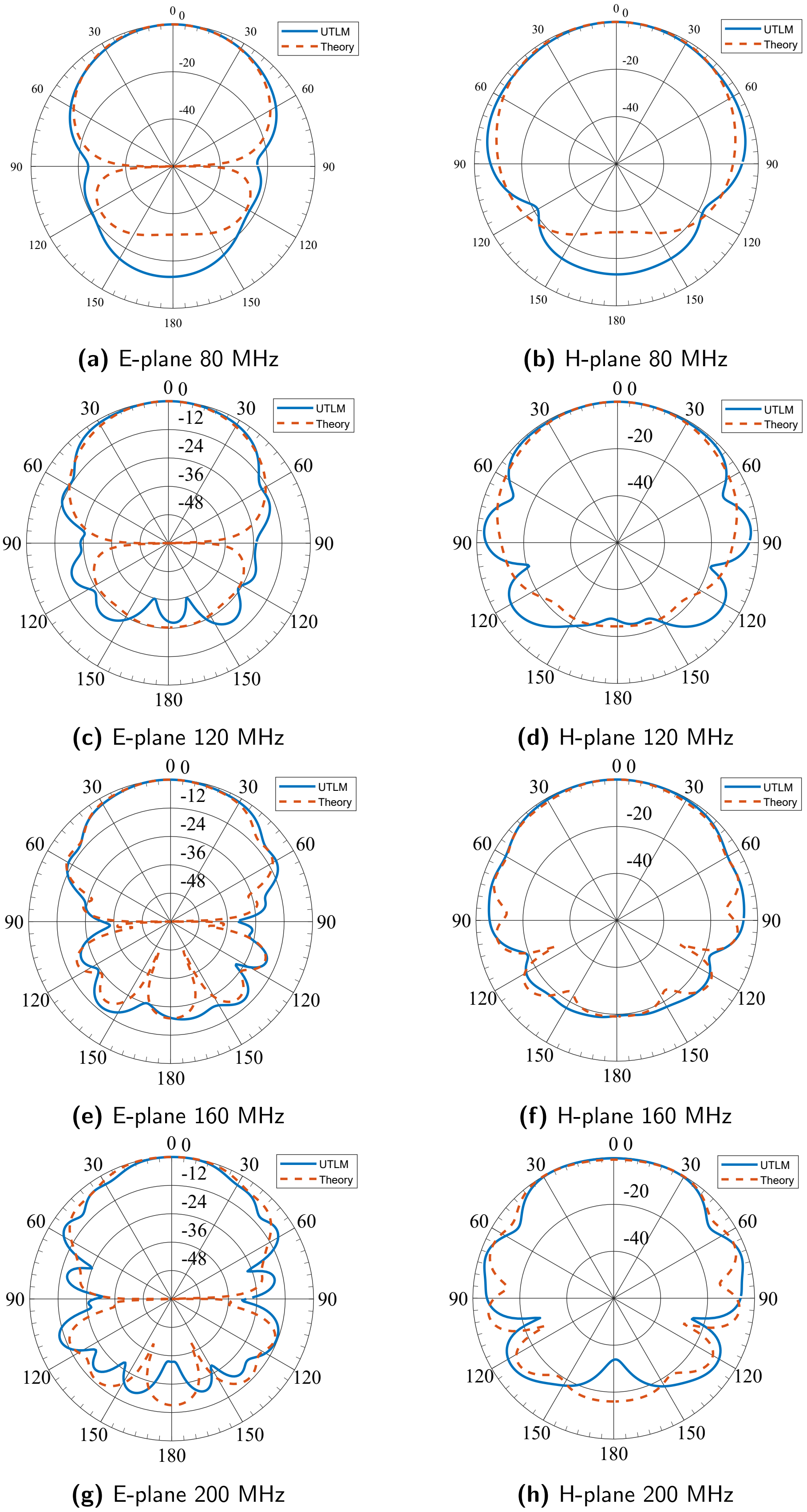

(a) E-plane 80 MHz **(b)** H-plane 80 MHz

(c) E-plane 120 MHz **(d)** H-plane 120 MHz

(e) E-plane 160 MHz **(f)** H-plane 160 MHz

(g) E-plane 200 MHz **(h)** H-plane 200 MHz

Figure 7.11 | Far field radiation pattern for different frequencies

7.4 Conclusion

In general, the capability of UTLM in modelling LPDA antenna is demonstrated in this chapter. The use of thin and long wire structures in the antenna construction and in wideband operation frequencies decide its difficulty to model using full-wave time domain electromagnetic solvers, as their particular requirement of volume mesh in the whole simulation space. Nevertheless, the UTLM method demonstrates its robustness in such background using sufficient meshing sizes and acceptable geometry constraints.

References

[7.1] C. A. Balanis, *Antenna Theory: Analysis and Design*, no. v. 1 in Antenna Theory: Analysis and Design (John Wiley & Sons, 2005).

[7.2] T. A. Milligan, *Modern Antenna Design*, Wiley - IEEE (Wiley, 2005).

[7.3] I. Poole, “Log Periodic Antenna Theory, Operation, & Formula,” (2018).

8

Conclusion

8.1 Overview of the work presented

The aim of this work was to study the Electromagnetic Compatibility (EMC) of wiring problems in modern Comupational Electromagnetic (EMC) environment and demonstrate the capability of Unstructured Transmission Line Modelling method to directly modelling wire structures using explicit unstructured tetrahedral meshing techniques.

The work has presented the UTLM method, as a novel powerful CEM method which is unconditionally stable, is capable to solve various wiring problems without decoupling into two-step process that solves the wire model and field-to-wire separately. The UTLM resolved the issue of curved boundary of circular wires using tetrahedral meshes and implicit mesh clustering method to increase time step. The local mesh refinement has been used to resolve the dispersion error due to mesh size inconsistency in the near-field area around the wire without compromising meshing sizes in the whole simulation space and achieves fast convergence of simulation results. This also provided the capability of UTLM in modelling multi-scale complex electrical systems, where free spaces can be modelled using relatively coarse meshes and fine meshes are kept near wire models.

This work has presented the study of various wire bundles of different configurations upon external field excitation. A simple straight wire model upon a plane wave excitation presented resonances according to its length. When multiple wires presented in a wire bundle with close space, more resonances were shown due to cross coupling between cores, and resonant frequencies were shown related to spatial relationship of wires within the bundle. In addition, wires in the inner region of a bundle were shown less current induced due to shielding from wires in the outer regions. However, more wires within a bundle did not show affecting the overall system performance which is decided by the maximum induced current in the bundle.

The UTLM method has also shown the capability to model an Log-periodic dipole array (LPDA) antenna which consists of 14 dipole pairs with maximum length 2.78 m and minimum diameter 1 mm. The radiation pattern at different frequency bands were shown good agreement to the theories.

Although UTLM has shown its feasibility in modelling multi-scale features, the computational expenses is still the main concern. In a simple simulation set-up of a wire bundle above a ground plane with truncated simulation space, wire structures contributed to the most number of meshes with apparent smaller size compared to the outer space. When number of wires increases or wires with curved routes, the computational cost increased accordingly. Nevertheless, the significance of the work presented in this thesis is the presence of a straightforward method without a priori simplification and approximation and the capability of extending this work to more complicated studies.

8.2 Future Work Consideration

In this contribution, various wire bundles were directly modelled and studied using the UTLM method. This work might be extended in the future for more complicated structures such as wire bundles not parallel to the structure, non-straight wire bundles and more complicated simulation environment such as the inclusion of carbon fibre reinforced plastics fuselages.

Meanwhile, embedding thin wire approximations in UTLM is still desired as it reduces more computational costs. The local field solutions for multi-wire systems presented in chapter 3 could be further developed to be embedded into unstructured tetrahedral meshes as well as mesh clusters. In addition, combining the method of moment for thin-wire approximation could be an alternative approach as it presents accurate results for wiring models.